AGH

AGH UNIVERSITY OF SCIENCE AND TECHNOLOGY

FIELD OF SCIENCE Physical Sciences

SCIENTIFIC DISCIPLINE Physics

DOCTORAL THESIS

*Establishing the origin of mechanical and biophysical
properties in pure titanium processed
by an unconventional severe plastic deformation*

Author: Daniel Wojtas

Supervisor: Prof. dr. hab. inż. Krzysztof Wierzbanowski
Co-supervisor: Prof. dr. hab. inż. Krzysztof Sztwiertnia
Auxiliary supervisor: Dr inż. Klaudia Trembecka-Wójciga

Completed in: AGH University of Science and Technology, Faculty of Physics and
Applied Computer Science

Kraków, 2022

Acknowledgements

I would like to express a sincere gratitude to my supervisor, Professor Krzysztof Wierzbanowski, for his invaluable expertise, guidance and patience throughout the PhD studies of mine. His insightful feedback brought my work to a higher level as I have been constantly looking up to him as an acclaimed researcher.

I would also like to thank my co-supervisor, Professor Krzysztof Sztwiertnia, for introducing me into the world of fascinating severe plastic deformation processes, and an assistant supervisor, Dr. Klaudia Trembecka-Wójciga, whose knowledge and support were priceless in formulating the research questions and methodology.

I would like to acknowledge my colleagues and coworkers from The Institute of Metallurgy and Materials Science, Polish Academy of Science for their wonderful collaboration. I would particularly like to single out Dr. Anna Jarzębska and Dr. Łukasz Maj as they have always believed in me and taught me how to be a good scientist. In addition, I would like to thank Professor Robert Chulist, Professor Magdalena Bieda-Niemiec and Dr. Jakub Kawałko (the latter from the Academic Centre for Materials and Nanotechnology AGH) for their generous help in microstructural examinations.

Finally, I would like to kindly thank Dr. Aldona Mzyk, who has been a true inspiration of mine, and Professor Romana Schirhagl (of The University Medical Center Groningen) for making it possible to perform biological investigations described within the present study.

List of acronyms

AFM – Atomic Force Microscopy

ARB – Accumulative Roll-Bonding

BF – Bright Field

CDRX – Continuous Dynamic Recrystallization

CEC – Cyclic Extrusion Compression

EBSD – Electron Backscatter Diffraction

ECAP – Equal Channel Angular Pressing

ECM – Extracellular Matrix

ED – Extrusion Direction

ELI – Extra Low Interstitial

FG – Fine-Grained

GAM – Grain Average Misorientation

GOS – Grain Orientation Spread

HAGB – High-Angle Grain Boundary

HCP – Hexagonal Close-Packed

HE – Hydrostatic Extrusion

HPT – High-Pressure Torsion

HUVEC - Human Umbilical Vein Endothelial Cell

IPF – Inverse Pole Figure

KAM – Kernel Average Misorientation

LAGB – Low-Angle Grain Boundary

LCS – Longitudinal Cross-Section

MDF – Multi-Directional Forging

NC – Nanocrystalline

OIM – Orientation Imaging Microscopy

PF – Pole Figure

RS – Rotary Swaging

SAED – Selected Area Electron Diffraction

SEM – Scanning Electron Microscopy

SFE – Surface Free Energy

SPD – Severe Plastic Deformation

TCS – Transverse Cross-Section

TEM – Transmission Electron Microscopy

TMC – Titanium Matrix Composite

UFG – Ultrafine-Grained

UTS – Ultimate Tensile Strength

XPS – X-ray Photoelectron Spectroscopy

YS – Yield Strengths

Table of contents

1. Introduction

1.1. Titanium

The existence of titanium was recognized in 1791 by William McGregor, a clergyman and an amateur-mineralogist of British descent. However, it was until 1795 that the element acquired a name, thanks to a German chemist, Martin Klaproth, who had been amazed by the strength of a material and adopted Greek mythology as an inspiration [1], [2]. Titanium is the ninth most abundant element found in the Earth's crust, but whilst narrowing the list to the structural metals, i.e., the ones used in industry for fabrication of metal structures/components, it becomes the fourth, after aluminum, iron and magnesium. Several titanium-containing ores, including ilmenite ($FeO \cdot TiO_3$), titanite ($CaO \cdot TiO_2 \cdot SiO_2$) or rutile ($TiO_2$) are treated in the well-standardized Kroll process so as to obtain a metallic titanium [3]. In a nutshell, the technique, that has been employed on a broad scale for a couple of decades, assumes that a given mineral is carbo-chlorinated to remove the accommodated impurities e.g., oxygen, iron or silicon. As a result, titanium tetrachloride ($TiCl_4$) vapor is given out and gets promptly reduced to titanium in its pure form by using molten magnesium. Afterwards, acid leaching or vacuum distillation is undertaken in order to clear away the Mg-based by-products of the reaction. At this step of the process, a purified titanium sponge is produced, although it needs to be refined and compacted, therefore melting processes are carried out [1], [2].

Titanium shares some characteristics typical of transition metals it belongs to. High melting point (1670°C), satisfying hardness and toughness as well as the ability to form compounds, exhibiting profound catalytic activity (anatase, brookite) are undeniable. Contrarily, both density and electrical conductivity of titanium stand out because of being markedly lower in comparison to the metals of the d-block [2], [3]. Automotive and aerospace industries as well as medicine, sports, chemistry and petroleum sectors greatly benefit from the use of Ti-based materials. Were it not for the laborious, capital-intensive manufacturing, poor wear resistance and machinability of titanium and its alloys, that the worldwide usage of steel as well as aluminum in different branches of economy would be seriously endangered [4].

At low temperatures, pure titanium crystallizes in the hexagonal close-packed (hcp) structure (illustrated in Fig. 1.1), known as the α phase, yet it undergoes allotropic transformation at 882 ± 2°C and the resultant body-centered cubic structure, or simply the β phase, remains stable up to the melting point [1]. Based on these two crystallographic forms, the generally accepted classification of titanium alloys into α, α+β, and β, was framed. A further subdivision between

near-α as well as metastable β alloys was also made [3]. The main alloying elements having a tendency to stabilize the α phase include aluminum, gallium, tin and oxygen. On the other hand, noble metals e.g., gold, palladium or platinum, as well as the transition metals, such as chromium, iron, manganese, molybdenum, niobium or vanadium encompass the β-stabilizing elements. To group titanium alloys by their constitution is convenient, although misleading as all of the known α alloys and even commercially pure titanium always contain a small amount of an element stabilizing the high-temperature phase, primarily iron. An excelled criterion would be to have in mind the lack of heat treatment response for the α alloys [1], [3], [5].
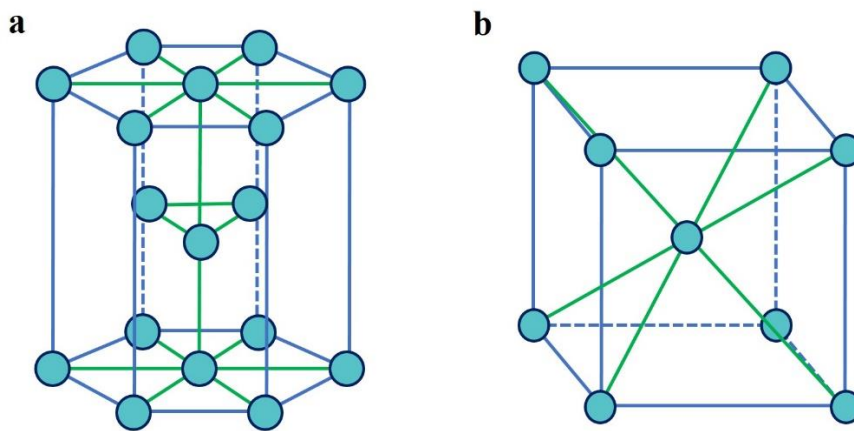
Figure 1.1. a) hexagonal close-packed structure, b) body-centered cubic structure.

Four unalloyed titanium grades differ from each other with respect to the iron (0.2-0.5 wt%) and oxygen (0.18-0.4 wt%) total. Obviously, the higher the level of an impurity contained, the stronger the particular titanium grade becomes, as may be seen in Table 1 [2], [6]. Ti-5Al-2.5Sn and Ti-3Al-2.5Sn, showing good weldability and high creep strength, are the most popular α alloys available, yet their industrial use was overshadowed with the advent of the Ti-6Al-4V alloy, offering competitive properties [3]. Overall, the alloying elements defined as α-stabilizing cause the allotropic transformation temperature to raise. The α+β alloys, whose Ti-6Al-4V is a prominent example, possess about 5-30 vol.% of the β phase, whereas for the α and near-α alloys the amount of the high-temperature titanium phase does not exceed 5 vol.% [7]. The α+β alloys combine exceptional plasticity, fatigue strength as well as fracture toughness. They are heat treatable and can be utilized safely, should the service temperature persist below 300°C. Interestingly, ductility and mechanical properties of Ti-6Al-4V could be further enhanced by decreasing the interstitial impurities content i.e., carbon, hydrogen,

nitrogen and oxygen, yielding the Ti-6Al-4V ELI (extra-low interstitial) alloy, employed on a daily basis in orthopedics and dentistry [2], [3], [7].

Alloying titanium with the addition of β-stabilizing elements provokes a decrease in the transus temperature. An apparent difference between the β and α+β alloys is that the former contains a higher fraction of β-stabilizers and, at the same time, lower amounts of α-stabilizing elements, without intermetallic phases formation [3]. β-type alloys can be hardened easily by using thermomechanical processing or heat treatment procedures. In particular, they may be heated at solution-treated condition followed by ageing. Such a unique phenomenon is related to the partial transformation of the β phase to the α phase and subsequent dispersion strengthening. In fact, properties such as plasticity, toughness, age hardenability and heat treatment capability might be significantly improved if a portion of the β phase is increased. As a consequence, elastic moduli of the β-type alloys get drastically minimized. It is of critical importance for advanced medical applications and explains the hunt for an ideal biomedical β alloy [3], [8]. Nonetheless, some of the β alloys tend to be brittle and, generally, are not meant to be applied at elevated temperatures due to low creep resistance they display. In contrast, such alloys manifest improved fabricability and biological response with comparison to the α+β group [8].

Except for titanium alloys, intermetallics comprised of titanium and aluminum as well as titanium matrix composites (TMCs) are notable Ti-based materials [1], [2]. Titanium aluminides (TiAls) are a part of intermetallic compounds, characterized by long-range ordering, thereby enhanced high-temperature strength. TiAls have been perceived as front-runners in replacing Ni-based superalloys utilized in different areas of industry, especially in the production of turbine and jet engines, exhaust valves or turbocharger wheels. Sadly, they suffer from reduced fracture toughness and low room temperature ductility. For years, it had been claimed that the existing shortcomings outweigh the strength-related profits. However, recent advances in micro-alloying and manufacturing technologies offer a glimpse of hope for Ti-based intermetallics to blossom [9].

Table 1. Mechanical properties of selected Ti-based materials [2], [6].

Material	$\sigma_{0.2}$ (MPa)	σ_{UTS} (MPa)	E (GPa)	ε_{max} (%)
α-type				
99.98 Ti (high-purity Ti)	140	235	100-145	50
CP-Ti Grade 1	170	240	103	24
CP-Ti Grade 2	275	345	103	20
CP-Ti Grade 3	380	450	103	18
CP-Ti Grade 4	485	550	104	15
Ti-5Al-2.5Sn	827	861	109	15
α+β-type				
Ti-6Al-6V-2Sn	950-1050	1000-1100	110-117	10-19
Ti-6Al-4V	825-869	895-930	110-114	6-10
Ti-6Al-4V ELI	795-875	860-965	101-110	15-10
Ti-6Al-7Nb	880-950	900-1050	114	8-15
Ti-6Al-2Sn-4Zr-6Mo	1000-1100	1100-1200	114	13-16
Ti-5Al-2.5Fe	895	1020	112	15
Ti-3Al-2.5V	585	690	100	15
Ti-5Al-2Sn-2Zr-4Mo-4Cr (Ti17)	1050	1100-1250	112	8-15
β-type				
Ti-9Mn	1023	1048	94	19
Ti-6Mn-4Mo	1090	1105	89	15
Ti-15Mo	544	874	78	21
Ti-15Mo-5Zr-3Al	838-1060	852-1100	80	18-25
Ti-15Mo-2.8Nb-0.2Si	945-987	979-999	83	16-18
Ti-12Mo-6Zr-2Fe	1000-1060	1060-1100	74-85	18-22
Ti-36Nb-2Ta-3Zr-0.3O	670-1150	835-1180	32	6.5-12.9
Ti-35.5Nb-7.3Zr-5.7Ta	793	827	55-66	20
Ti-24Nb-0.5N	665	665	43	13
Ti-24Nb-0.5O	665	810	54	22
Ti-24Nb-4Zr-8Sn	570-700	755-830	46-55	13-15
Ti-23Nb-0.7Ta-2Zr	280	400	55	33
Ti-23Nb-0.7Ta-2Zr-1.2O	830	880	60	14
Ti-13Nb-13Zr	836-908	973-1037	79-84	42-44

TMCs material systems have been designed and investigated with a similar purpose as titanium aluminides. Due to the remarkably high ultimate tensile strength and elastic moduli, TMCs could be subsumed into the most structurally efficient materials developed [10]. So far, their introduction into high-performance applications has been suppressed due to the fabrication complexities, variability of properties and implementation costs. Following a classical path of obtaining a composite material, TMCs are built of titanium matrix and reinforcement, either continuous (mainly SiC and Al_2O_3), or discontinuous (such as carbon-containing two-dimensional structures, titanium borides, carbides or nitrides). Naturally, a great deal of fibers, particulates or whiskers have proven to show reinforcing ability, although the produced TMCs systems often remain unstable [2], [10]. As a matter of fact, clustering of reinforcement has been the major challenge associated with Ti-based composites since it aggravates the mechanical characteristics of a material. In contrast, an impressive progress in the manufacturing techniques of composites should be praised. Induction plasma deposition, physical vapor deposition, tape casting or lay-up approaches, including hot isostatic pressing and vacuum hot pressing, are typically practiced for the fabrication of continuously-reinforced TMCs. On the other side, discontinuously-reinforced TMCs are produced by using powder metallurgy processes or rapid solidification technologies [10], [11].

1.1.1. Titanium in medicine

Titanium and its alloys are known as the best-in-class materials designed for orthopedic applications due to its non-magnetic properties, exceptional biocompatibility bound with corrosion resistance and relatively good formability. Artificial joints, prostheses and fixation tools made of titanium have received worldwide popularity as they are superior to customarily-used stainless steel-based elements in terms of biophysical and mechanical characteristics [6]. In medicine, Ti-based materials are also devoted to surgical instrumentation as well as components of hearing aids, artificial cornea, mechanical heart valves and pacemakers. Furthermore, a tremendous share of Ti and its alloys is dedicated to the manufacture of dental implants, bridges and orthodontic appliances [12].

Currently, it is Ti-6Al-4V and Ti-6Al-7Nb alloys that constitute a group of the most commonly applied materials in the production of implants. They are characterized by excellent mechanical properties, adequate for complex load-bearing applications, as well as low susceptibility to corrosion in various biological media i.e., body fluids and tissues. However, due to their high elastic moduli, the so-called stress shielding phenomenon is often observed [7], [13]. It leads to the formation of fibrous tissue at the bone-implant interface and, as a consequence, an uneven

distribution of mechanical loads in the peri-implant structures, micro-motions of an embedded material as well as loosening of the implant fixation. Large-scale research on β-type alloys resulted in distinguishing a group of biocompatible non-vanadium alloys, gum metals and developing materials with stiffness close to that of cortical bone, hence the stress-associated shortcomings no longer pose an obstacle [5], [8]. Nevertheless, the biomedical β alloys demonstrate unsatisfactory, high density and contain rare elements, making the final material expensive. In addition, their costly processing, due to the extremely high melting points of some elements (e.g., Ta, Mo, Nb) and resulting segregation, should also be mentioned. Recently, low-cost β-type titanium alloys, comprised of elements such as Fe, Sn or Mn, have been extensively studied as they hold premise in eradicating the aforementioned difficulties [14].

Based on a series of cell viability examinations, pure titanium could be regarded as nontoxic, nonirritating and nonallergenic metal [15]. Its biocompatibility is even slightly superior to some titanium alloys, specifically those with aluminum, chromium or vanadium addition. Interestingly, niobium and tantalum are the only β-stabilizing elements, whose biocompatibility is superior to that of titanium. Their use in medicine is albeit confined due to poor availability, high-priced cost of sourcing and manufacturing as well as low strength [6]. As mentioned, Ti-6Al-4V alloy is still the material of choice in clinical practice, however, the evidenced toxicity of alloying elements i.e., carcinogenic effects vanadium causes and neurodegenerative properties of aluminum, raises a major concern [3], [6]. Therefore, wealth of novel pure Ti-based materials developed and investigated over the past years have been targeted to eliminate the use of alloys, containing harmful alloying elements, in regenerative medicine. Furthermore, patient-customized techniques such as 3D-assisted bioprinting, have come to the fore in contemporary biomedical engineering because the materials produced demonstrate outstanding functional properties and may be readily modified by incorporating additional treatments e.g., surface optimization [7].

A considerable share of Ti-based materials utilized in medicine is taken by shape memory materials with the most typical representant being the near-equiatomic NiTi, despite the evident allergic reactions nickel tends to induce. The alloy, typically referred to as nitinol, displays a series of uncommon properties i.e., superelastic strain recovery, high corrosion resistance and strength as well as notably lower elastic modulus with comparison to both commercially pure titanium and α+β-type alloys [16]. Generally, all of the shape memory materials are regarded as smart ones. After having been quasi-plastically distorted at given temperature, they are able to recover their original form upon the presence of a particular stimulus e.g., heat, magnetic

field, light, humidity or pH. Such a feature is known as the shape memory effect that a host of metallic, ceramic, composite and synthetic materials can experience. Under certain conditions, pseudoelasticity effect (in alloys) as well as visco-elasticity (in polymers) are also observed. The former is defined as a reversible, elastic response to the stress that has been exerted on a material, whereas the latter refers to the time-dependent behavior of exhibiting both elastic and viscous characteristics when undergoing deformation. All the above-mentioned effects stem from the martensitic transformation, taking place while the right stimulus is applied [17]. The other, less frequently employed smart Ti-based materials include TiNiAg, TiZr and TiNbSn. In medicine, nitinol, usually coated with biodegradable ceramic or- polymer-based films, is used for the construction of stents, cervical replacements as well as filters. In addition, various coating-based technologies are implemented so the barrier for nickel diffusion is set up [7].

Both commercially pure titanium as well as Ti-6Al-4V alloy demonstrate poor resistance to wear, a hard-to-overpower hurdle [7]. In orthopedics and dentistry, the nature of an implanted biomaterial surface acts as one of the most crucial factors determining the speed and effectiveness of the healing processes [18]. Different surface modification techniques, including chemical, physical and mechanical treatments, are pursued at roughness shaping, improvement of corrosion and wear resistance or formation of bioactive layers that tend to modulate the bone rebuilding processes. Some methods could be used to improve not a single, specific property but a few, simultaneously. When it comes down to wear resistance, its enhancement counteracts the loosening of an implant. It might be accomplished by a host of physical deposition processes, such as cladding, ion implantation, physical vapor deposition or plasma-assisted techniques, and thermochemical surface treatments, including boriding, carburization, nitriding or oxygen diffusion hardening [7], [18]. Up till now, TiN films and their ramifications i.e., TiON, TiAlN, have proven to be the most promising as their biocompatibility, hardness and wear properties are impeccable. Unfortunately, deposition-produced surfaces tend to delaminate, whilst thermochemical approaches lead to a substantial twist of a substrate [19]. Ensuring that corrosion properties are delivered upgrades both the stability and longevity of an implant bonding during its service in a human body. Sol-gel technique, passivation, ion implantation, laser surface treatment, physical vapor deposition or plasma electrolytic oxidation are only a couple of methods utilized to improve corrosion resistance of Ti and its alloys [20]. Despite all the inarguably merits such processing technologies have, one ought to focus on their

cost, reproducibility, environmental unfriendliness, long-term impact or volatility of the properties earned.

A novel, recognized trend in surface engineering is to provide materials, having antibacterial properties so as to curb the biofilm accumulation. The development of strategies assuming the durability of antimicrobial surfaces and the selection of appropriate materials is decisive, since an implanted biomaterial, constantly exposed to the presence of various bacteria strains, should manifest an unchanged biocompatibility [21]. The employment of polymer coatings based on e.g., polyethylene glycol or hydrophilic poly(methyl methacrylate) hinders the bacteria multiplication, yet their premature degradation and strong anti-adhesive properties require careful working out [22]. On the other hand, innovative two-dimensional materials, such as nanotubes, graphene or molybdenum disulfide, although very promising in terms of electrical, optical and antibacterial properties, are additionally characterized by cytotoxicity and extremely high cost of fabrication [23]. Enriching the surface of materials with fluorine-, silver-, zinc- or copper-containing compounds should be acknowledged because such elements are known to prevent the long-term bacteria adherence to a biomaterial, thus reducing the risk of biofilm formation as well as the probability of infections and inflammation states occurrence [21].

While improving the strength of pure titanium intended for advanced, medical purposes, fine-scaled volumetric features are desired since it has been found out that surface-based modifications may not be sufficient [24]. Obviously, it seems reasonable to manipulate surface properties of a biomaterial in order for a stable and long-term implant integration to be assured. However, bulk properties are of vast importance as surface itself makes up only for a microenvironment recognizable by different biomolecules and cells [25]. The effectiveness of any procedure conducted within the field of implantology depends, to a large extent, on the characteristics of a material, mainly its fatigue and tensile strength, elastic modulus as well as ductility.

1.2. Severe plastic deformation techniques

Over the past three decades, a great deal of interest has been centered around the severe plastic deformation (SPD) techniques, exploited so the strength of various metals gets reinforced. These methods encompass a great deal of metal forming processes that operate by imposing high strains on fully-dense bulk specimens under an extensive hydrostatic pressure [26], [27]. Such extraordinary procedures lead to intense grain refinement, the phenomenon controlled by

the gradual transformation of low-angle grain boundaries (LAGBs), having high-energy configurations, into well-developed high-angle grain boundaries (HAGBs). In fact, it is believed that the prevalence of HABGs serves as the distinguishing mark of the SPD-manufactured samples [27], [28]. Grain refinement as a method of materials strengthening, realized in different ways, has been handled for years, yet it is still alloying that has gathered considerably more attention owing to its conversance and practicability [27].

The SPD processes represent a "top-down" nanocrystallization approach, enabling the formation of fine-grained (FG), ultrafine-grained (UFG) and nanocrystalline (NC) microstructures. Materials obtained by using the SPD methods manifest a set of outstanding mechanical properties, relatively homogeneous microstructure in the volume of a material as well as crystallographic texture. An important advantage of the UFG or NC metals and alloys is being contamination- and porosity-free [27]. In addition, they display surface properties to be diversified from those of their untreated, coarse-grained counterparts [29]. In stark contrast, small-scaled size and high-temperature instability are among the greatest drawbacks the materials produced by the SPD techniques have. As a matter of fact, only a few actually hit the market since potential applications the UFG and NC materials might find are scarce [27], [30]. However, the attempts for customizing the SPD methods, so they become more industrial-oriented, have never been ceased. The ongoing search for the novel SPD routes and the modification of those already existing have been dictated by the promising outcomes achieved and the need of developing innovative, low-priced materials, aiming to be employed in e.g., medicine, aviation and space industry or electronics.

By using the SPD techniques, it is possible to treat a whole spectrum of materials, including metals and alloys, intermetallics, polymers or various composites. A true milestone in the optimization of the SPD methods was the design of pioneering functional materials, such as nanostructured thermoelectrics and superconductors, irradiation-resistant metals or hydrogen-storing nanomaterials, proving that the SPD techniques are not exclusively assigned to grain refinement [31]. UFG and NC biomaterials e.g., biodegradable metals and alloys as well as pure titanium exhibiting superior biocompatibility to its coarse-grained form, seem to be of equal interest [32], [33].

A distinctive feature of the conventional SPD approaches is that the change in the transverse dimension of a workpiece does not occur. It is achieved by using complex machinery, facilities and tools, durable enough to withstand extremely heavy loads present while the material is formed. Normally, an initial billet is processed through a series of plastic deformations, not

by a single one. The core of the SPD techniques is the presence of hydrostatic pressure and, in the majority, shear deformation [26], [27]. Grain refinement during the SPD processing is governed by the two major factors: process parameters, such as temperature, strain, strain rate, deformation path, friction forces and the presence of lubricants, as well as material parameters, including stacking fault energy, melting point, initial grain size and the presence of second-phase particles [28].

A host of the experimental SPD procedures has been introduced and improved for decades, yet it is equal channel angular pressing (ECAP), high-pressure torsion (HPT), accumulative roll-bonding (ARB) as well as multi-directional forging (MDF) that have drawn the greatest attention. As the name suggests, ECAP is performed by inserting a squared or a round sample into a die, having two intersecting channels of equal cross-section. The specimen is pushed with the use of a plunger and experiences massive shear straining, directly at the place where both channels connect. Typically, four, eight or twelve passes of ECAP are realized in order for the material to be refined into the submicrocrystalline level. A plenty of variants, involving rotations of the workpiece about the operating axis are possible, hence different microstructures and textures are obtained. B_C route, assuming the rotations by 90° in the same direction every time the billet is re-deformed, has become the most frequently applied version. Generally, the low productivity of the ECAP technique is what poses a challenge. Therefore, alternative modifications of the method such as ECAP-Conform, rotary-die ECAP or incremental ECAP have been proposed to address this issue [27], [28].

Despite the fact that ECAP is by far the most developed and analyzed SPD technique, it is HPT that enables the nanostructures to be formed readily. Nowadays, the process is employed mostly for research purposes, however it remains the only one SPD method, allowing grain size to be reduced to over a dozen of nanometers without any additional working processes [27]. While executing HPT, a coin-shaped sample, placed between the two anvils, gets thinned by simultaneous torsional straining and applying high pressures, exceeding the range of a few gigapascals. A particular number of rotations strongly influences the microstructure produced, thereby mechanical properties of a deformed sample. Rather surprisingly, not only a variety of metals, but also amorphous glasses and crystalline ceramics may be easily subjected to the HPT approach. The technique is also used for powder consolidation. Nevertheless, microstructure inhomogeneity as well as the dimensions of manufactured specimens makes the HPT method unable for large-scale commercialization. Only a couple of potential applications, such as

nanomagnets showing enhanced magnetic properties or small-sized components of microelectromechanical systems might be considered [27], [34].

The ARB technique was suggested to overcome the constraints of the ECAP and HPT processes. Although the method quickly turned into a very promising SPD route, its expensiveness, stemming from meticulous material preparation and energy consumption, cannot be disregarded. One of the greatest benefits of ARB is making use of a conventional rolling facility, thus eliminating the necessity of constructing specialized, powerful setups [27], [31]. The technique works by repeated stacking of the material followed by rolling. Every time the sheet is piled up for a consecutive deformation, it is cut in half, then its surface gets degreased and wire-brushed in order for the cut samples to bond tightly. Usually, the processing is performed at elevated temperatures. ARB may be suitable for the fabrication of metal-matrix composite materials by sheathing mixed powders [27].

MDF has been, so far, the only SPD approach that was successfully optimized, upscaled and, as a result, it facilitates the formation of UFG materials having sizable dimensions. The method assumes that numerous free-forging operations, involving setting and pulling in three orthogonal directions, are realized. Owing to the fact that the MDF processing begins at warm conditions and the applied loads are relatively low, brittle materials may be efficiently refined to the nanometer range [27], [35].

In addition to the abovementioned SPD technologies, the methods such as twist extrusion (TE), asymmetric rolling (ASR), repetitive corrugation and straightening (RCS), friction stir processing (FSP) and cyclic extrusion-compression (CEC), deserve mentioning [27]. There is also a wealth of the so-called SPD-derivative processes as well as combined or hybrid SPD techniques that have produced highly promising outcomes and their usefulness is yet to see the light of day [28]. Hydrostatic extrusion (HE) along with the KoBo technique are two representatives of the unconventional SPD approaches [12], [36]. The most recent breakthrough in modern materials science pertains to the surface severe plastic deformation (SSDP) methods, profiting from the principles of the classical SPD techniques. Surface mechanical attrition treatment (SMAT), severe shot peening (SSP) and repeening (RP) enable nanostructures to be formed on the metallic surface without affecting the bulk of a material [27].

1.2.1. Hydrostatic extrusion

HE, a direct extrusion method patented in the late 1880s, belongs to the class of the unconventional SPD approaches, mostly due to the reduction in diameter

of a processed billet [37]. In contrast to the conventional extrusion, HE functions with the use of a pressurized liquid medium, enclosing the material to be deformed. Therefore, the process is also referred to as hydraulic direct extrusion or simply hydroextrusion [12], [38]. Over the decadesm the HE treatment had been employed mainly for shaping of metal objects, but with nanotechnology rapidly growing into a preeminent field of research, it was rediscovered at the beginning of the XXI century [39].

The effectiveness of HE in the fabrication of UFG or NC materials has received universal acclaim as recently the technique has been perfected to such a degree that it could go up against the conventional SPD methods with regard to the strength of processed specimens [40], [41]. Originally, HE was aimed to improve the mechanical characteristics of different polycrystalline materials, yet it turned out that electrical conductivity, magnetic properties or corrosion resistance could also be enhanced [42]–[44]. The process may be applied for plastic deformation of structural materials (steel, Al, Cu), refractory metals (Nb, W), functional materials (Dy, Ni, FeGa), biomaterials (Mg, Ti, Zn, Zr) as well as various intermetallics and composites [45]–[49]. By means of the multistage HE, long-length rods, wires or tubes, exhibiting fiber texture and mixed microstructures, are manufactured [12]. Furthermore, hybrid processing by combining HE with the other SPD methods e.g., HPT or ECAP, have also proven to be advantageous in the production of high-strength polycrystalline materials [50], [51].

A typical HE device, as seen in Fig. 1.2, is constructed of an operational chamber, guaranteeing the safety and finalization of the process, a set of dies, sealing the system, and a nonstationary piston, starting the extrusion operation. A given workpiece, positioned inside the chamber and surrounded by a liquid medium, such as castor oil, gets deformed as the piston is moved. At that point, the medium is compressed, resulting in a steady increase of hydrostatic pressure in the chamber. Overall, the entire process of extrusion begins as soon as the value of material's yield point is exceeded and the frictional resistance is conquered. In the end, a rod exits the chamber by a die hole, usually of conical geometry. Then, water-quenching may be handled in order to minimize the adiabatic heating effects and the whole deformation procedure might be redone [12], [38].
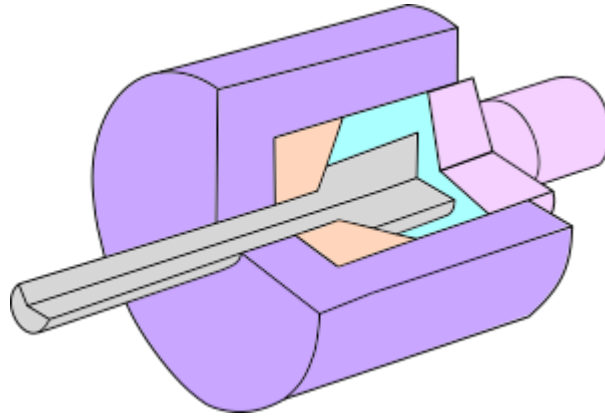
Figure 1.2. HE device scheme.

In HE, the presence of pressurized medium plays an important role, thus it is imperative to emphasize the consequences its use leads to. First and foremost, there is no contact of a billet with the piston and the chamber walls, therefore any arising friction forces are maximally diminished. They are, however, present at the die-billet interface, influencing the surface quality of the final product [12], [41]. In comparison to conventional extrusion, the operating pressure, being the active force during the HE process, is markedly reduced. As a result, lower-temperature treatment is attainable and, additionally, it may be executed with a higher reduction ratio of a billet's cross-section [52].

The main deformation mode in the classical SPD techniques, such as ECAP or HPT, is simple shear, while in the case of HE it is elongation along the direction of extrusion. Deformation taking place in this method increases the plasticity of a material as well as inhibits microcracks initiation and propagation. It is why brittle materials may be easily subjected to the HE process [38]. Such phenomena are believed to be originated from the triaxial state of compressive stresses, occurring during HE. Generally, deformation by compression is assumed to be the most beneficial for plastic working technologies. The HE method allows for unusually large plastic deformations at room temperature to be brought about, what is especially relevant to the formation of UFG and NC microstructures, since it requires low-temperature processing and high degree of deformation [38], [53].

Despite all of the assets the HE method holds, it also suffers from a few drawbacks, including inability to accumulate remarkably high values of plastic strain, reachable for the conventional SPD approaches, especially multiaxial forging (MAF), CEC and ECAP. Obviously, the reason behind such a limitation is the change in a diameter of a deformed billet. The HE process ought

to be finished in a particular number of stages, while most of the SPD technologies enable a material to be treated without any restrictions [12], [54]. Up till now, maximally 20 steps of HE, resulting in 5.47 of total strain, have been reported [55]. In addition, time-consuming liquid maneuvering, the need for a complex, sealing system, the energy loss during the process as well as surface quality of the hydrostatically extruded samples are the HE-associated disadvantages [12].

1.3.   SPD-induced microstructures

By virtue of undergoing plastic deformations, the microstructures of normally coarse-grained materials are significantly refined. The observed changes are striking, thereby ought to be discussed. Conventional techniques, such as extrusion, drawing, or cold rolling, enable for a substantial grain refinement to be accomplished, but the grain size hits the order of several micrometers, at the utmost. The microstructures obtained are typically cellular-type substructures, bordered by low angle misorientation boundaries, whilst those formed by the SPD techniques range from elongated, lamellar to fully equiaxed. The fact that the SPD methods possess the ability to scale the microstructures down to the nanometer range i.e., the level unattainable for the aforementioned metal-forming technologies, makes them a force to be reckoned with. Interestingly, distribution of the grain size in the SPD-processed materials usually follows a lognormal statistical function, though bimodal microstructures could also be acquired [26], [56].

Up till now, UFG materials, having microstructures scaled-down to the submicrometer range, have enjoyed the greatest popularity in research. It is widely known that the capability of a single-phase material to sustain large deformation is governed by its crystal structure. If the activation of considerable number of slip system is achievable, so is undergoing plastic deformation [56], [57]. Face-centered cubic (fcc) structures tend to be processed more easily, even at ambient temperatures, owing to the multiplicity of active slip systems, although the extent of plastic deformation is greatly affected by the stacking fault energy of a material. On the other hand, deformation mechanism of body-centered cubic (bcc) metals is yet to be comprehended as their drastically different plasticity hampers a uniform conclusion to be reached. Materials having hcp structure possess not only fewer independent slip systems, but also lower crystallographic symmetry, thereby they are known as hard-to-deform [28], [57]. It needs to be pointed out that irrespective of the crystal structure, melting point of a material has a profound influence on the outcomes of deformation. If the recrystallization temperature is markedly low, as in the case of Al or Mg, then, instead of dramatic grain refinement, grain

growth is bound to occur [28]. Overall, microstructures produced by plastic deformation technologies are also the resultant of the process conditions, freely to be adjusted. In general, temperature drop, pressure increase and the addition of alloying elements make the effects of grain refinement more spectacular [56].

UFG and nanostructured materials, manufactured by the SPD approaches, are filled with a variety of defects, which may be detected experimentally at the micro- and nanoscale [27]. Based on the widely recognized classification of structural defects, one may claim that point defects e.g., substitutional atoms or vacancies, as well as linear ones, such as dislocations and a host of planar defects in the form of stacking faults or grain boundaries are present in the as-processed microstructures [28]. An accumulation of defects leads to a substantial distortion of crystal lattices and qualitative change in properties of a developed material. Indeed, the SPD-fabricated metals and alloys are often named 'interface-controlled materials' since the structure and abundance of defects is an essential factor, regulating e.g., mechanical characteristics, electrical resistivity or susceptibility to corrosion [27]. Amidst the well-documented defects, grain boundaries have shown to dominate and determine the material behavior to the greatest extent. They may be categorized into LAGBs and HAGBs, taking into account a disparity in the misorientation between adjacent grains, yet the other kinds of grain boundaries such as equilibrium and non-equilibrium, as well as special and random, could be generated while exposing a sample to heavy straining. Non-equilibrium boundaries with strain-distorted structures prevail in the SPD-processed materials. They are characterized by excessive Gibbs energy, increased free volume and the existence of long-range stresses related to the high density of dislocations in the near-boundary regions [58]. Whilst deliberating about boundaries, grains should also be highlighted. SPD-fabricated microstructures are composed of a host of grains, dissimilar in size, shape, orientation, internal structure and the origin. Commonly, subgrain structure is observed in large, partially-deformed grains, whereas those of intermediate size contain a high density of lattice distortions. The most extremely refined grains, having dimensions in the nanometer regime, are mostly dislocations-free, however, some small inhomogeneities might also be noted [59].

By applying plastic deformations, it is possible to witness unusual phase transformation, including formation or dissolution of second phases, disordering and complete amorphization, providing that some structural features, such as nanotwins, precipitations (nano-sized particles), segregations or solute clusters are shaped [27], [57]. The fraction of twins i.e., defects of twin orientation, might be augmented by either low-temperature or high-strain deformation as well

as by decreasing stacking fault energy, which is typically practiced with the use of alloying. Generally, twinning is viewed to play an important role during deformation, albeit not a dominant one [28]. A substantial fraction of grains is converted into micro-twins, when the stress is applied normal to the basal plane. Reorientation of a portion of grains enables slip to occur because the favorably oriented slip systems are activated. However, twinning itself cannot accommodate the deformation needed for a considerable grain refinement since one interatomic distance is greater than the atomic displacement triggered by twinning. Overall, the process assumes fragmentation of coarse grains into lamellar structure with subsequent formation of dislocation walls inside lamellae and their further subdivision into equiaxed, nanosized blocks, exhibiting random orientation [56].

The actual mechanism responsible for downsizing coarse-grained microstructures by means of the SPD methods is still being debated, although several models have made a successful attempt in understanding the complexity of observed phenomena. It is generally acknowledged that, irrespective of the crystal structure, SPD-induced grain refinement eventuates from a non-uniform distribution of high-density dislocations, arranging themselves into low-energy configurations so that cell structures could be formed within the original grains [26], [28]. Another approach focuses on the weight of shear bands, deformation inhomogeneities of intense localized strain [60]. Owing to the small distance between the shear bands, dislocation cells, having dimensions in the submicrometer regime, are created. Their characteristic positioning and subtle differences in crystallographic orientation with respect to the adjacent regions make them subgrains, not grains, defined by a misorientation boundary of at least 15 degrees [61], [62]. In hcp metals, the process of grain refinement takes place through the nucleation of fine grains along grain boundaries or preexisting twins, forming a necklace-like arrangement. It is achieved due to stress concentrations as well as the activation of both basal and non-basal slip. The former is facilitated by external stresses, while the latter can be realized, providing those elevated temperatures or/and high stresses are maintained [27], [28].

It is widely recognized that dislocations motion and interactions they experience are at the core of all the deformation- and failure-related mechanisms in ductile, metallic-based systems. Thus, dislocation activities are believed to have an enormous impact on refining the coarse-grained microstructures by means of the SPD technologies [28], [57]. The most common dislocation classification is made upon a possible movement to immobile dislocations, known as sessile ones and mobile dislocations, glissile ones, leading to glide, which, apart from climb, is the basic dislocation movement. Glide of at least a couple of dislocations results in slip, the most

typical manifestation of plastic deformation in polycrystalline materials. There are also statistically stored dislocations, derived from random trapping processes during deformation, and geometrically necessary dislocations, arising when internal strain gradients accompany plastic deformations. Overall, dislocations possess the unique abilities to interact with all types of defects and form various structures, arrays or configurations, such as tangles, cells, loops or pile-ups, being effective barriers to further dislocation motion [27], [58].

All of the beforenamed defects are also reported in traditionally-manufactured metals and alloys, although with a considerably lower density. Therefore, a good insight into the SPD-processed specimens could be gained from an analysis of the microstructural events and features rarely, if ever, observed in bulk materials deformed by conventional methods. Grain agglomerates, originating from grain coarsening, constitute the most common exemplification of defects, exclusively seen in the microstructures formed by using the SPD technologies. If a manufactured sample is of high purity, then the chance for grain agglomerating rises notably. Generally, grain coarsening stands in stark contrast to grain refinement during the low-temperature deformation of materials and is totally undesired since a grain agglomerate as a region of high local stress and reduced strength, hinders the performance and functionality of a developed material. The other only-SPD-related microstructural defects include star twins, a group of five twins, meeting at a single junction, as well as disclinations, i.e., violations in rotation symmetry of a crystal [58].

1.4. SPD-induced biophysical properties

In literature, biocompatibility of a material is often wrongly coupled with its biological properties, whereas they characterize the nature of interactions between surfaces and biomolecules, cells or tissues, under *in vitro* or *in vivo* conditions. On the other hand, biocompatibility, an intrinsic feature of substances and materials intended for use in medical applications, could be defined as the capability to exist in complete harmony with neighboring living matter. Although the term was originally referred to the simple ability of a synthetic material to perform in the human body with a desirable, harmless recipient's response, it has evolved and been redefined throughout the years as now it also describes a great deal of biological requirements a material should meet while considering its employment in medicine and dentistry [63]. The first and foremost, a material can be viewed as biocompatible if it does not elicit any cytotoxic, carcinogenic or mutagenic effects, as well as allergic reactions and inflammatory processes [12]. The origin of conflicting nomenclature lies within the assessment of biological properties and biocompatibility, both realized by means of cell studies as well as

animal and clinical trials. In general, all the materials aimed to be utilized for medical purposes should be fully biocompatible as reflected in their microstructural, chemical and biophysical properties.

From the point of view of reactions an implanted material may trigger with the surroundings, biomaterials are classified as bioinert and bioactive. Recently, biodegradable materials, undergoing a steady breakdown in specific environments, have been developed and extensively researched as their potential applicability, especially in cardiovascular medicine and electronics, is of great significance [64]. Titanium and its alloys make up for the group of bioinert materials that do not initiate any chemical response with the remodelling tissues. Hence, surface modification techniques are implemented for Ti-based implants in order for a variety of biological and chemical processes at the biointerfaces to be encouraged [6]. Contrarily, bioactive materials are those biologically active since they tend to stimulate the formation of a direct, stable bonding between the surface of a material and adjacent tissues [21].

Ultrafine-grained and nanostructured metals represent a rather niche class of materials, mainly due to the limitations in size, anisotropy of properties as well as complicated and high-cost production, yet they tend to manifest improved biophysical properties as compared to their unprocessed, coarse-grained counterparts [65]. What needs to be emphasized is that biocompatibility of any material is a strictly surface-dependent phenomenon [66]. Each and every surface modification, performed so the material is to gain a specific property e.g., porosity, wear or corrosion resistance, might either exacerbate, increase or have no impact on biocompatibility. Processing of modern biomaterials is revolved around the techniques that result in a material exhibiting complete biocompatibility coupled with other characteristics, such as an osseointegration ability, antithrombogenic effect or increased hydrophilicity [67], [68]. Currently, antimicrobial surfaces have received a great deal of attention owing to their rapidly-lowering costs as well as an immense effectiveness in hindering the biofilm accumulation, hence declining the number of bacteria-related side effects in patients undergoing operative procedures within the field of implantology [68]. In the case of the SPD-processed titanium, it has been noted that imposing heavily strains into the volume of a material results in significant changes of surface properties, such as topography, roughness, chemical composition and wettability [69], [70].

Titanium, along with nickel, molybdenum, aluminum and chromium encompass a group of easily-passivated metals. Thus, biocompatibility of Ti-based materials is strongly related to the properties of native, well-adherent and thermodynamically stable passive oxides which are

24

spontaneously formed on titanium surface as soon as it gets exposed to different oxygen-enriched environments [15]. Such characteristics are believed to be the result of the material's low electrical conductivity. Titanium dioxide, commonly known as titania, in the form of poorly crystallized rutile and anatase, is the most frequently composed film on Ti and its alloys. Besides, some traces of titanium(II) oxide, titanium(III) oxide as well as non-stoichiometric titanium oxides could also be found. It has been shown that irrespective of experiencing a metal treatment, the thickness of titania layer is in the range from 2 to 10 nm [12]. However, the SPD techniques influence defects density, mostly oxygen vacancies as well as distribution of some functional groups and stoichiometry of an oxide layer [71]. In addition, it needs to be pointed out that the nature of titanium surface affects not only biophysical properties, but also markedly low corrosion susceptibility to various aggressive media, both acidic and alkaline. Generally, excellent corrosion resistance of Ti-based materials to biological liquids, being mostly near-to-neutral, mild solutions, is indisputable. Titanium manifests no traces of surface delamination, debris or pitting attack when exposed to simulated biological fluids, physiological saline or phosphate buffer solutions [72]. In fact, once a passive film is broken, it gets immediately rebuilt and the probable corrosion reactions are impeded. It is worth mentioning that the environments filled with halide ions (F^-, Cl^-, Br^-, I^-) are the only ones destroying the surface of Ti and its alloys locally. Interestingly, in the case of the SPD-produced titanium, a tremendous amount of high-angle grain boundaries acts as preferential sites for titania layer nucleation, even in the presence of fluoride- and chloride-containing compounds [12]. Furthermore, titanium demonstrates low susceptibility to wear-assisted kind of corrosion, namely tribocorrosion. Overall, it has been well-documented that biological compatibility of Ti-based materials is entangled with their corrosion resistance as both are originated from the extraordinary properties of the surface [6], [12], [73]. Nevertheless, a uniform conclusion on how microstructural refinement affects corrosion properties of the SPD-processed materials has not been drawn so far. More recent reports have indicated that rather than the small grain size, an enormous share of surface defects, equilibrium grain boundaries as well as crystallographic texture might be viewed as the source of change in the corrosion resistance of ultrafine- and nano-grained materials [37], [44], [73].

Nowadays, it seems obvious that by decreasing the grain size of biomaterials, having coarse-grained microstructures, down to the submicron or nanometer scale it is possible to modulate protein adsorption and cell-substrate interactions. However, the underlying mechanism controlling the observed phenomena remains poorly understood. Initially, it has been claimed

that the reduced grain size is responsible for the improved biocompatibility of ultrafine-grained and nanocrystalline materials [74], [75]. Grain refinement was somehow naturally linked to the improvement of biophysical properties in the SPD-treated materials since it was already known that the mechanism enables a material to be exceptionally strengthened. As HPT- and ECAP-processed titanium were one of the first severely deformed biomaterials obtained with the aim to rule out the use of Ti-6Al-4V alloy in medicine, they have also been the most extensively researched in terms of biophysical properties. Enhanced functionalization of a variety of cell cultures, including fibroblasts, pre-osteoblasts, osteoblasts, mesenchymal stem cells and keratinocyte cells, on the surface of ultrafine- and nano-grained titanium was widely reported [73], [76]–[81]. Cells have displayed to thrive on the SPD-processed substrates more vividly in comparison to the unprocessed samples. The vast majority of cells grown on the severely deformed surfaces tend to exhibit phenotypic morphology, including polygonal and flattened shape. A great deal of cytoplasmic extensions begins to form at the relatively early stages of incubation, indicating accelerated cells growth and proliferation [29]. Moreover, increased cell viability and alkaline phosphatase activity, the undeniable signs of superior cytocompatibility, have also been observed [82]. In addition, some studies have also highlighted the promoted absorption of proteins as well as the apatite-like crystals formation on the SPD-produced substrates soaked in various simulated body fluids, suggesting bioactivity of the inherently inert Ti-based materials [83]. As a matter of fact, direct bone apposition to the surface of ultrafine-grained titanium has been noticed under *in vivo* conditions, what implies good integration of the implanted material within a very complex, biological environment [65]. Apart from the small grain size, all of the observed changes were attributed to the presence of nanostructured surface features, in the form of nano-peaks or nano-grooves, increased hydrophilicity or nanoroughness, surface free energy (SFE) and grain boundary energy [24], [84], [85]. Recently, it has been proven that the substantial share of high-angle grain boundaries on the surface as well as crystallographic orientation of grains should also be taken into consideration while explaining the mechanism governing the improved biological response of the unconventionally manufactured materials [69], [86]. At the same time, the role of grain refinement was notably diminished. Overall, surface chemical reactivity as well as surface topography have been reported to influence cell-substrate interactions and protein adsorption the most. In fact, surface properties tend to mediate the amount, distribution and conformation of proteins adsorbed on the substrate [87], [88]. As a consequence, cells functioning, including adhesion, maturation, proliferation and differentiation, is also indirectly affected by physicochemical properties of the surface. Undoubtedly, these properties are one of the most

important factors dominating the interactions of a synthetic material with living tissues, yet, what needs to be pointed out, they may be easily adjusted, by either simple mechano-chemical preparation (subtractive manufacturing) or altering with the employment of additional surface modification technologies (additive manufacturing). However, it is worth underlining that any coating-related procedures, performed so the integration with living tissues is reached, create often unstable, artificial, chemically and physically complex interfaces. In addition, most of the applied techniques are energy- and time-consuming, thereby not environmental-friendly.

Despite a very favorable impact the severely deformed titanium exerts on biological tissues, it also displays some hard-to-overcome disadvantages, including limitations in size, nonhomogeneous microstructures and high stiffness [33]. Therefore, potential applications the ultrafine- and nano-grained Ti-based materials might find are mainly restricted to weakly-loaded implants as well as small-sized medical equipment [30].

2. Materials and experimental procedures

2.1. Material development

Commercially pure titanium (Grade 2), whose chemical composition is listed in Table 2.1, was the investigated material. It was supplied by Wolften (Poland) in the form of a rod having 50.60 mm in diameter. The choice of this particular Grade was dictated by its relatively low interstitial content, in comparison to Grade 3 and Grade 4, as well as the attractiveness for industrial and medical purposes it has displayed throughout the years. The material was subjected to the hybrid severe plastic deformation process, carried out at The Institute of High Pressure Physics (Unipress), Polish Academy of Sciences, Warszawa, Poland.

Table 2.1. Chemical composition (in wt.%) of the investigated material.

O	Fe	C	N	H	Ti
0.139	0.110	0.020	0.013	0.0007	Balance

Prior to the actual deformation, the billet in its as-received condition was extruded at ambient temperature to the rod with 26.70 mm in diameter. Subsequently, it was machined to diameter of 24.80 mm and annealed at 700°C for 2 hours so it gets homogenized and softened. Afterwards, the material was left air-cooled and then machined again in order to fit the extruder die. The whole process of HE was realized in five consecutive stages and, in addition, two steps of rotary swaging (RS), a type of net-shape forming operation, were completed so the final workpiece be clear-cut. Combining these two techniques makes the entire material development hybrid. Due to the fact that neither the extruder dies, nor the processed rods were heated during deformation, the obtained materials could be viewed as cold-worked. However, right after exiting the extruder die, the specimens were water-quenched so as to reduce the adiabatic heating effects. A part of every single hydrostatically extruded rod was sliced and stored, while the remaining piece was subjected to HE anew. It is worth mentioning that no intermediate annealing was performed, even though it used to be practiced because the process might have been finalized more smoothly. Following all the HE and RS operations, the final rod was heat treated at 200°C for 3 hours. Overall, the initial material having diameter of 24.80 mm was deformed to the final rod of 5.00 mm in diameter, what corresponds to the true strain value of 3.23, according to the equation:

$$\varepsilon = \ln\left(\frac{A_0}{A_e}\right) = lnR \quad (1)$$

where A_0 and A_e stand for the initial and the final cross-sectional area of a processed sample, while R denotes an area reduction.

Table 2.2. Diameter reductions in the applied processes and the corresponding true strain values and pressures.

Process	Reduction (mm)	ε (-)	ε_{cum} (-)	Pressure (MPa)
HE	50.60 → 26.70	1.24	-	937
Machining	26.70 → 24.80	-	-	-
	24.80 → 15.94	0.90	0.90	867
	15.94 → 11.58	0.64	1.54	1040
HE	11.58 → 9.04	0.50	2.04	672
	9.04 → 7.41	0.40	2.44	630
	7.41 → 6.14	0.38	2.82	700
RS	6.14 → 5.00	0.41	3.23	-

The change in diameters, true strain values as well as operating pressures during the whole deformation processes are summarized in Table 2.2.

2.2.   Mechanical behavior

At first, an in-depth evaluation of mechanical properties by means of static tensile and compression tests as well as fatigue test was realized. Additionally, Vickers hardness measurements over diameters of obtained rods were conducted.

Static mechanical testing was performed according to the ISO 527-2:2012 Standard. In so doing, a Zwick/Roell Z250 machine was used. Uniaxial tensile and compression tests were carried out at room temperature, employing at least three 'dog-bone shaped' and cylindrical specimens, respectively. The obtained samples were CNC-machined (CNC; Computerized numerical control) from the longitudinal cross-section of deformed rods. The overall length, width and gage length of the specimens utilized for tensile tests were 15 mm, 4 mm and 3.3 mm, respectively, while the applied strain rate was 0.008 s^{-1}. The samples used for compression testing had 7.5 mm in height, 5 mm in diameter and the applied strain was kept

at 5 MPa·s⁻¹. While executing the compression tests, the maximum capacity of the testing machine was reached, therefore it was impossible to measure the ultimate compressive strength for the analyzed materials and so only the yield strengths in compression were facilitated.

Overall, due to a vast amount of data gathered, only the most representative curves were plotted, and the results were averaged. Strains were recorded by using an automatic extensometer equipped with a Cardan shaft. Two quantities related to the strain energy i.e., modulus of resilience as well as modulus of toughness, were calculated by targeting the appropriate areas underneath the tensile stress-strain curves. Modulus of resilience is generally defined as the amount of energy a particular material may absorb without suffering any damage before it comes back to its original, undeformed shape. It could be determined using the following formula:

$$\mu = \frac{\sigma_y{}^2}{2E} \qquad (2)$$

where μ stands for the modulus of resilience, σ_y is the yield stress, while E denotes the elastic modulus of a material.

On the other hand, modulus of toughness, being a ductility-dependent property, is specified as the amount of energy required for a material to be completely fractured. It may be approximated as:

$$u_t = \left(\frac{\sigma_y + \sigma_{UTS}}{2}\right)\varepsilon - (\frac{\sigma_y + \sigma_{UTS}}{2})^2 \frac{1}{2E} \quad (3)$$

where u_t is the modulus of toughness, σ_{UTS} denotes the ultimate tensile strength and ε stands for the ultimate strain (total strain at failure). It is worth mentioning that in both cases the term *modulus* is practiced due to the operative unit i.e., $Nm \cdot m^{-3}$ or $N \cdot m^{-2}$, thus the same as in the case of stress or elastic modulus.

Samples' microhardness based on the Vickers HV0.2 method was measured by using a Zwick indenter. Only the surface parallel to the specimen's transverse cross-section was tested. The impressions were made along the diameter of a sample with a load of 200g.

Finally, rotary bending tests were realized in order to find out how the hydrostatically extruded titanium responds to alternating, high-cycle loads. Only the material deformed at the strain of 3.23 was investigated. The fatigue tests were carried out at the Institute of Advanced Manufacturing Technology, Kraków, Poland, using a fatigue testing-dedicated machine. Fluctuating loads were applied at five different strain levels until fracture was detected or the

number of cycles reached 10^7. Three specimens were tested for each of the strain condition. According to the ISO 1143:2010 Standard, hourglass samples were machined and abraded so the single-point loading method could be performed. The overall length, diameter and gage length of the specimens employed for fatigue tests were 60 mm, 3 mm and 12.2 mm, respectively. A maximum rotational speed of 2500 rpm was adopted, and the entire testing procedure was executed at room temperature. A single rotary bending-induced stress (S) was calculated based on the bending moment (M) and the section modulus (W), according to the following formulas:

$$M = \frac{S}{W} \qquad (4)$$

$$W = \frac{\pi d^3}{32} \qquad (5)$$

where d is the diameter of a specimen.

Eventually, a Wöhler curve was plotted, and the results were compared to those available in the literature.

2.3.   Surface preparation

Prior to the investigations conducted within the present study, a careful samples preparation needed to be realized as titanium surface gets easily passivated in air and the presence of a thick passive film may derange the accuracy of the collected data, especially in the case of microstructural characterizations. All of the examined specimens were progressively ground with a set of silicon carbide (SiC) sandpapers, ranging in grit from 100 to 4000. Subsequently, they were ultrasonically rinsed with isopropanol so as to remove any abrading-related residue, electro-etched, using an alcohol-based solution and dried with a stream of hot air. As a result, mirror-polished surfaces of nearly identical topographies were obtained. It should be underlined that a special attention was devoted to the polishing step. In so doing, the Struers LectroPol 5 electrolytic polisher was utilized and the conditions were as follows: the polishing time of 15 s and the applied voltage of 35 V, while the electrolyte temperature was held below 5°C. Such metallographic procedures were employed for microstructural and physicochemical surface properties investigations as well as cell-material interactions and protein-material response studies.

Due to the anisotropy the severely deformed materials tend to demonstrate, various cross-sections i.e., transverse (TCS) and longitudinal (LCS), were examined within the present thesis.

2.4. Microstructure examinations

2.4.1. SEM/EBSD

A comprehensive microstructural characterization was executed on the grounds of orientation imaging microscopy (OIM). In so doing, a FEI Quanta 3D Scanning Electron Microscope (SEM) equipped with a field emission gun and the electron backscatter diffraction (EBSD) system was used. The Inverse Pole Figure (IPF) maps were gathered for all of the HE-processed titanium rods in order to trace the microstructure evolution during hydrostatic extrusion. The initial material was used as reference. Prior to obtaining the data, a step size as well as the overall map size were adjusted so at least 1.8 million diffraction points could be recorded.

Upon completing the measurements, the maps were cropped so the comparison between the particular samples be reliable. All of the points having the Confidence Index below 0.1 were excluded from the analyses as they correspond to the nano-sized structures, whose cannot be resolved by using the EBSD method. In addition, the *grain dilation* cleanup procedure was implemented under the assumption that a single grain is defined as an area constituting at least five points, surrounded by a continuous boundary having a misorientation angle of 15°. Such a value was used in order to distinguish between LAGBs (2° - 15°) and HAGBs (> 15°). In the IPF maps, single grains were color-coded according to their crystallographic orientations relative to the sample normal direction.

While analyzing the data obtained, grain size distribution, grain boundary density, grain boundary fraction as well as misorientation angle profiles were thoughtfully studied. The size of a single grain was specified by diameter, established by calculating the total area of a grain having an assumed circular shape. In the case of grain boundary density, it was worked out as the ratio of the overall boundary length to the orientation map size. In addition, a series of parameters describing intragranular misorientation were revealed:

- KAM (*Kernel Average Misorientation*), which is determined for a given point as its mean misorientation in reference to the neighboring points.
- GAM (*Grain Average Misorientation*), which is defined similarly as the KAM parameter, though the neighboring points are restricted to the same grain.

- GOS (*Grain Orientation Spread*), which expresses the mean misorientation of all points making up for a grain.

Due to the fact that different step sizes were used for the OIM maps gathering, both the KAM and GAM parameters were normalized to the smallest step size. Such an approach was adopted as the parameters are known to be resolution-sensitive. For the sake of clarity, a graphical visualization of the EBSD-derived parameters is illustrated in Fig. 2.1.
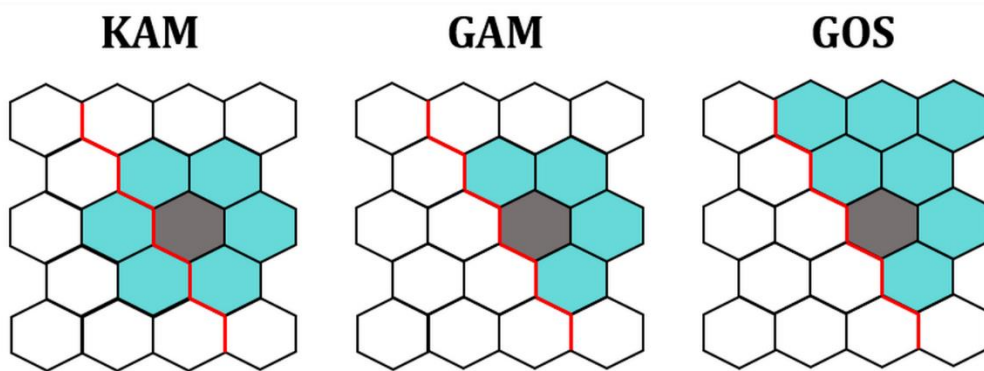
Figure 2.1. A graphical representation of the KAM, GAM and GOS parameters.

In addition, crystallographic textures were obtained based on the gathered EBSD maps since wealth of studies have confirmed complete resemblance of pole figures (PFs) derived from OIM maps and those collected by X-ray powder diffraction (XRD). In doing so, (0001) and (1120) PFs as well as ED and TD2 IPFs were revealed, assuming the convention of directions depicted in Fig. 2.2.
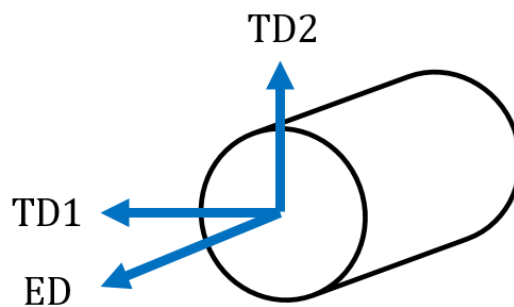
Figure 2.2. The convention of directions used to depict pole figures.

2.4.2. TEM

A Tecnai G2 SuperTWIN FEG equipped with the HAADF/STEM/EDAX attachments was used for TEM examinations. The microstructures of the HE-processed titanium samples were analyzed by setting the Bright Field (BF) mode. Furthermore, Selected Area Electron Diffraction (SAED) patterns were taken so as to confirm the crystalline nature of the obtained materials. Indexing of the diffraction images was performed applying the CSpot software, delivered by the CrystOrient company.

In order to carry out the TEM investigations, a host of thin foils of 100 nm in thickness were prepared. The sawed cross-sections were firstly abraded with SiC-based sandpapers, varying in grit from 100 to 4000, and ultrasonically cleaned in isopropanol. At this stage, the specimens were approximately 100 μm thick. Subsequently, electropolishing with the help of TenuPol-5 facility was conducted. In doing so, an electrolyte containing nitric acid (63%) mixed with methanol was used and the procedure was executed at the temperature of -20°C, while the applied voltage was set as 30 kV.

2.5. Biophysical properties examinations

Substrates, manifesting considerable differences in microstructures and crystallographic planes exposed at the surface, were the subject of research. Therefore, titanium subjected to four stages of HE along with that after two steps of rotary swaging were selected for the evaluation of biophysical properties. In addition, a comprehensive evaluation of surface properties was performed in order to understand cell-substrate interactions a severely deformed material may elicit. With regard to biological behavior, protein adsorption, cytotoxicity test as well as cell-material interactions were scrupulously investigated.

2.5.1. Wettability and surface free energy

Hydrophilicity/Hydrophobicity of the surfaces was assessed by using a DSA 100 Krüss drop shape analyzer equipped with a video capture attachment. Deionized water, ethylene glycol and diiodomethane made up for a set of liquids used for examination. A contact angle was recorded in 1 second upon placing the drop on the surface of each characterized cross-section. At least three specimens were tested. Moreover, SFE was calculated based on the Owens-Wendt-Rabel & Kaelble (OWRK) theory, according to the following equation:

$$\gamma_l(1 + cos\theta) = 2(\sqrt{\gamma_s^d \gamma_l^d} + \sqrt{\gamma_s^p \gamma_l^p}) \qquad (6)$$

where γ_l is the liquid surface tension, θ stands for the contact angle between the solid and the liquid, while γ_s^d and γ_l^d denote dispersive components of the solid and the liquid surface energies, respectively. Analogically, γ_s^p and γ_l^p designate polar components of the solid and the liquid surface energies, respectively.

2.5.2. Surface topography

An Innova Bruker Atomic Force Microscope (AFM) was utilized for surface topographical analyses. The measurements were based on the tapping mode with the use of a SiC cantilever. Due to the high-density defects typically present on the surfaces of severely deformed materials, a relatively small i.e., 5 μm × 5 μm, scanning areas were investigated. Upon the data acquisition, the images were subjected to third-order flattening. Surface roughness was computed as the arithmetical mean deviation of the profile (R_a) taken from at least three measurements. Additionally, by implementing a self-made Matlab script, a series of surface-related characteristics were revealed:

- Peak density, which expresses the number of peaks with respect to the unit area.
- Mean spacing, which is defined as the averaged spacing between the peaks.
- Surface defects density/coverage, which represents the density of defects present on the surface and is obtained by multiplying the corresponding peak densities i.e., the number of peaks per unit distance, in two orthogonal directions.

It should be stressed that all of the aforementioned parameters are derived from surface profiles. Due to the very high irregularity of the examined surfaces, while analyzing a single AFM image, 20 profiles were determined in two orthogonal directions and the results were averaged. Therefore e.g., y-Peak density stands for the mean number of peaks taken from the profiles plotted in the y direction of an image, while x-Mean spacing denotes the spacing obtained from the profiles plotted in the x direction of an image.

2.5.3. Surface chemical composition

The X-ray photoelectron spectroscopy (XPS) analyses were performed in order to find out the surface chemical composition of the HE-processed titanium samples. In doing so, a PHI VersaProbeII Scanning system using monochromatic Al Kα ($\lambda = 1486.6$ eV) radiation was used. X-rays were focused to form a 100 μm spot, while the scanning area was 400 μm × 400 μm.

High-energy resolution spectra for the Ti 2p, O 1s, C 1s and Ca 2p regions were obtained with the photoelectron take-off angle and the pass energy set to 45° and 46.95 eV, respectively. In addition, in order to maintain a constant surface potential, irrespective of the sample conductivity, a dual beam charge compensation with the use of 7 eV Ar+ ions and 1 eV electrons was ensured. The operating pressure in the analytical chamber was kept below 3×10^{-9} mbar. All of the XPS spectra were charge-referenced to the unfunctionalized, saturated carbon (C-C) C 1s peak at 285.0 eV, whereas the deconvolution procedure was carried out by using the PHI MultiPak software v. 9.9.0.1. Finally, the relative percentages of the detected elements were computed.

2.5.4. Protein adsorption

Bovine fibronectin protein (later called simply fibronectin) and bovine serum albumin (named albumin later on) were utilized for protein adsorption assays upon 10-fold dilution of the as-received solutions (Abcam company). The characterized titanium substrates were incubated at 37°C for 12 hours under a humified atmosphere of 5% CO_2. Afterwards, they were flushed in phosphate-buffered saline (PBS) so the unattached proteins were removed, while sodium lauryl sulfate (SLS) was used in order for the absorbed proteins to detach from the surface. Finally, the obtained concentrates were frozen at -20°C prior to a quantity essay conducted with the application of the Qubit Protein Assay Kit suitable for a Qubit fluorometer. The actual protein concentration within the eluted samples was normalized to the exposed surface area. At least five measurements were taken for each of the tested specimen.

2.5.5. Cytotoxicity

Despite the fact that pure titanium is generally viewed as an acclaimed biomaterial, cytotoxicity evaluation has been performed. In doing so, human umbilical vein endothelial cells (HUVECs, CC2519, Lonza), obtained by the courtesy of the University of Groningen, were adopted. Prior to cell culturing, titanium-bearing extracts were prepared by placing culture medium on a surface with a medium-to-area ratio of 1.25 ml/cm^2. The extracts were held for 24 hours at 37°C and 5% of CO_2. HUVECs were cultured in an EGM-2MV solution (CC3202, Lonza), consisting of EBM-2 Basal Medium (CC3156, Lonza) as well as EGM-2 MV supplements and growth factors (CC4147, Lonza). After reaching 90% confluence, cells were washed with sterile PBS and loosened with trypsin. Following a short-time incubation, they were neutralized with medium in order to generate a single cell suspension. Subsequently, such a solution was centrifuged for 5 minutes at 1000 rpm. Finally, the supernatant was discarded and the remaining

pellet resuspended with culture medium. Cells were stored in a 96-well plate at a density of 2.1 $\times 10^4$ cells/ml and incubated for 24 hours at 37°C in a humified atmosphere of 5% CO_2 to allow attachment. Then, the remaining culture medium was replaced by titanium-containing extracts and cell culture was maintained for additional 24 hours. The MTT assay, making use of the ability of the tetrazolium dye MTT 3-(4,5-dimethylthiazol-2-yl)-2,5-diphenyltetrazolium bromide to be reduced to insoluble formazan, was employed in order to assess cell metabolic activity. The extracts were refreshed with the MTT-containing culture medium (5 mg/ml) and incubated for 4 hours. The cells cultured in a normal medium without any additions were treated as the negative control. Consequently, dimethyl sulfoxide (DMSO) was added to each well and the plate was gently shaken for 2 minutes. The spectrophotometrical absorbance was measured at 570 nm in a microplate reader (Biotek Instruments) and an average of at least six measurements was taken for each set.

2.5.6. Cell-material interactions

HUVECs and Saos-2 osteoblast-like cells, delivered by the courtesy of the University of Groningen, were employed for cellular response studies. To the author's knowledge, biophysical properties of materials processed by means of severe plastic deformation techniques have not been examined with the use of HUVECs so far. Endothelial cells were cultured and seeded in a manner similar to that used for cytotoxicity evaluation. Osteoblasts, on the other hand, were mixed with a solution containing Dulbecco's modified Eagle's medium (DMEM), 10% fetal bovine serum (FBS) and 1% penicillin/streptomycin. Upon placing on sterilized titanium substrates, cells were kept at 37°C in a humified atmosphere of 5% CO_2. Overall, cell-material interactions were determined based on the cells' morphology and proliferation after 72 hours of incubation. All of the investigated materials were fixed with 4% paraformaldehyde solution for 10 minutes and permeabilized with 0.1% Triton X-100 (Sigma) for 7 minutes. Afterwards, they were washed with fresh PBS and carefully stored at 4°C. In the end, the cells grown on the titanium surfaces were stained with the use of FITC-phalloidin (Sigma) and DAPI (Sigma) so cell F-actin fibers of cytoskeleton and cell nuclei, respectively, could be observable. Microstructural analyses were performed by using a confocal laser scanning microscopy (CLSM) Stellaris 8 Leica Microsystems. The captured images were finally processed by employing the LAS X software.

3.   The aim of the research

A meticulous literature review has testified that an almost limitless potential within the processes of severe plastic deformation should be taken advantage of. With respect to pure titanium, its insufficient strength may be easily compensated for once heavy strains are imposed. As a consequence, any processed material, exhibiting a series of outstanding biophysical and mechanical characteristics could possibly replace the conventional alloys used in various branches of medicine.

Given that the method of hydrostatic extrusion has proven itself very effective in increasing the strength of various materials, within the present study, the technique was chosen to enhance pure titanium's mechanical properties with a final goal to produce a material, whose properties will be promising from the point of view of biomedical applications.

The main goal of the research was to find the clear origin of superior mechanical and biophysical properties observed in commercially pure titanium processed by means of both conventional and unconventional severe plastic deformation techniques. The mechanism mediating such properties remains incompletely understood.

Thesis:

Increased strength of severely deformed titanium originates from microstructure refinement, whereas its biophysical properties are governed by the synergistic effect of crystallographic orientation of grains and the presence of surface irregularities.

4. Results and discussion

4.1. Microstructure

The IPF maps as well as the grain size distributions and the misorientation angle profiles determined for the as-delivered billet are depicted in Fig. 4.1. For the sake of brevity, the microstructure of a material in this particular state is illustrated only to highlight the remarkable changes in microstructure triggered by applying the HE method.
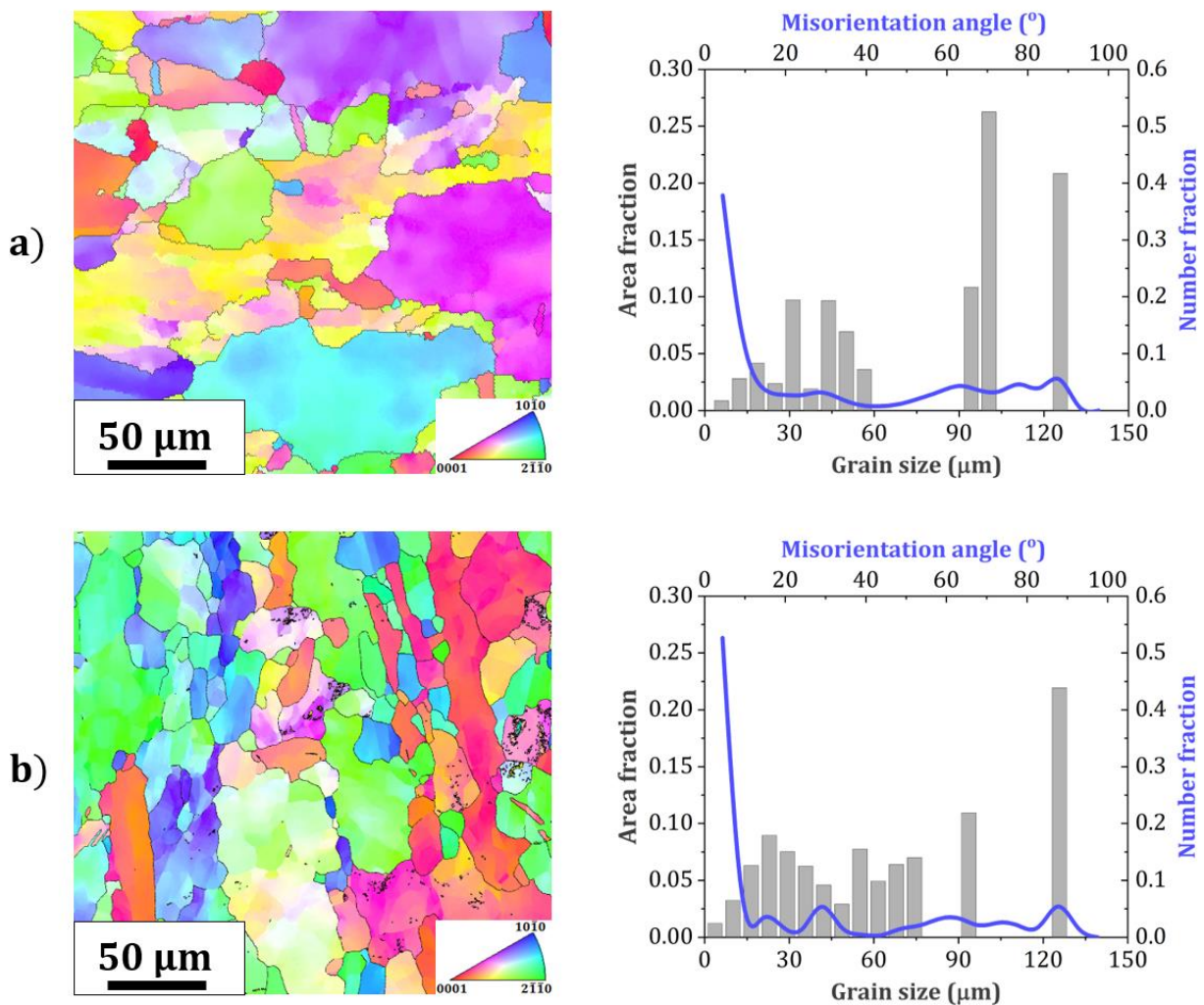
Fig. 4.1. OIM maps and the corresponding grain size distributions combined with misorientation angle profiles taken from the a) transverse, b) longitudinal cross-section of the as-received material.

Irrespective of the cross-section examined, the microstructure of the as-received material was distinctly coarse-grained and non-uniform. The mean grain size of 79.31 μm ± 40.95 μm and 66.17 μm ± 42.07 μm was measured on the TCS and LCS, respectively. Coarse grains were bordered by HABGs, yet contained a significant substructure as reflected by clearly noticeable

differences in crystallographic orientation between the areas within single grains, misorientation angle profiles and the values of LAGB fraction i.e., 0.54 and 0.62 for the TCS and LCS, respectively. In addition, some twin boundaries were also present in the volume of a material. However, it is likely that twins originated from preparation of specimens used for the EBSD measurements since misorientation angle profiles did not reveal any peaks corresponding to the characteristic tensile or compression twins.

The evolution of titanium's microstructure during HE is depicted in Figs. 4.2-4.8. The analysis was carried out for the materials characterized by an accumulated plastic strain ranging from 0.9 (regarded as very low) to 2.82 (intermediate), whereas the initial, homogenized material was used as reference. Furthermore, a special attention was devoted to the final material i.e., deformed to the cumulative strain of 3.23 (herein considered high). Its EBSD-gathered microstructure is shown in Figs. 4.10 and 4.11. Overall, the IPF maps with the corresponding distributions of grain size as well as the misorientation angle profiles constitute the basis for establishing the origin of enhanced mechanical strength observed in the HE-treated titanium.

4.1.1. Initial material ($\varepsilon = 0$)

By virtue of undergoing homogenization heat treatment, the initial material was made up of well-developed, equiaxed coarse grains, regardless of the investigated cross-section, as displayed in Fig. 4.2. The mean grain size evaluated on the TCS and the LCS was 33.25 μm ± 12.85 μm and 33.76 μm ± 14.02 μm, respectively, indicating markedly homogeneous microstructure. It is worth stressing out that a remarkable grain refinement was accomplished already at this stage of processing, even though it was preceded by a recrystallization-induced grain growth. As a matter of fact, two-fold drop in the mean grain size value was observed as compared to the material in the as-received condition. Moreover, high share of HAGBs, originating from the pre-deformation annealing, was identified, whereas no traces of twin boundaries were found.
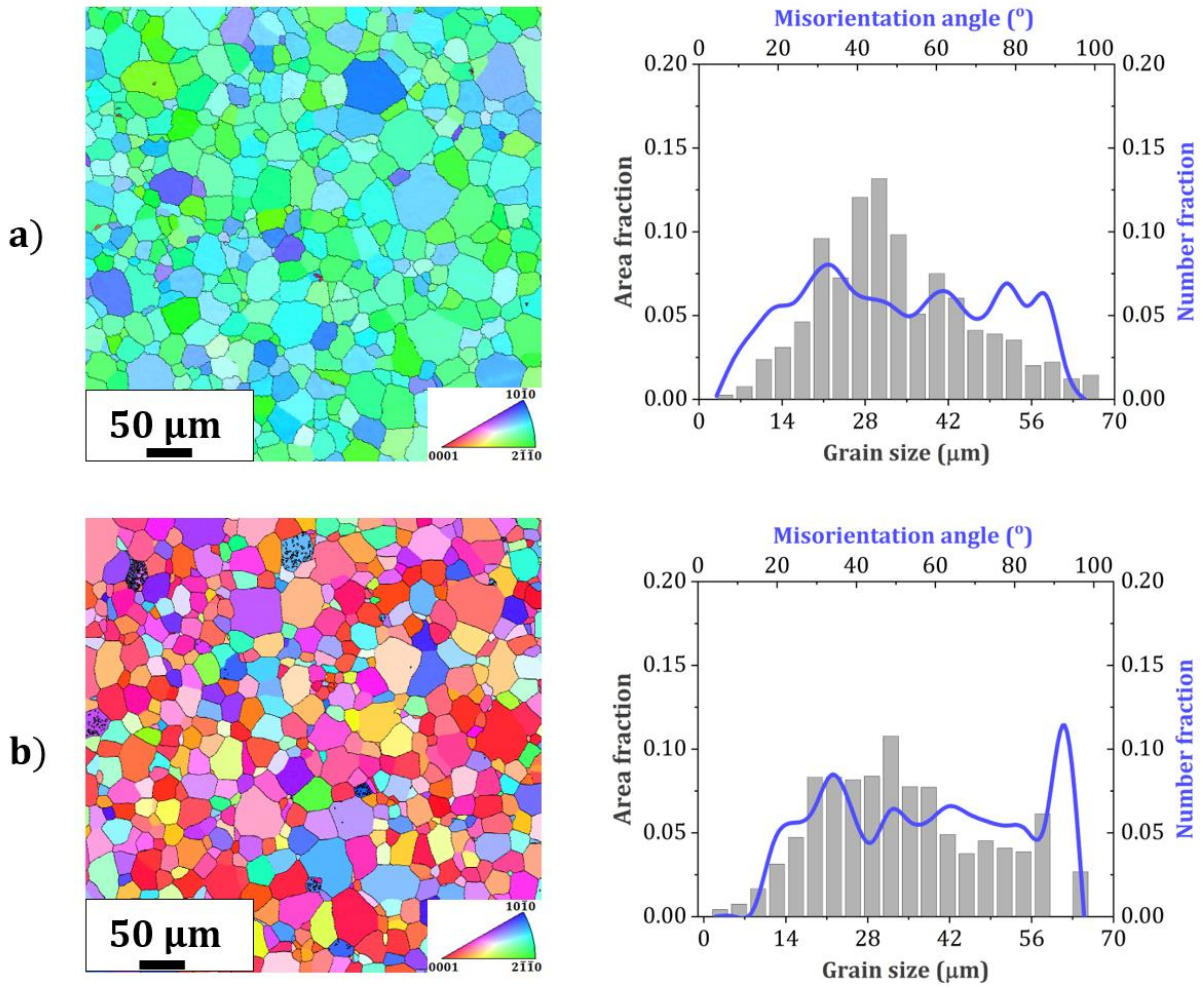
Fig. 4.2. OIM maps and the corresponding grain size distributions combined with misorientation angle profiles taken from the a) transverse, b) longitudinal cross-section of the initial material.

Microstructural homogeneity of the initial material was additionally confirmed by a thorough investigation of the OIM-derived parameters i.e., GOS, KAM and GAM, listed in Table 4.1. Their low values are typical of ordinary, recrystallized microstructures. Overall, the only major difference between the analyzed cross-sections was the crystallographic orientation of grains.

Table 4.1. Microstructural parameters computed for the initial material

Cross-section	*GOS* (°)	*KAM* (°)	*GAM* (°)
Transverse	0.44	0.07	0.05
Longitudinal	0.67	0.10	0.09

4.1.2. Very low strains ($\varepsilon = 0.9$)

The IPF maps collected for the TCS (Fig. 4.3), gives a clear evidence of grain refinement at the early stage of processing. The observation is consonant with the literature data suggesting it is the first step of HE that is mainly responsible for downsizing of the microstructure in a variety of fcc and hcp metals [53], [55]. The mean grain size on the TCS and the LCS was measured to be 22.54 μm ± 14.61 μm and 45.69 μm ± 35.09 μm, respectively, indicating highly anisotropic nature of the examined material. Although the grain size distribution was broad as coarse grains prevailed, fine-grained fraction began to form as well. Approximately 1.5% of the TCS and 3.6% of the LCS were filled with grains having the mean size smaller than 2 μm.
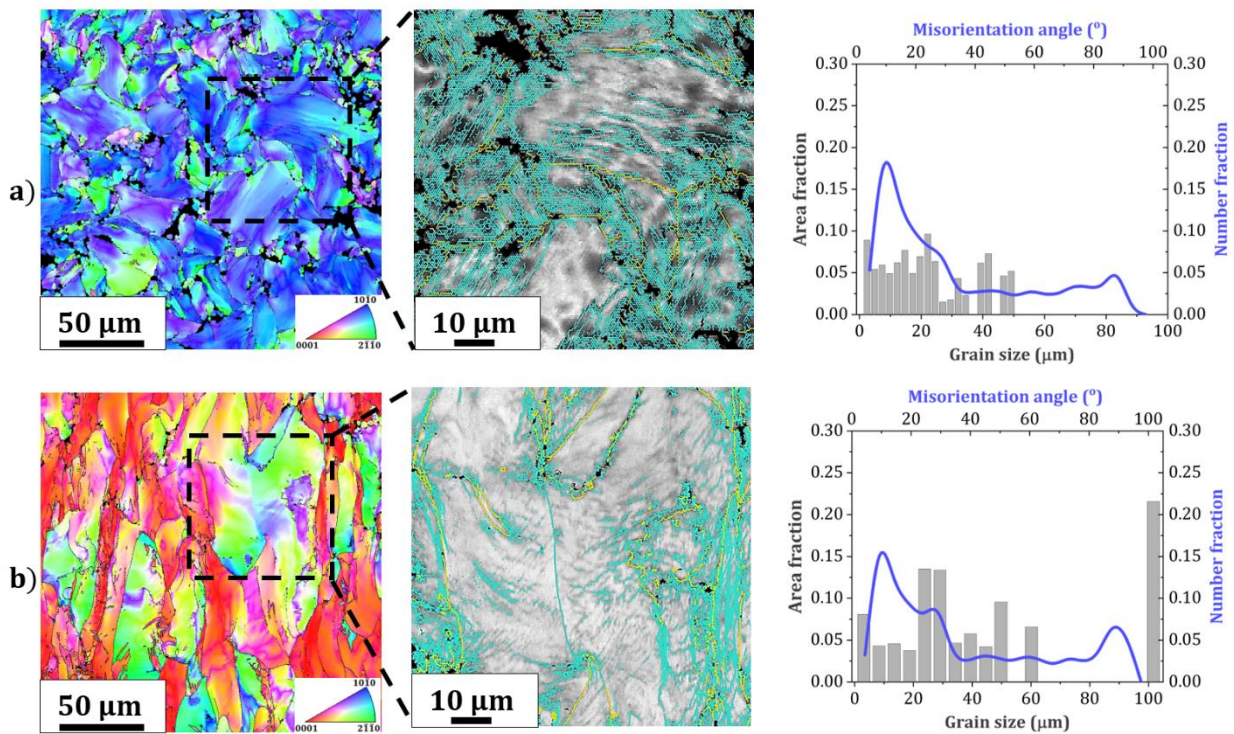
Fig. 4.3. OIM maps and the corresponding grain size distributions combined with misorientation angle profiles taken from the a) transverse, b) longitudinal cross-section of the material deformed at ε = 0.9. Grain boundary maps shown in the middle were collected from the highlighted area on the OIM maps. Blue and yellow color depict LAGB and HAGB, respectively.

Rather surprisingly, grain coarsening was observed on the LCS, a phenomenon relatively rare in the case of severely deformed materials. It may be attributed to the complexity of deformation as well as the high surface activity of a processed material [89]. At the same time, it should be noted that a tremendous amount of microstructural defects was generated, as indicated by the grain boundary maps, the misorientation angle profiles and the TEM images taken in the BF mode (Fig. 4.4). The heterogeneous contrast coming from the selected grains/subgrains was

a result of their various crystallographic orientations as well as the presence of lattice defects. Deformation-induced LAGBs were formed within grain interiors with a strong tendency to cluster near already-existing HAGBs. It may be noticed that some of the unconnected LAGBs were trapped inside coarse grains, while dislocations started to organize into incompletely-built arrays of defects, resembling dislocation walls and cells. The formation of irregularly-shaped ultrafine grains/subgrains, containing high-density dislocations and surrounded by fuzzy, poor-lineated boundaries, needs to be mentioned. The grain shape, in general, was hardly discernable. In addition, the exact locations of HAGBs were often hard to determine since these boundaries have not been completely developed. Moreover, the existence of parent, barely refined grains ought to be underlined as well (Fig. 4.3b). The grains on the LCS displayed a tendency for elongation in a particular direction, overlapping with the extrusion direction (ED).
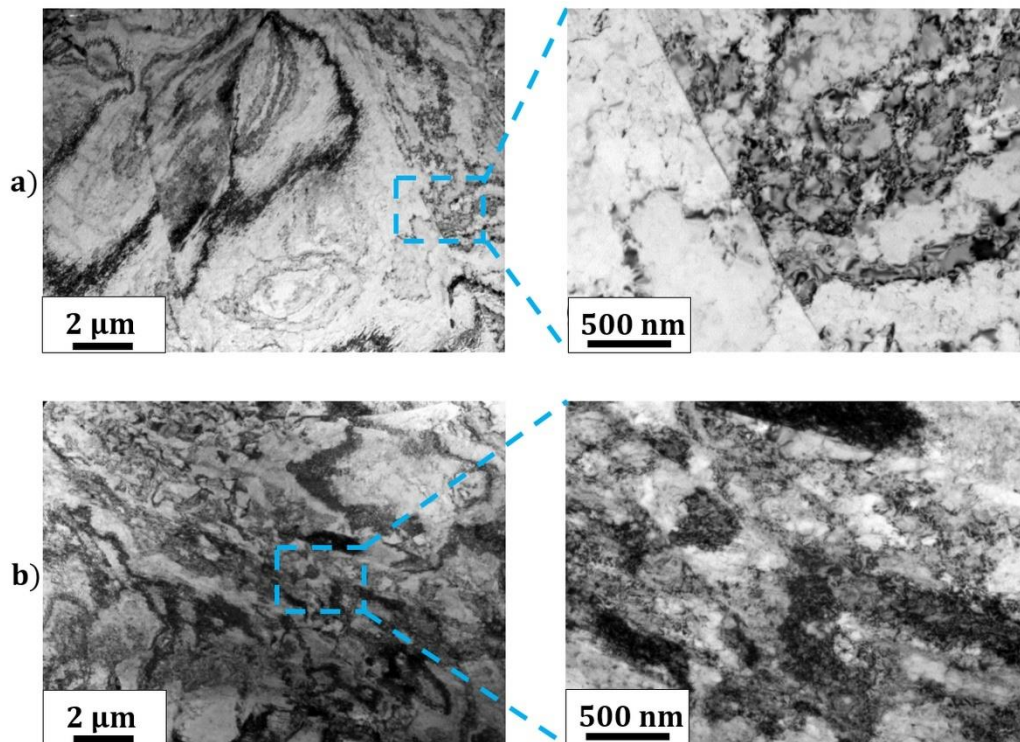
Fig. 4.4. TEM/BF images taken from the a) transverse, b) longitudinal cross-section of the material deformed at ε = 0.9. High-magnification images, shown on the right side, were collected from the blue-colored area drawn on low-magnification images, displayed on the left side.

Overall, it could be stated that the microstructure of the HE-processed titanium, deformed at very low strains, is of substructure-type as filled with a great deal of microstructural defects.

Table 3.2. Microstructural parameters computed for the material deformed at ε = 0.9.

Cross-section	GOS (°)	KAM (°)	GAM (°)
Transverse	10.71	0.74	0.38
Longitudinal	18.3	1.42	0.70

The claim is fully supported by high values of the GOS, GAM and KAM parameters, listed in Table 4.2, as well as the total fraction of LAGBs, being 0.79 and 0.82 on the TCS and the LCS, respectively.

4.1.3. Low strains ($\varepsilon = 1.54$)

The material obtained owing to an application of low strains was distinctly heterogeneous and highly disordered as revealed by the IPF maps, shown in Fig. 4.5. It may be seen that the microstructure was composed of wavy grains on the TCS and lengthened ones on the LCS. In either case, coarse-grained fraction was dominating, though fine grains covered approximately 5.5% of the LCS and 13.2% of the TCS, marking a considerable increase in comparison with the material processed at very low strains. Microstructural refinement progressed as demonstrated by the mean grain size plummeting below 20 μm for the TCS and 30 μm for the LCS. Furthermore, TEM/BF images, displayed in Fig. 4.6, have proven that within large grains, considerable substructure was developed, regardless of the inspected cross-section. Dislocation-type defects e.g., dislocation tangles of statistically stored dislocations, tended to concentrate at boundaries surrounding coarse grains and so did the elongated, ultrafine grains/subgrains. Some of LAGBs were already transformed into HAGBs, as revealed by a decreasing share of the former with regard to the material fabricated at very low strains i.e., 0.74 and 0.80 on the TCS and the LCS, respectively. Additionally, GBs began to extend throughout the entire grain interior, indicating the grain subdivision process to take place. What deserves highlighting is that large grains contained cell blocks, the type of defects defined as subgrains comprised of dislocation cells. Simultaneously, some regions of the coarse-grained fraction exhibited local bending contours, a clear sign of heavily straining. Moreover, the presence of nearly dislocation-free grains/subgrains with nearly delineated, straight boundaries ought to be noted. Generally, dislocation density strongly varied since individual dislocation segments as well as dense dislocation clusters could be distinguished. In addition to high-density dislocations, other microstructural defects such as twins and triple points were also observed, as illustrated in Fig. 4.7.
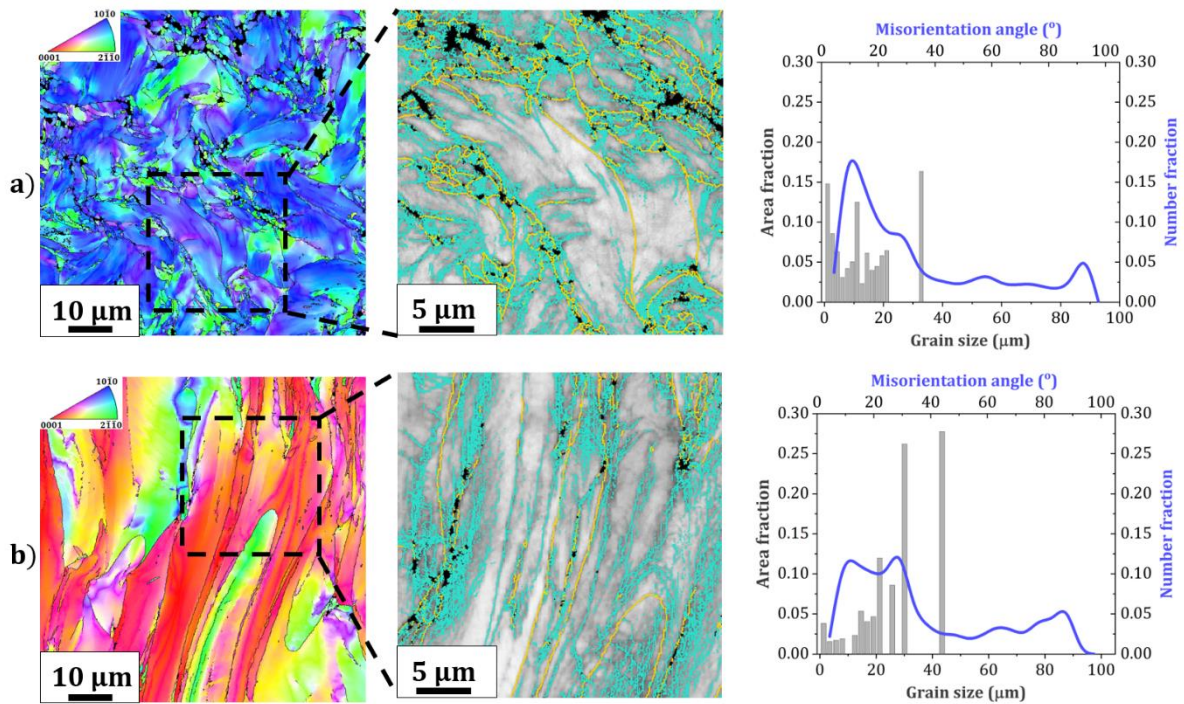
Fig. 4.5. OIM maps and the corresponding grain size distributions combined with misorientation angle profiles taken from the a) transverse, b) longitudinal cross-section of the material deformed at ε = 1.54. Grain boundary maps shown in the middle were collected from the highlighted area on the OIM maps. Blue and yellow color depict LAGB and HAGB, respectively.
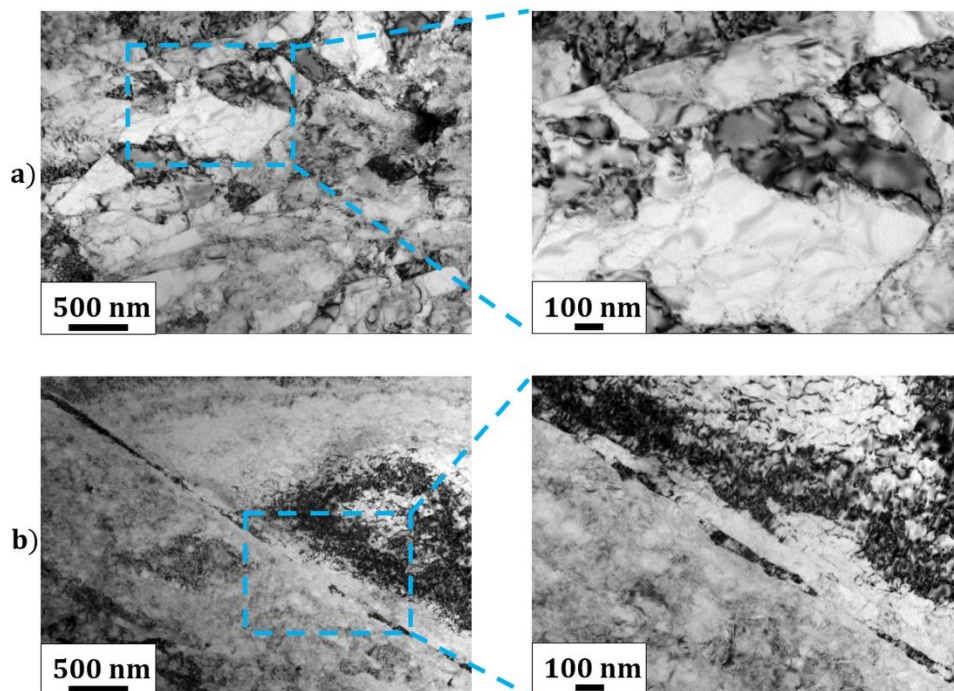
Fig. 4.6. TEM/BF images taken from the a) transverse, b) longitudinal cross-section of the material deformed at ε = 1.54. High-magnification images, shown on the right side, were collected from the blue-colored area drawn on low-magnification images, displayed on the left side.

Cross-section	GOS (°)	KAM (°)	GAM (°)
Transverse	14.65	2.17	1.47
Longitudinal	20.17	1.66	1.08

The misorientation angle profile plotted for the LCS and TCS showed the preferential misorientation peak around 86°, implying the occurrence of $\{10\bar{1}2\}$ twinning. At the same time, no frequency peak around 56° was noticed, suggesting that $\{10\bar{1}1\}$ twinning, typical for titanium-based materials, has not taken place. The abundance of deformation-induced defects is also substantiated by the values of GOS, KAM and GAM parameters, placed in Table 4.3.
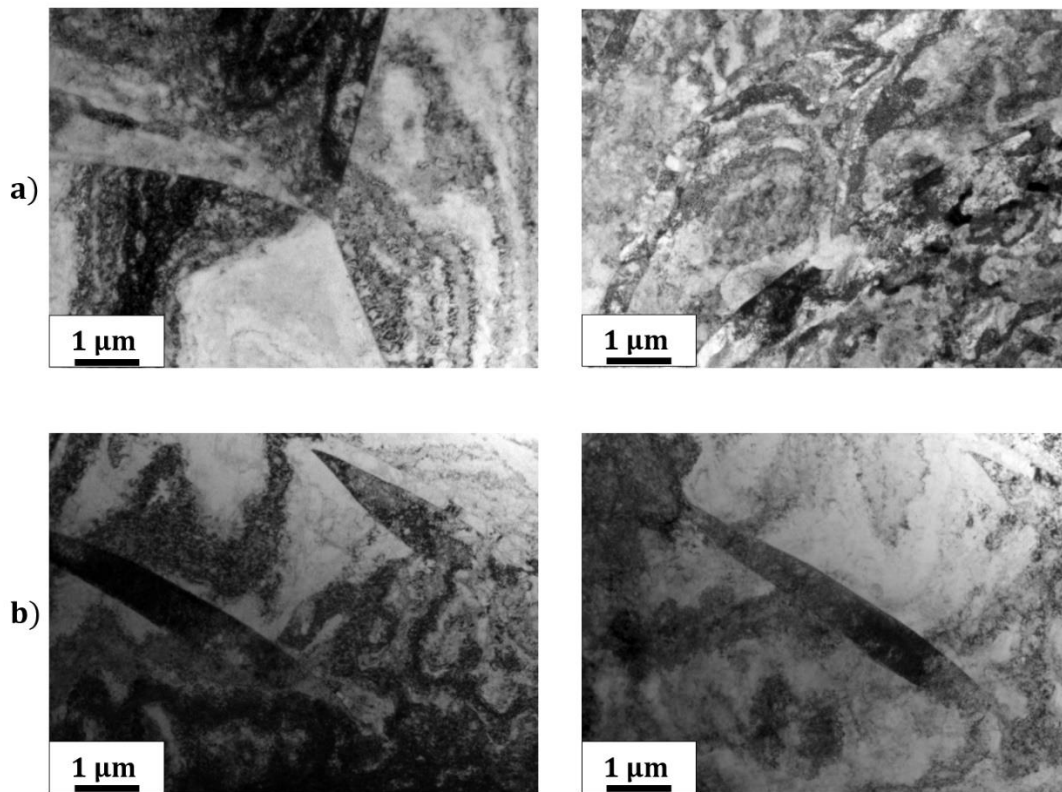
Figure 4.7. a) triple points, b) twins observed within the microstructure of titanium processed at the strain of 1.5.

4.1.4. Intermediate strains ($\varepsilon = 2.44$)

During additional extrusions, the material was extensively refined as reflected by the grain size distributions, skewing towards small grains, and a thorough examination of the IPF maps, illustrated in Fig. 4.8. The mean grain size measured on the TCS and LCS was equaled to 6.06 μm ± 5.67 μm and 17.75 μm ± 14.55 μm, respectively, hitting a spectacular decrease once again.

However, the evidently bimodal character of the as-processed microstructure was confirmed to persist. Taking the LCS into consideration, it may be seen that elongated grains were alternating with thin bands of ultrafine/nanosized grains. In addition, the boundaries between single grains became slightly sharper and delineated, albeit the overall share of HAGBs have not outbalanced that of LAGBs. The fraction of the latter, determined on the TCS and LCS, was 0.68 and 0.78, respectively. Some of LAGBs were arranged into arrays of branched, parallel boundaries. It may be declared that the LCS have experienced a rather small drop of the LAGB amount, in comparison to the materials deformed at lower strains, although, at the same time, the lengthened grains got markedly narrower and the share of fine grains raised significantly. Approximately 25.9% of the TCS and 19.7% of the LCS were comprised of grains smaller than 2 μm in size. TEM experiments have additionally proven the existence of submicron-sized or nanocrystalline features in the material. As displayed in Fig. 4.9, a number of grains/subgrains were variously oriented, differently shaped and accumulated at wavy boundaries. Some of the grains/subgrains were almost defects-free, while the others contained high density of dislocation-type structures e.g., dislocation cells.
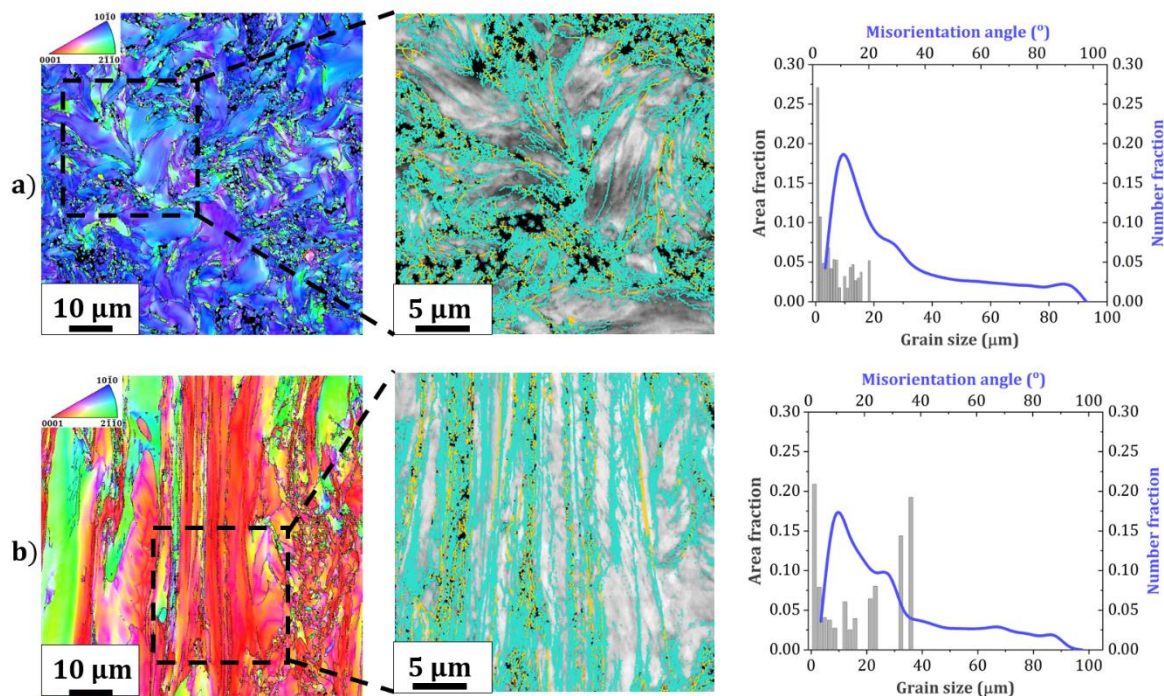
Fig. 4.8. OIM maps and the corresponding grain size distributions combined with misorientation angle profiles taken from the a) transverse, b) longitudinal cross-section of the material deformed at ε = 2.44. Grain boundary maps shown in the middle were collected from the highlighted area on the OIM maps. Blue and yellow color depict LAGB and HAGB, respectively.
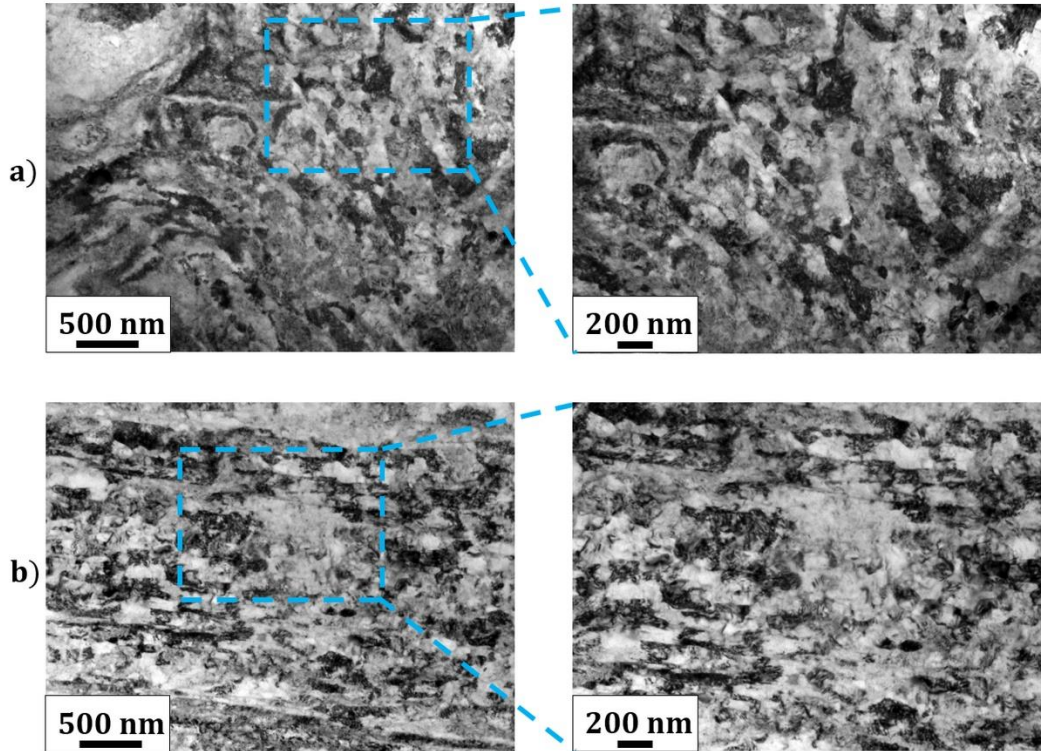
Fig. 4.9. TEM/BF images taken from the a) transverse, b) longitudinal cross-section of the material deformed at ε = 2.44. High-magnification images, shown on the right side, were collected from the blue-colored area drawn on low-magnification images, displayed on the left side.

The presence of twins was not detected at the subgrain level, implicating that the twinning deformation mode has been suppressed, yet the process might have led to the generation of small-sized, elongated grains surrounded by distinct boundaries. Nonetheless, a weak peak around 86°, stemming from $\{10\bar{1}2\}$ twins was observable on the misorientation angle profiles. It is also worth mentioning that on either of the examined cross-sections, some of the grains retained nearly equiaxed shape.

Table 4.4. Microstructural parameters computed for the material deformed at ε = 2.44.

Cross-section	GOS (°)	KAM (°)	GAM (°)
Transverse	13.81	2.59	1.62
Longitudinal	17.65	2.42	1.81

Generally, the HE-treated titanium manufactured at intermediate strains should be viewed as made out of a strong substructure rather than well-developed clusters of grains. Such a statement is backed up by the continuously high values of the KAM, GAM and GOS parameters, listed in Table 4.4. However, considering a slight GOS decline with respect to that

of the material processed at low strain, it is fair to say that the defect storage has just reached the saturation limit.

4.1.5. High strains ($\varepsilon = 3.23$)

Strains elicited during the last stage of the HE processing combined with RS caused the microstructure to be substantially rebuilt, though its character remained heterogeneous, as observed on the IPF maps, illustrated with the corresponding grain size distributions as well as misorientation angle profiles in Fig. 4.10. The mean grain size measured on the TCS and LCS was 3.93 μm ± 3.85 μm and 12.94 μm ± 9.06 μm, respectively. The microstructure, examined on the TCS, consisted of wavy, large grains, featuring substantial orientation gradients, mixed with refined grain agglomerates, bordered mainly by HAGBs. Taking the LCS into consideration, it might be seen that elongated, coarse grains were intensely narrowed and aligned with the ED, thus creating a lamellar/banded microstructure. Obviously, the grain shape mirrored the induced deformation route. By comparison to the materials deformed at low or intermediate strains, the bands' thickness got substantially diminished as a few reached the submicron range. In addition, coarse, lengthened grains got separated from one another by nanograined/ultrafine-grained fraction. Overall, fine grains spanned over approximately 31.6% of the TCS and 17.2% of the LCS. Surprisingly, elongated grains were present on both of the investigated cross-sections. It may be seen that the IPF maps were filled with plenty of black areas correlating to the Confidence Index value lower than 0.1 and confirming the presence of the extraordinarily high content of nano-sized features, undetectable for the EBSD technique. As a matter of fact, the density of microstructural defects was very high, as pointed by the grain boundary maps and TEM/BF images, depicted in Fig. 4.11. Internal grain structure was verified since grains containing dislocation walls, dislocation tangles or dislocation cells could be readily noticed. Equiaxed, nearly defects-free grains of nano-scaled size were also shaped within the microstructure. It may be supposed that the most extremely refined grains did not contain any dislocation-type defects as these had been absorbed into the adjacent grain boundaries. Actually, ultrafine grains and nanograins could be observed in the vicinity of HAGBs surrounding coarse, less fragmented grains. In general, most of the deformation-induced defects were found close to the well-developed, sharp, delineated HAGBs, whose fraction, especially when regarding the TCS, increased significantly. The share of LAGBs determined on the TCS and the LCS was 0.49 and 0.76, respectively, confirming that the LAGB-to-HAGB transformation had still occurred. Grain boundary network was diversified as well-developed, sharp, straight segments were entangled with fuzzy, poorly-lineated ones.
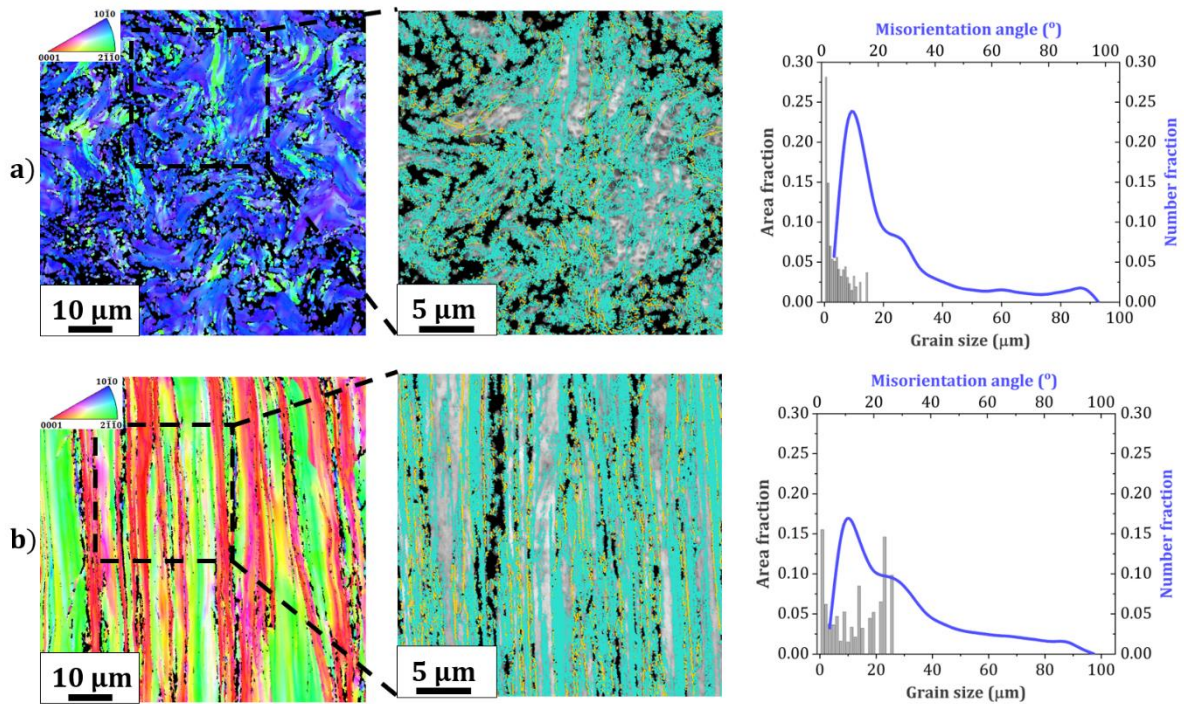
Fig. 4.10. OIM maps and the corresponding grain size distributions combined with misorientation angle profiles taken from the a) transverse, b) longitudinal cross-section of the material deformed at ε = 3.23. Grain boundary maps shown in the middle were collected from the highlighted area on the OIM maps. Blue and yellow color depict LAGB and HAGB, respectively.
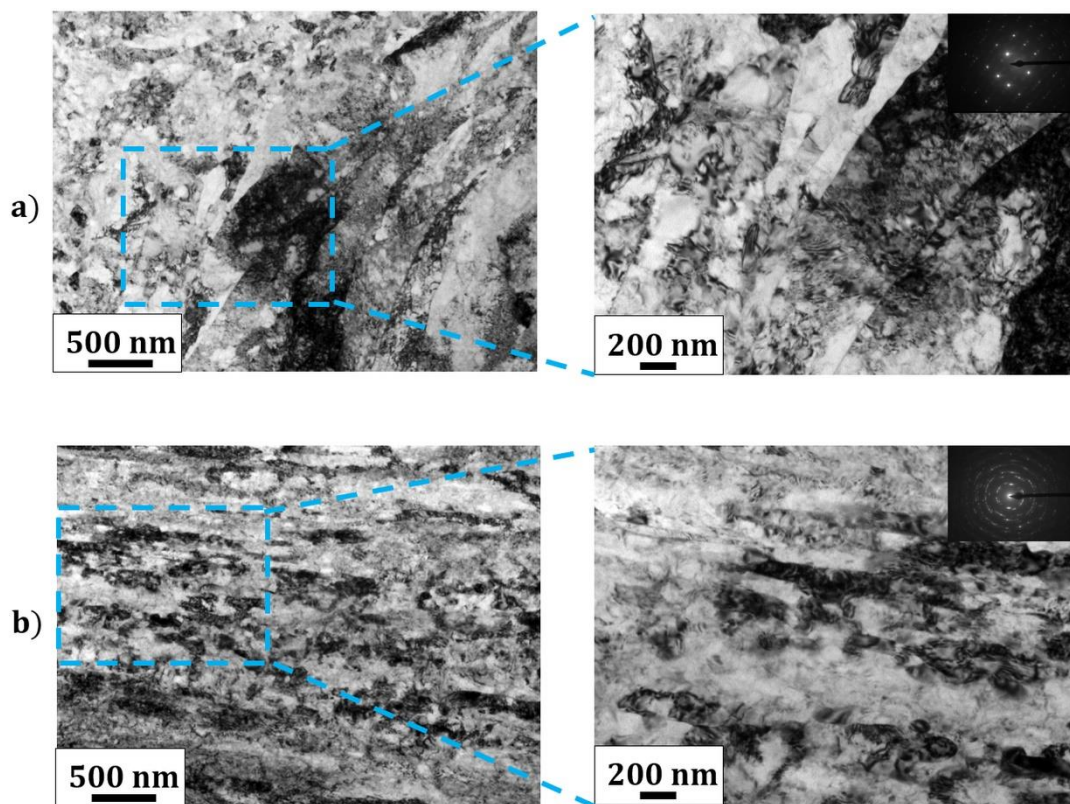
Fig. 4.11. TEM/BF images taken from the a) transverse, b) longitudinal cross-section of the material deformed at ε = 3.23. High-magnification images, shown on the right side, were collected from the blue-colored area drawn on low-magnification images, displayed on the left side.

The SAED patterns confirmed the material to be polycrystalline and filled with a vast amount of HAGBs. What should also be stressed out is that no evidence of twin boundaries was found on either of the inspected cross-sections. The values of the KAM and GAM parameters, listed in Table 4.5., prove the final microstructure to be highly disordered, while the value of GOS points to not only the microstructure's inhomogeneity but also the saturation of defects. The continuous decrease of GOS can be also explained by the fact that in smaller grains there is a smaller orientation scattering.

Table 4.5. Microstructural parameters computed for the material deformed at ε = 3.23.

Cross-section	GOS (°)	KAM (°)	GAM (°)
Transverse	12.42	2.95	1.98
Longitudinal	16.24	2.71	1.96

In order to address the complexity of deformation during the multistage HE, misorientation angle gradients within typical, HAGB-enclosed grains observed on the TCS and LCS are provided in Fig. 4.12 and Fig. 4.13, respectively. Two lines were arbitrarily plotted along different paths i.e., L1, representing the direction parallel to the grain elongation and L2, perpendicular to the L1 profile. Afterwards, point-to-origin and point-to-point misorientations were cautiously inspected.

With regard to the TCS, a couple of substantial point-to-origin misorientation jumps, ranging in magnitude from 2.4° to 13.6°, were noted along the L1 lines. Such a behavior confirms the formation of differently oriented subgrains, cell structures as well as sub-boundaries within a grain and is typical of materials treated by various plastic deformation techniques [89], [90]. In general, the inhomogeneity of the HE-processed titanium was proven once again as the maximum cumulative misorientation across the grains chosen for the examination varied considerably and so did the character of the relative misorientation profiles. While the continuous rise of the point-to-origin misorientation gradient within a grain originates from the accumulation of LAGBs over an analyzed distance, the increase in misorientation and its subsequent drop confirms that a particular grain is characterized by significant strain heterogeneity. On the other hand, the point-to-point misorientation profiles generally fluctuated below 5°, yet a few misorientation jumps, exceeding 10° could be seen. It indicates that the developing boundaries are formed parallel to the already existing ones and that the difference in lattice orientation between the neighboring subgrains is locally large [91].
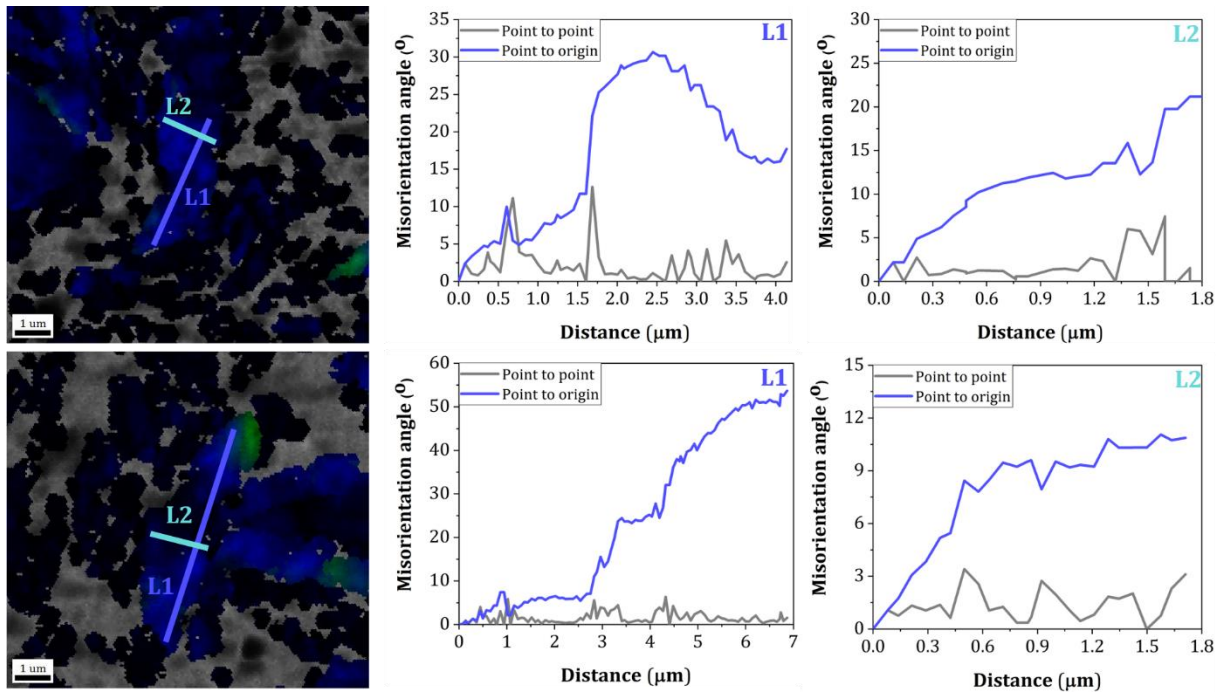
Fig. 4.12. Point-to-point and point-to-origin misorientation distributions taken for two arbitrarily chosen grains on a transverse cross-section of the titanium deformed at ε = 3.23. Distributions in the middle refer to the L1 line, while these on the right side correspond to the L2 line.

Interestingly, when taking the L2 lines into consideration, it may be observed that the cumulative misorientations measured on the lines perpendicular to the grain elongation were notably smaller than those assessed on a grain major axis i.e., the L1 lines. Comparable findings were observed for pure titanium processed by the ECAP technique and, in crude terms, they evidence a significant substructure, whereas the opposite effect would substantiate the formation of microbands within a coarse grain [89].

In the case of the LCS, there were apparent similarities to the TCS noticed except for the distinctive plateau on the L1 profile, referring to the presence of a well-developed, banded region characterized by an almost constant misorientation. In addition, the course of the L2 profiles ought to be highlighted as well. Naturally, the accumulation of misorientation nearby well-defined HAGBs proves that misorientation gradients close to a grain boundary are larger than those inside the grains. The observation is fully consistent with the TEM data, revealing that the higher density of dislocations could be found in the areas adjacent to HAGBs. Overall, the study of long-range misorientation gradients confirmed the microstructural defects to be encompassed within the coarse grains.
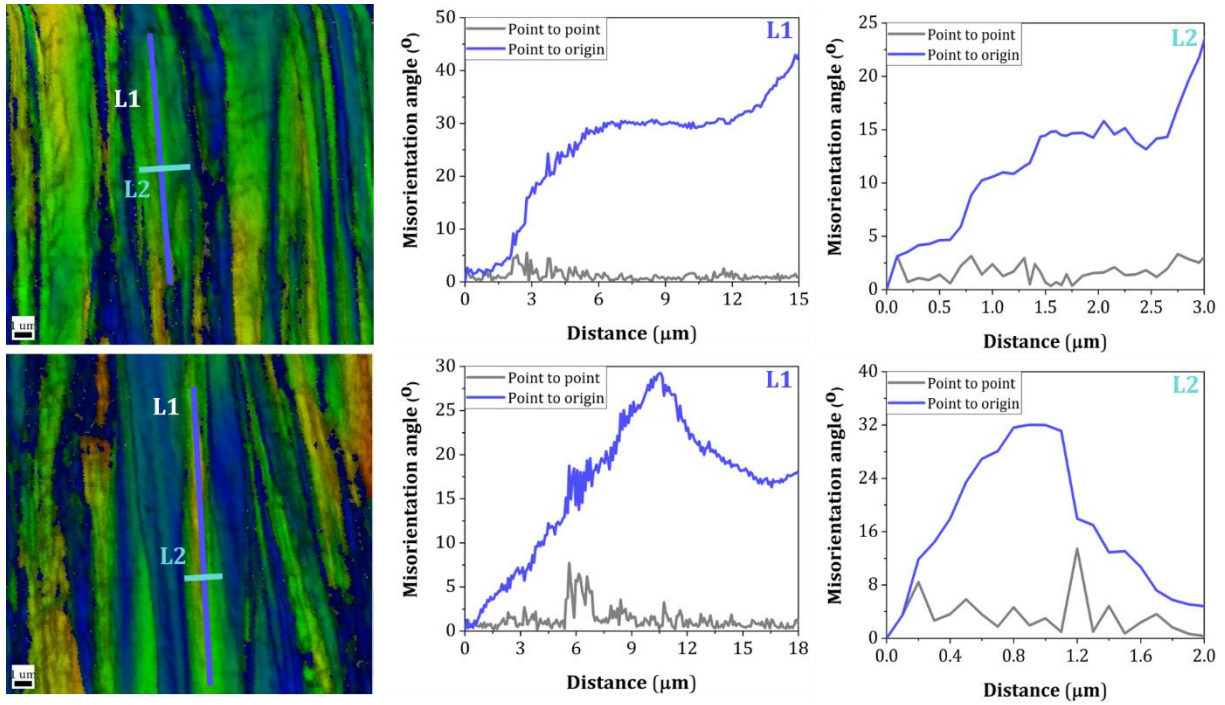
Fig. 4.13. Point-to-point and point-to-origin misorientation distributions taken for two arbitrarily chosen grains on a longitudinal cross-section of the titanium deformed at at ε = 3.23. Distributions in the middle refer to the L1 line, while these on the right side correspond to the L2 line.

4.1.6. Low-temperature heat treatment

Minor alterations in the microstructure of the final material occurred upon heat treatment at 200°C with stress relieving representing the most striking change. The phenomenon was proven by considerably lower values of the KAM and GAM parameters (Table 4.6), with comparison to the material processed at high strain.

Table 4.6. Microstructural parameters computed for the material deformed at ε = 3.23 and heat-treated.

Cross-section	GOS (°)	KAM (°)	GAM (°)
Transverse	14.31	2.68	1.56
Longitudinal	15.92	1.77	1.44

In addition, while taking the TCS into account, two-fold increase of the mean grain size was noted, but, at the same time, the total fraction of either HAGBs or LAGBs has not varied. Interestingly, no significant change in the mean grain size measured on the LCS was registered. As seen in the IPF maps, shown in Fig. 4.14, a vast amount of black areas, corresponding to the CI below the value of 0.1, was still present, evidencing the abundance of nano-sized features

within the material volume. Low- and high-magnification TEM/BF images, depicted in Fig. 4.15 and Fig. 4.16, respectively, give clear proof of the unremitting microstructural inhomogeneity. During low-temperature heat treatment, dislocation-based defects had not been annealed out, since dislocation cells or tangles could still be easily observed. However, it may be noticed that some of the boundaries between grains/subgrains became slightly sharper. In addition, the SAED patterns proved the material to be nanocrystalline.
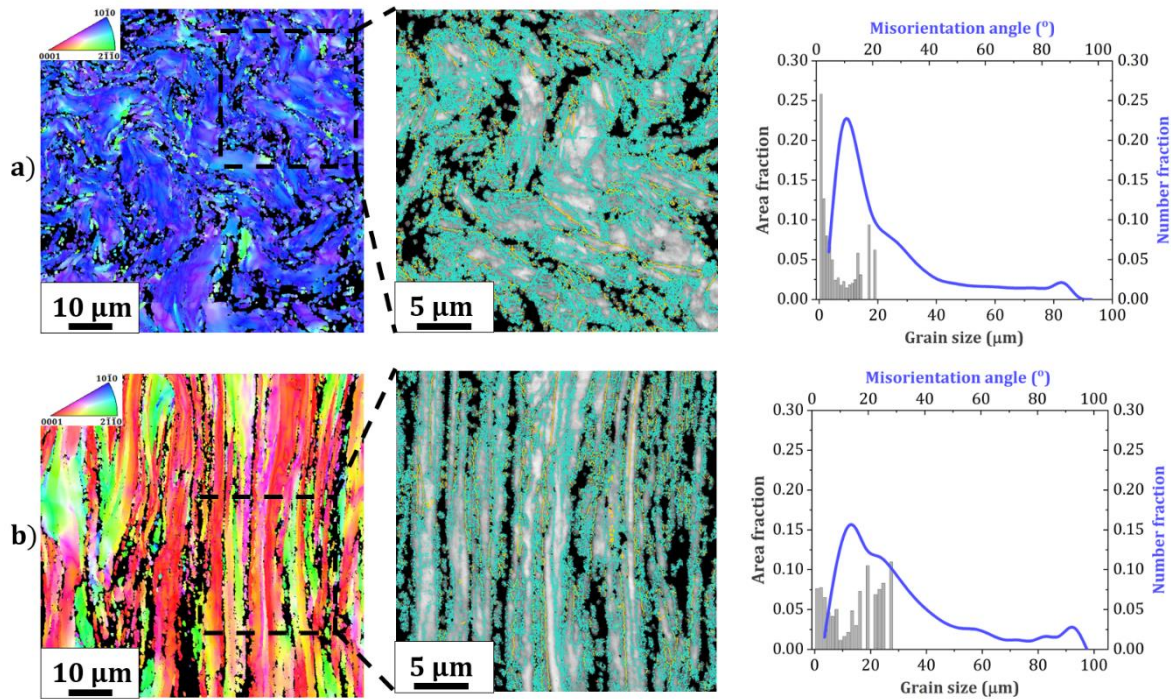
Fig. 4.14. OIM maps and the corresponding grain size distributions combined with misorientation angle profiles taken from the a) transverse, b) longitudinal cross-section of the material deformed at ε = 3.23 and heat-treated. Grain boundary maps shown in the middle were collected from the highlighted area on the OIM maps. Blue and yellow color depict LAGB and HAGB, respectively.
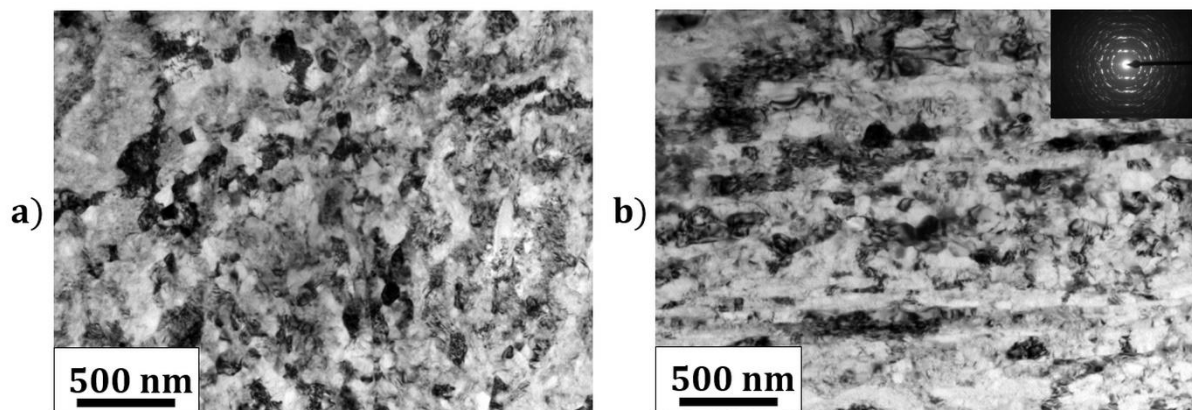
Fig. 4.15. Low-magnification TEM/BF images taken from the a) transverse, b) longitudinal cross-section of the material deformed at ε = 3.23 and heat-treated.
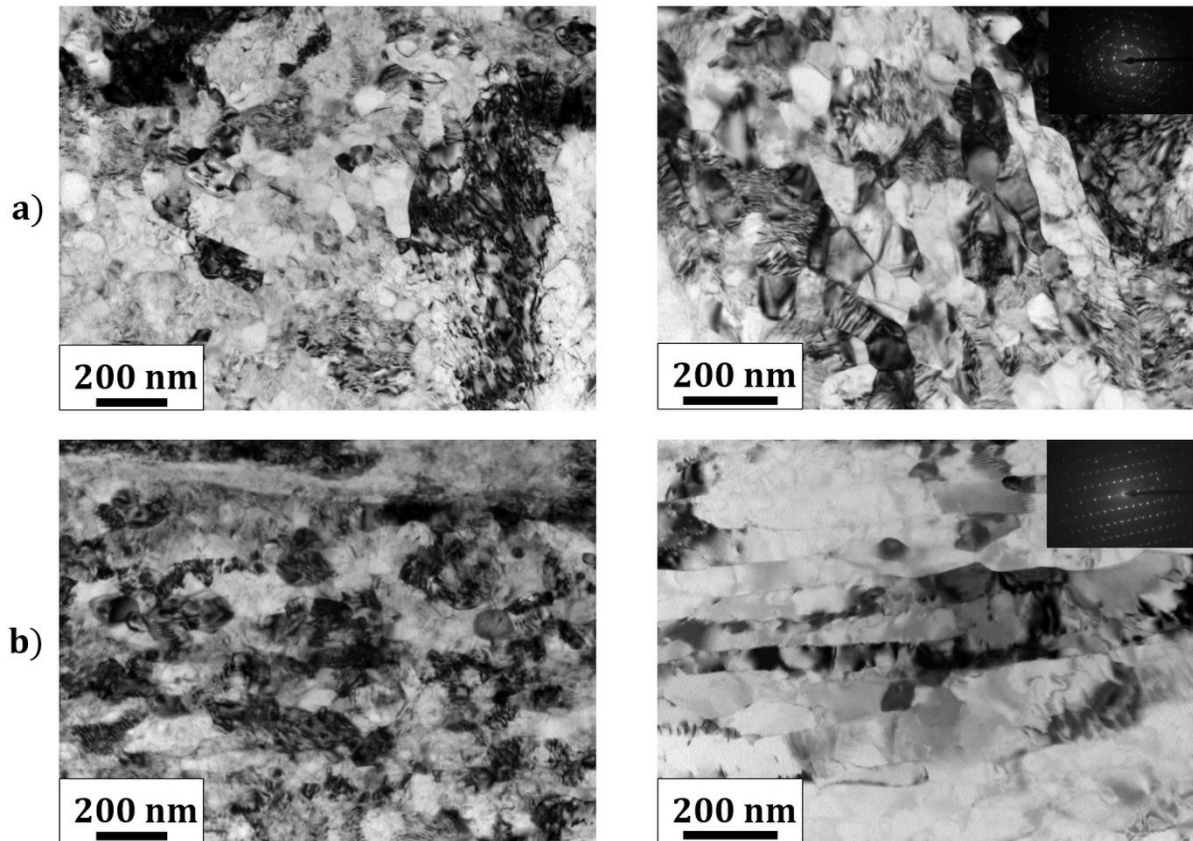
Fig. 4.16. High-magnification TEM/BF images taken from the a) transverse, b) longitudinal cross-section of the material deformed at ε = 3.23 and heat-treated.

4.1.7. Microstructural evolution during HE

The initial, coarse-grained, recrystallized microstructure got rebuilt and markedly fragmented when the multistage HE process was implemented. As demonstrated by EBSD and TEM data, deformation of pure titanium during HE is complex and non-homogeneous. It leads to bimodal, defects-filled microstructures, heterogeneous strains and complicated, varied misorientation gradients inside single grains. Moreover, the microstructural heterogeneity was additionally confirmed by broad distributions of grain size as well as a great deal of localized deformation regions, including dislocation tangle zones and in-grain strain contours.

Generally, during the HE processing, large deformation energy is stored within a deformed material, as indicated by continually growing values of both the KAM and GAM parameters with an increase in strain exerted on a sample. This is a distinctive feature of any SPD-treated specimen. The change in the aforementioned parameters as deformation proceeded is illustrated

in Fig. 4.17. Any sample characterized by a KAM/GAM value exceeding 0.5 should be viewed as deformed, thus one may conclude that HE-processed titanium is a highly deformed material.
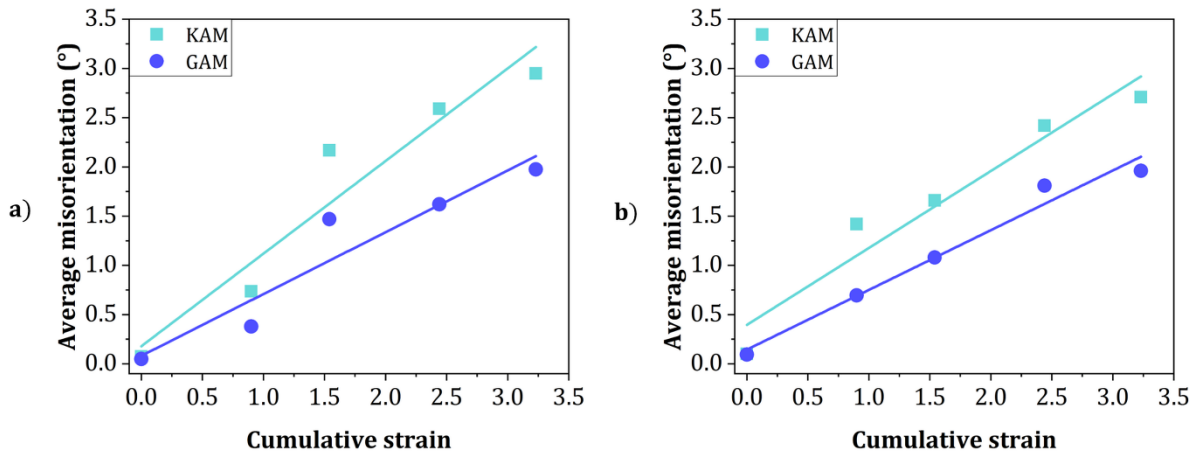
Fig. 4.17. Change in the KAM and GAM parameters with an increase in plastic strain for a) transverse, b) longitudinal cross-section of the analyzed materials.

During the first stages of HE, the deformation was clearly dominated by the formation of dislocation-type defects, including dislocation walls, dislocation tangles, assembling into zones, and LAGBs, as manifested by a series of collected TEM/BF images and GB fraction, depicted in Fig. 4.18. The latter data deserves a closer inspection since it is believed that boundaries affect a bunch of extraordinary properties a material exhibit. As soon as HE was introduced, a vast of LAGBs was generated in the volume of a deformed sample and, with a consecutive increase in plastic strain, their share steadily, yet slowly, decreased. It is believed that a typical SPD-treated material is characterized by a prevalence of HAGBs in its microstructure. However, for the hydrostatically extruded titanium such a condition has not been reached. The amount of LAGBs was greater than that of HAGBs with the exception of a material deformed at the strain of 3.23. Strictly speaking, its TCS and LCS were filled with 0.51 and 0.24 of HAGBs, respectively. It could be assumed that any additional processing might substantially augment the fraction of HAGBs, knowing that post-deformation heat treatment did not change the share of boundaries within a microstructure.
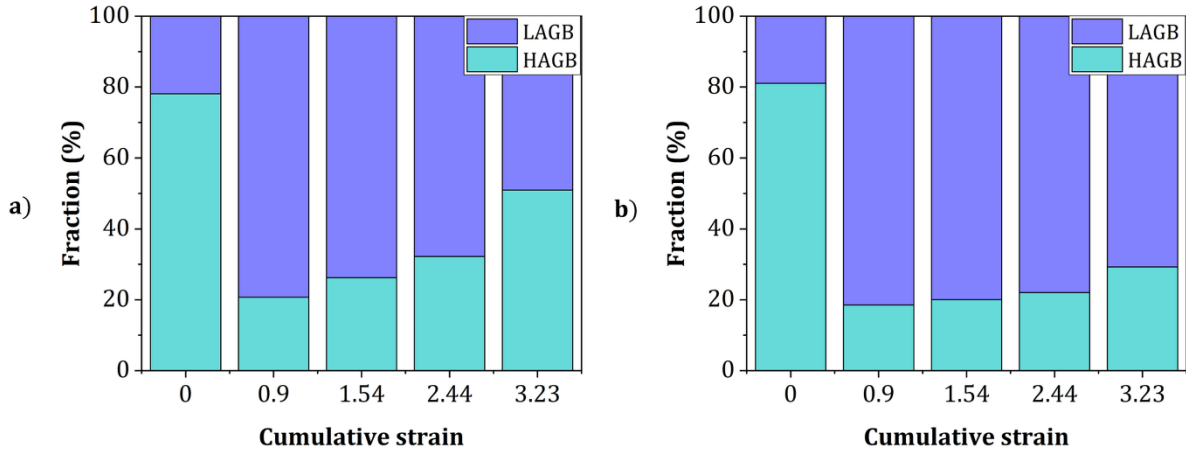
Fig. 4.18. Change in the fraction of HAGBs and LAGBs with an increase in plastic strain for a) transverse, b) longitudinal cross-section of the analyzed materials.

In general, a gigantic amount of GBs is present in the volume of the HE-processed titanium. They differ considerably in terms of length, shape and origin. While the majority of them are wavy and fragmented, some are also straight and well-lineated. What is especially interesting is the remnants of disconnected, poorly-lineated LAGBs that have been trapped inside large, coarse grains. They could be viewed for those materials that were deformed at lower strains i.e., less than 1.54, and represent the most common exemplification of the grain subdivision phenomenon. Actually, this mechanism could take place easily, even at ambient temperatures, as a simple result of mechanical deformation, whereas thermal contributions are prerequisite for any dynamic recrystallization (DRX) processes [92]. Overall, the complexity of HE as well as local increases in both stresses and temperatures activate multiple gliding, which results in the formation of irregularly-shaped, disconnected LAGBs. At the same time, due to the abovementioned factors, misorientation of grain boundaries tends to increase as grains of smaller size begin to form [93].

The extent of either dislocation gliding or mechanical twinning in titanium is believed to depend on several factors such as the purity of a grade, the deformation rate, the processing temperature and the presence of crystallographic texture [93]. Of course, the stress needed to activate twinning during deformation increases rapidly as grain size decreases, whereas gliding occurs even at low strains. In actual fact, twinning is suppressed when grain size hits the critical level [94]. In the case of the HE-processed titanium, only a couple of twins/twin boundaries were detected while performing TEM examinations, but their existence might be also supported by local extrema around 86° on the misorientation angle plots, indicating the presence of $\{10\bar{1}2\}$

twins. At the subgrain level, twins were not observed for materials deformed at strains exceeding 2.04, although it should be borne in mind that some lengthened, small-sized grains surrounded by well-lineated, straight GBs might have been produced by twinning.

In addition to abundance and heterogeneity of GBs, grains themselves are also broadly-based in the microstructure of the hydrostatically extruded titanium. One may have easily detected those containing either subgrains, dislocation cells or single dislocations. Furthermore, nearly or completely defects-free grains can also be distinguished. They evolved from dislocation cells or cell blocks upon absorption of dislocations by adjacent grain boundaries [62]. The grains of elongated morphology were prevailing on the LCSs and, irrespective of the applied plastic strain, they were composed of a substantial substructure, bordered mainly by LAGBs. On the other hand, a growing fraction of equiaxed grains with consecutive extrusion operations is of special significance, especially on the TCSs. It is commonly known that such grains originate from DRX-based processes, operating effortlessly during deformation/straining. Nevertheless, it cannot be excluded that they might have been created by the fragmentation of lengthened grains as these were detected on both of the orthogonal CSs. The presence of elongated clusters is notably surprising on the TCSs and it substantiates the process of grain subdivision. With respect to grain size, although it is seen that grain size distributions were narrowed as HE proceeded, large, coarse-grained fraction prevailed during every single stage of processing. What is more, the log-normal plots, being characteristic of SPD-treated materials, have never been acquired. A special attention should also be devoted to grain morphology, particularly size and shape. EBSD and TEM data enabled large, medium-sized, fine, ultrafine or even nanocrystalline grains to be visualized. With respect to the LCSs, grains were mostly elongated in shape, but on the TCSs, highly-irregular, wavy as well as lengthened grains could have been observed. Such a heterogeneity of grain size and shape indicates that grain subdivision process might have occurred.

One of the typical features in the SPD microstructures is the abundance of deformation-induced defects e.g., dislocations, specifically in the proximity of grain boundaries [62]. Hydrostatically extruded titanium is not an exception to this principle. Regardless of the strain applied, dislocation density was always higher next to grain boundaries than in the interior of grains. The observation is fully supported by the grain boundary maps as well as TEM/BF images. In general, the HE-processed titanium is characterized by highly diversified dislocation density, encompassing LAGBs, various dislocations present inside grains/subgrains, any boundaries enclosing dislocation cells as well as subgrains themselves. Overall, dislocation density in the

hydrostatically extruded titanium varies considerably when examining different microstructure areas. Individual dislocation cells, dislocation tangles and dense clusters of dislocations may be seen. The distribution of dislocations was particularly diverse within large grains. It is worth noting that dislocations were generated during every single step of deformation, proving the slip to be a dominant deformation mechanism during HE of pure titanium. The fact that a variety of dislocation-derived structures were generated already during the first stage of HE proves that small (i.e., $\varepsilon < 1$), limited strains are required for dislocation-type defects to be accommodated in a processing material. As the applied strain had been increased, the density of deformation-induced defects was growing progressively, yet the formation of LAGBs, dislocation walls and dislocation cells dictated the microstructure evolution at low and intermediate strains. Generally, a slow drop in the mean grain size estimated on the LCSs as well as the abundance of dislocation tangle zones, cell blocks or triple points prove dislocation-type defects to dominate in the microstructure of hydrostatically extruded titanium. In crude terms, dislocation walls initiated the microstructure rebuilding and, with an increase in HE steps, they got assembled into single dislocation cells. As cumulative plastic strain had continuously increased, these evolved into subgrains or cell blocks, bordered mainly by branched, poorly-delineated LAGBs. Finally, the latter turned into clearly visible HAGBs, while subgrains were transformed into small-sized, nearly-equiaxed grains. What is also worth mentioning is that the rapidly increasing density of dislocation-type structures as well as the substructure development are stimulated by dislocation gliding [93]. However, while taking intermediate or high strains into account, it was noticed that defects' capacity had already been reached. It is believed that after hitting the saturation limit, dislocation-based defects tend to annihilate and/or disappear into sinks i.e., abundant sites in a material containing ultrafine grains/subgrains as well as cell-type features [62]. Interestingly, the co-existence of dislocation cells and tangles of dislocations had been ceased as the former were created by the recovery-dominated rearrangement of dislocations. In fact, one of a possible source of dislocation cells are dislocation tangles since they freely interact with one another, rearrange or annihilate. Consequently, such events result in a reduction of dislocation density. In terms of the HE-treated titanium, this claim could be backed up by the changes in the GOS values with an increasing plastic strain, as shown in Fig. 4.19. The parameter reached its maximum for a material deformed at the strain of 1.54, though the deformation process was continued until the cumulative strain of 3.23. It is well-known that even a slight decline in the volume of the GOS parameter implies the occurrence of recovery and/or recrystallization processes [93]. In addition, huge misorientation gradients within grains and the constantly growing share of small-sized grains, exhibiting more regular morphology

(i.e., close-to-equiaxed or simply equiaxed), are also an indicative of thermally driven mechanisms. Therefore, it may be expected that any additional deformation would force the formation of clearly equiaxed grains as coarse, elongated ones would evolve into narrow bands surrounded by lineated, well-developed HAGBs.
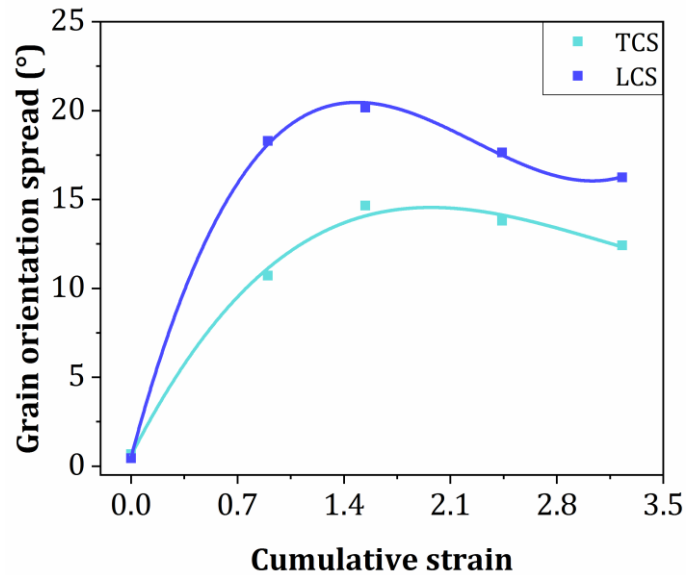
Figure 4.19. Changes in the GOS parameter with an increase in plastic strain during the HE processing

Generally, due to the fact that titanium is characterized by high stacking fault energy (i.e., around 300 mJ/m^2), instead of conventional discontinuous dynamic recrystallization (CDDRX), continuous dynamic recrystallization (CDRX) is assumed to be activated during its deformation. The fundamental premise of DRX, either discontinuous or continuous, is the development of strain/defects-free grains that are surrounded mostly by HAGBs. The process is driven by the stored deformation energy [92]. CDRX is viewed as a recovery-dominated process, operating by a gradual evolution of LAGBs into HAGBs [95]. The presence of dislocation-type defects nearby grain boundaries facilitates CDRX. In fact, continuous absorption of dislocations takes place as LAGBs turn into delineated, sharp HAGBs. At the same time, misorientation between cells/subgrains increases and, eventually, fine, ultrafine or even nano-sized grains are formed [96]. In general, it is pileup which is responsible for high-density dislocations being present close to grain boundaries since, in order to accommodate plastic deformation, a vast amount of defects next to grain boundaries is required [95]. All of such phenomena were observed while inspecting the alterations in microstructure of pure

titanium caused by the multistage HE process. In addition, CDRX is also identified by complex, long-range misorientation gradients within single grains since these provide the imminent driving force, enabling HAGBs to be formed. What also ought to be highlighted is that in the HE-treated titanium specimens dislocations remained in deformed grains, even if heat treatment had been introduced. It clearly proves that CDRX is to operate during the later stages of HE. If CDDRX was to happen, the majority of deformation-induced defects would be annealed out [95]. Annealing of the HE-processed titanium samples in 200°C seemed to have little influence on the microstructure, yet stress relieving should be noted as the most important change. Obviously, the results could have been expected as subjecting the ECAP-deformed titanium to annealing at 300°C, 400°C or 500°C also had meaningless impact on the resultant microstructures [97].

It needs to be concluded that the primary grain fragmentation mechanism occurring at lower strains is the development of subgrains and LAGBs in a process called grain subdivision. On the other hand, at higher strains, CDRX tends to dominate. Similar findings were reported for pure titanium subjected to various modifications of the ECAP process, i.e., continuous or incremental [98].
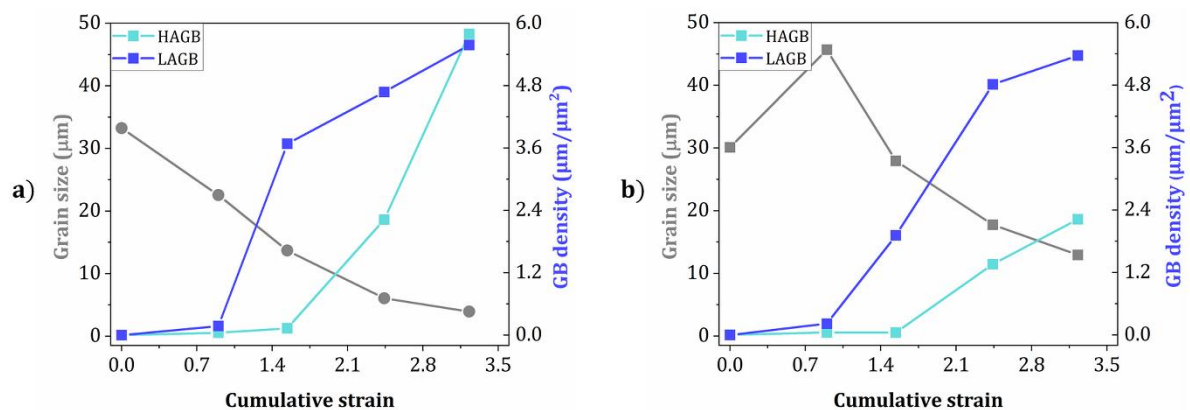
Figure 4.20. Changes in HAGB and LAGB density with the corresponding variations in grain size on the a) TCSs, b) LCSs of hydrostatically extruded titanium

The ultimate proof of these claims may be provided when analyzing variations in grain boundaries density, depicted in Fig. 4.20. Regardless of the examined CS, one may distinguish two characteristic stages in the grain boundary density plots. The first one, occurring below the strain of 1.54, is characterized by a development of substructure, expressed as a rapid increase

in the LAGB density. In addition, during the first stage, either a substantial drop (in the case of TCSs) or an increase and then a decline (for the LCSs) in the mean grain size took place. Even though the grain size for the TCSs decreased significantly, coarse and slightly downsized fraction of grains still prevailed in the volume of a material. In terms of the LCSs, until the strain of 1.54, the overall change in the mean grain size was barely noticed, yet grains morphology was altered considerably. The presence of some original/parent grains is of special importance as these only confirm that the grain subdivision process happened. The second stage of the grain boundary density curves features a massive surge in the HAGB density and a continuous reduction in the value of the mean grain size, the phenomena typical of CDRX.

4.2. Crystallographic texture

The evolution of titanium's crystallographic orientation of grains during hydrostatic extrusion, was determined from EBSD orientation maps, and is depicted in Fig. 4.21 and Fig. 4.22 for TCS and LCS, respectively. (0002) and $(10\bar{1}0)$ pole figures are shown and, in addition, the IPFs are also presented in order for an unambiguous determination of the preferred orientations to be possible. In general, the analysis of crystallographic texture confirmed the nature of the investigated material to be highly anisotropic. The texture of the as-received titanium was relatively weak since a single one predominant component was not revealed while inspecting the (0001) and $(10\bar{1}0)$ pole figures. However, the ED IPF for the TCS (Fig. 4.21 a) confirmed that orientations of some grain clusters fall towards the center of this IPF. Obviously, upon plastic deformation realized by means of HE, the initial texture was significantly altered as the formation of preferred orientations took place. Hydrostatically extruded titanium exhibits a strong fiber texture, typical for extruded as well as drawn and swaged metals having the hcp crystal structure. Interestingly, the fiber component had already formed during the first stage of HE, yet consecutive extrusion operations strengthened it as the final material demonstrates axial texture.

The examination of the PFs determined on TCS (Fig. 4.21) enables to confirm that grains are aligned such that $<10\bar{1}0>$ directions are parallel to the ED (or equivalently, $\{10\bar{1}0\}$ planes are perpendicular to ED). On the other hand, the PFs determined on TCS and LCS (Figs. 4.21 and 4.22) show that grains are oriented such that $<0001>$ directions, forming a radial distribution, are perpendicular to ED, which confirms the fiber character of texture. This also means that $\{0001\}$ planes are parallel to ED. Finally, inspecting IPFs from Fig. 4.21, it can be summarized that the texture of the final material is comprised between two fiber components with respect to the ED: the main component $< 10\bar{1}0 >$ and the weaker one: $< 11\bar{2}0 >$.

Generally, the evolution of texture in titanium processed by various SPD processes could also be correctly modelled; an example comprehensive study using the visco-plastic deformation model is presented in [99]. In particular, it can be noted that a successful prediction of the HE texture of titanium was obtained using a crystallographic elasto-plastic deformation model [100], [101] in which slip and twinning systems characteristic for titanium were taken into account. The basic equation of the model as well as the comparison of predicted and experimental pole figures are presented in the Appendix.
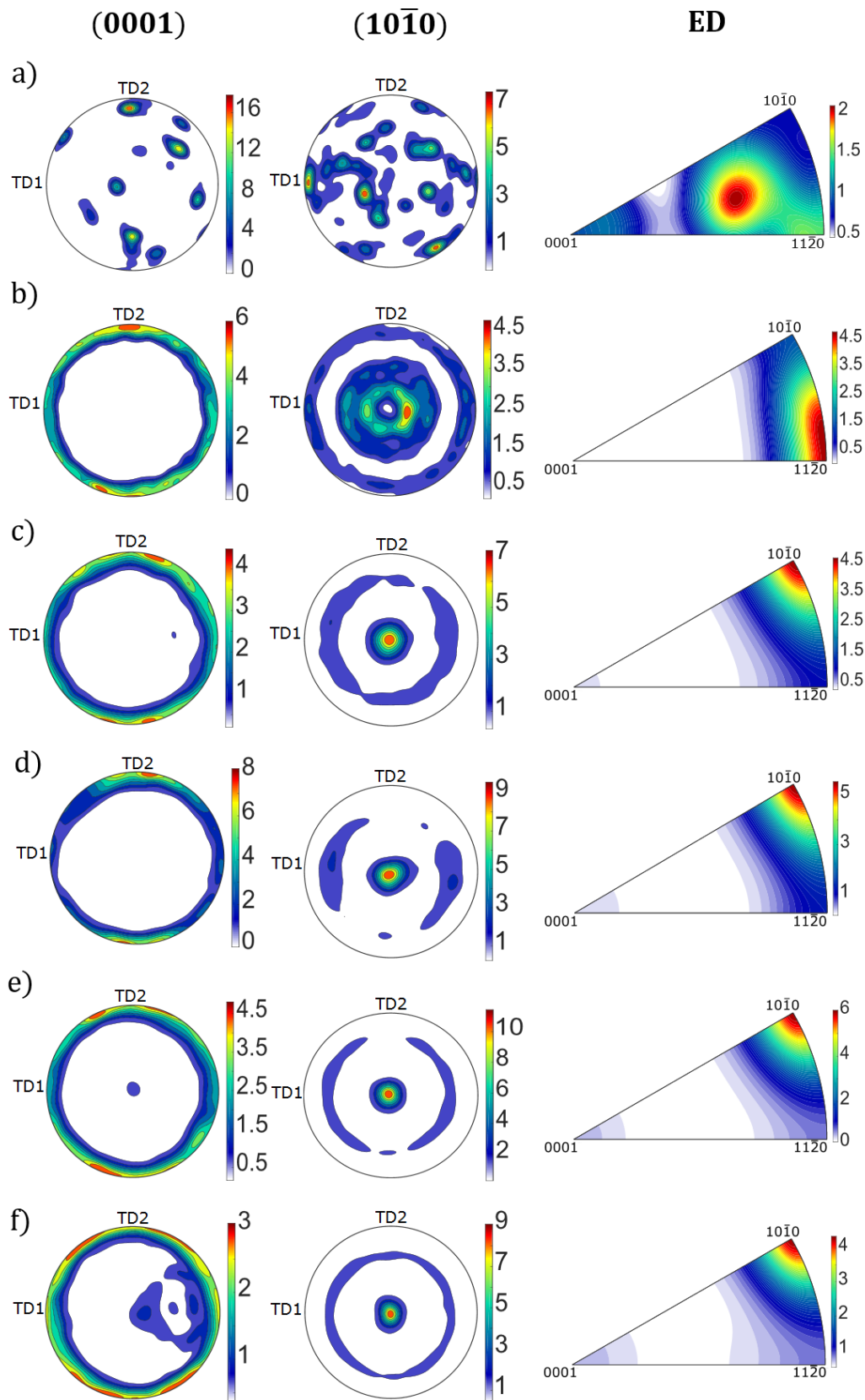
Fig. 4.21. (0001) and (10$\bar{1}$0) PFs as well as IPFs of ED collected from the transverse cross-sections of the a) as-received material, b) initial material, c) titanium deformed at ε = 0.9, d) ε = 1.54, e) ε = 2.44, f) ε = 3.23.
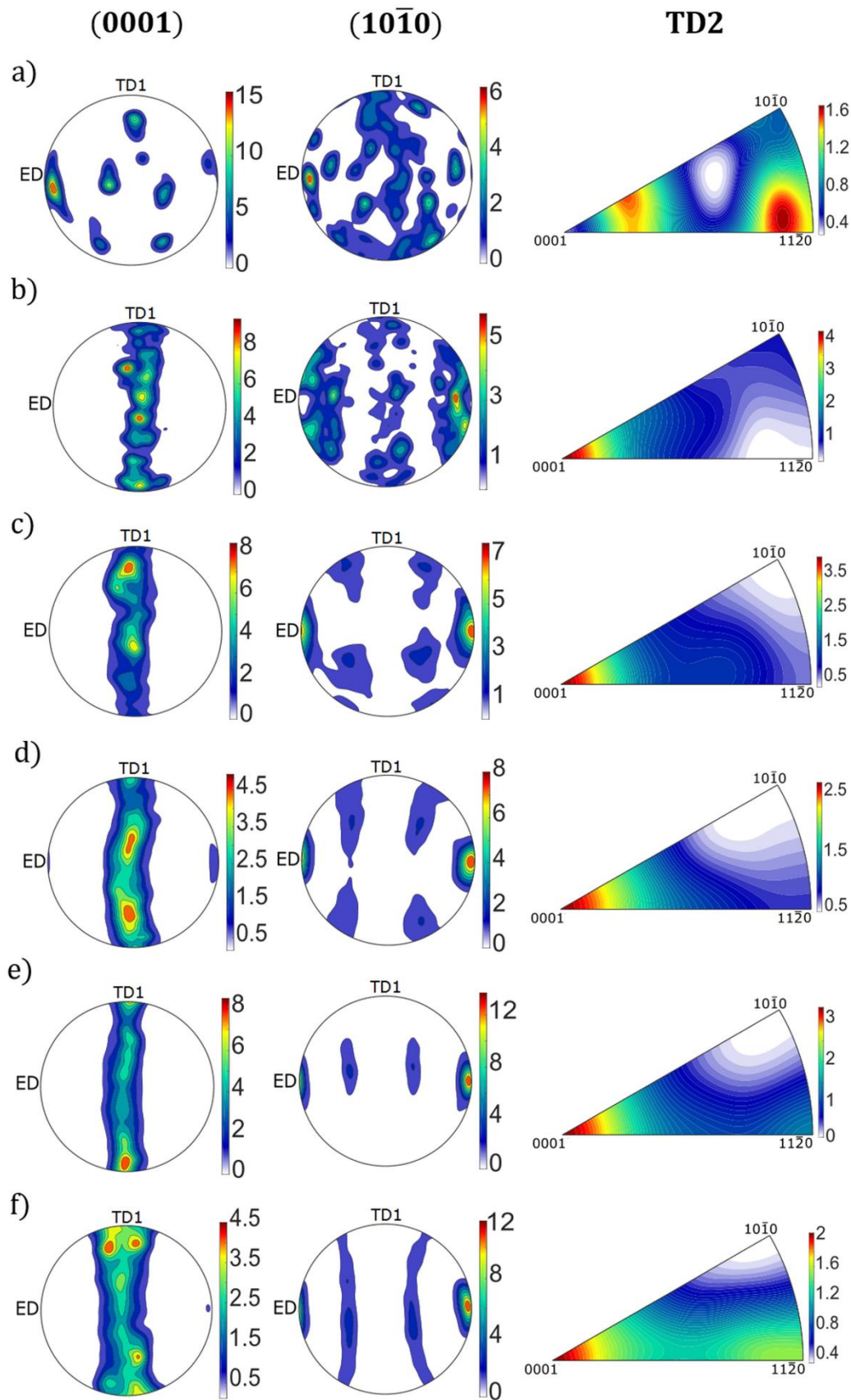
Fig. 4.22. (0001) and (10$\bar{1}$0) PFs as well as IPFs of TD2 collected from the longitudinal cross-sections of the a) as-received material, b) initial material, c) titanium deformed at ε = 0.9, d) ε = 1.54, e) ε = 2.44, f) ε = 3.23.

4.3. Mechanical behavior

4.3.1. Static mechanical properties

The most representative engineering stress-strain curves plotted for the HE-processed samples are illustrated in Fig. 4.23a. It may be seen that after reaching the ultimate tensile strength (UTS), the initial material underwent gradual flow softening, resulting in the elongation to failure of nearly 25%, typical for unprocessed, coarse-grained titanium. On the other hand, all of the HE-fabricated specimens exhibited flow softening quickly without demonstrating the apparent strain hardening mechanism. In general, severely deformed titanium samples are characterized by low ductility (less than 10%), manifested during the experimental testing by plastic instability in the form of early necking or shear bands. Interestingly, elongation at break did not diminish considerably with a subsequent increase in cumulative plastic strain as it persisted in the order of 7-8%.
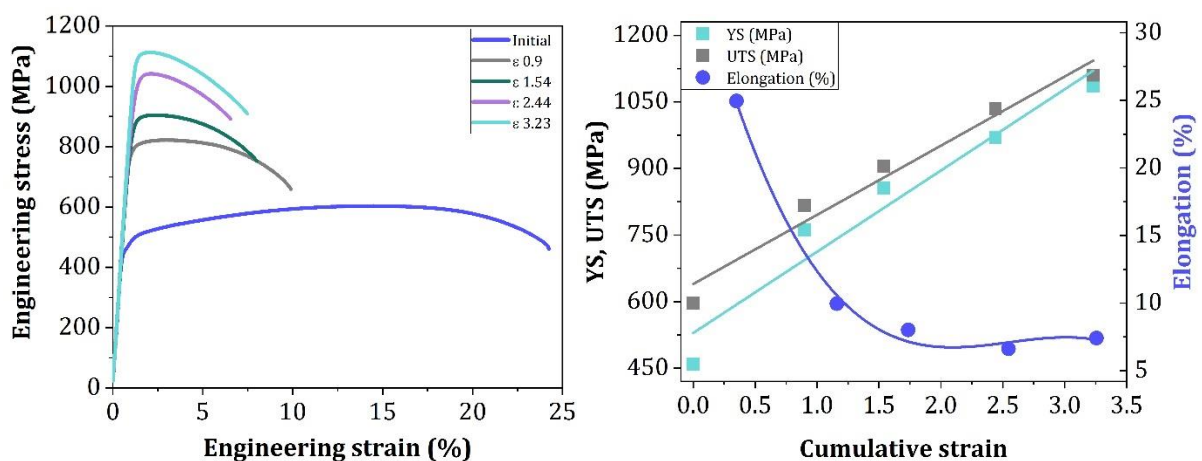
Fig. 4.23. a) typical stress-strain curves plotted for the whole deformation range, b) change in YS, UTS and elongation with an increase in plastic strain.

The evolution of mechanical properties during HE is presented in Fig. 4.23b. As expected, yield stress (YS) and UTS rose continuously when additional extrusions were introduced. For the final sample, both of these parameters were more than two times greater than those of the material in its initial condition. Additionally, as plastic strain increased, the difference between UTS and YS became markedly smaller e.g., 150 MPa for the initial specimens vs. 25 MPa for the final ones. It has to be stressed out that an exceptional value of UTS i.e., 1110 MPa, was achieved for the final material, confirming the multi-stage HE technique to be one of the most

efficient method in reinforcing the strength of pure titanium without any supplementary operations. However, for plastically deformed materials, the tendency of strength and ductility to be mutually exclusive properties is a common phenomenon. The strength-ductility paradox was confirmed to occur in hydrostatically extruded titanium as the final HE-processed samples encountered a three-fold decrease in ductility with comparison to the initial material. Such a behavior originates from the fact that the sites for continuous dislocation gliding as dislocation accumulation is no longer possible when grain size is drastically reduced [102].
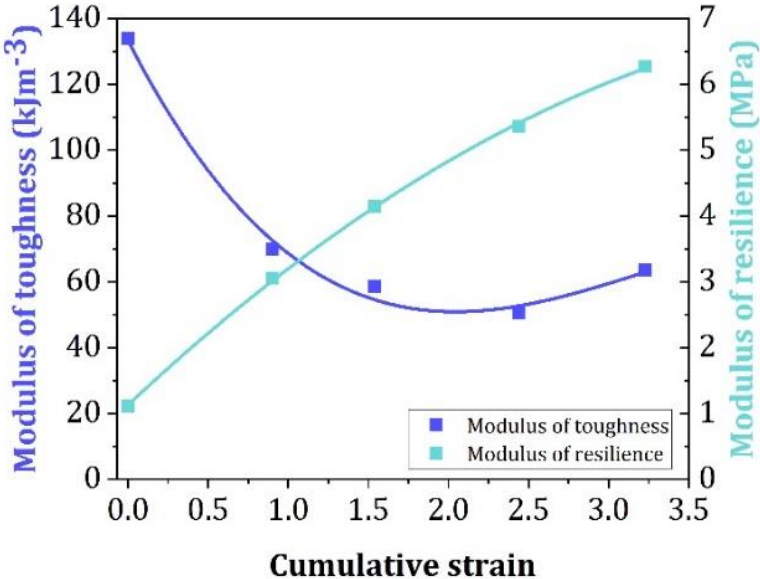
Fig. 4.24. Changes in modulus of toughness and modulus of resilience with an increase in plastic strain during HE.

The changes in modulus of toughness and modulus of resilience with an increase in cumulative strain are shown in Fig. 4.24. The former decreased notably as the actual HE was introduced, what implies a reduced propensity of a material to withstand dynamic loading. Surprisingly, the final material exhibited a slight raise in the modulus of toughness, indicating that it might be possible to regain the plastic stability after reaching a certain level of straining. On the contrary, modulus of resilience grew steadily with the plastic strain increasing and for the final HE-processed titanium it was six times greater than for the initial material. It confirms that, in comparison to unprocessed samples, hydrostatically extruded specimens are able to absorb significantly greater amount of energy without suffering any form of damage.
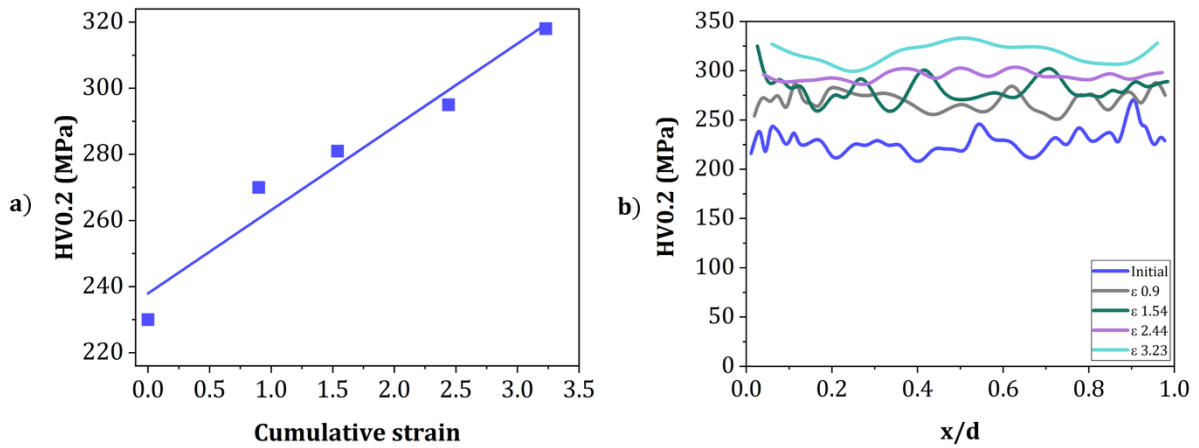
Fig. 4.25. a) change in Vickers hardness with an increase in plastic strain during HE, b) measurements of hardness distribution over diameter for the analyzed specimens.

The change in Vickers hardness with an increase in cumulative plastic strain is depicted in Fig. 4.25a. The obtained results showed that the consecutive extrusions caused hardness to slowly, almost linearly, rise and that the final material was approximately 40% harder than that in the initial state. Although the increase in hardness was not that spectacular as in the case of YS or UTS, what is worth highlighting is how hardness is distributed over a diameter of a sample (Fig 4.25b). It may be seen that the HE process provoked hardness to be more homogeneous. To better visualize the occurring changes, hardness distribution was illustrated in a form of radar plots, displayed in Fig. 4.26. Generally, the more blurred the graph, the more consistent the hardness. Even though there were a few violent fluctuations seen for an HE-processed sample, the general tendency of a material to become more uniform in terms of hardness after having been plastically deformed could be, without a doubt, noticed.
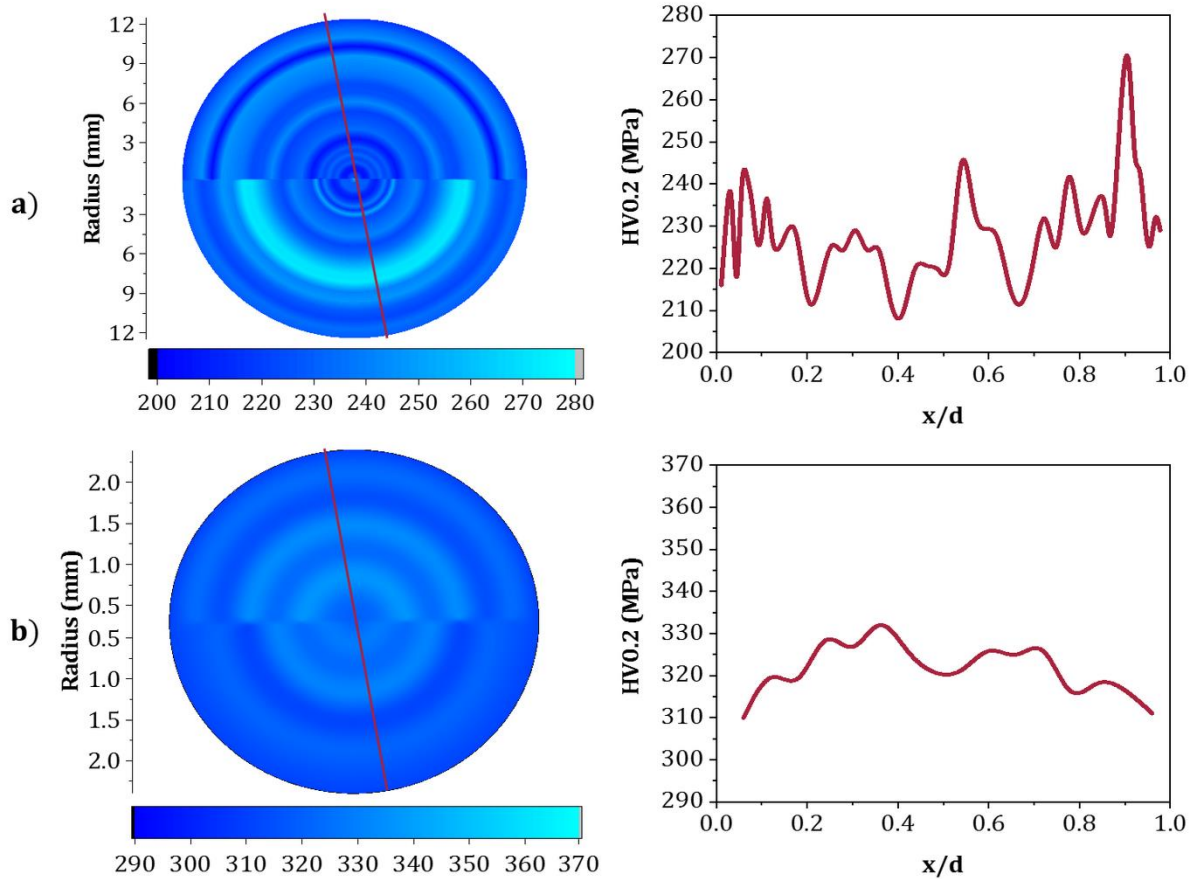
Fig. 4.26. Radar plots and the corresponding distribution of hardness over a diameter (claret-colored line) plotted for the a) initial material, b) material deformed at $\varepsilon = 3.23$.

In addition to tensile properties, representing the most typical way of revealing how a material behaves under a mechanical stimulus, compressive strength was also investigated. However, due to the fact that the maximum capacity of the testing machine had been reached and the materials were not destroyed, only YS in compression is discussed. The change in YS with an increase in plastic strain is illustrated in Fig. 4.27. For comparison, YS in tension was also added.
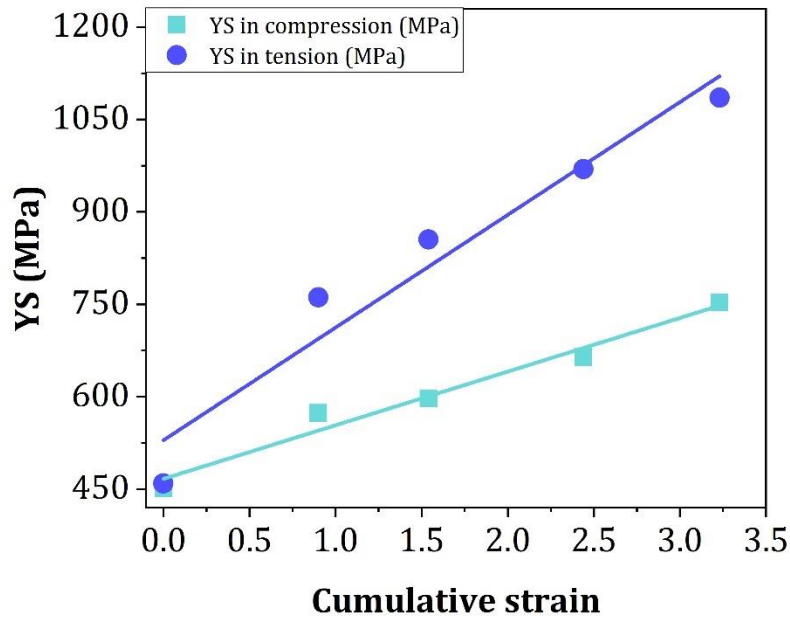
Fig. 4.27. Change in YS during HE

Tension-compression asymmetry, frequently reported for titanium-based materials, could be clearly seen. Interestingly, as deformation progressed, the difference between YS in tension and that in compression became greater e.g., 188 MPa and 305 MPa for the samples obtained at the strain of 0.9 and 2.44, respectively. Nonetheless, a noteworthy value of YS in compression i.e., 753 MPa, was achieved for the final material.

4.3.2. Fatigue mechanical properties

Lastly, fatigue properties of the HE-treated titanium, deformed at the strain of 3.23, were evaluated in order to inspect on the usefulness of a material from the point of view of load-bearing biomedical applications. A Wöhler diagram, also known as the S-N curve, plotting the applied stress against the number of cycles to failure is displayed in Fig. 4.28. In addition, two S-N curves of the ECAP-produced titanium are also included for comparison [103], [104].
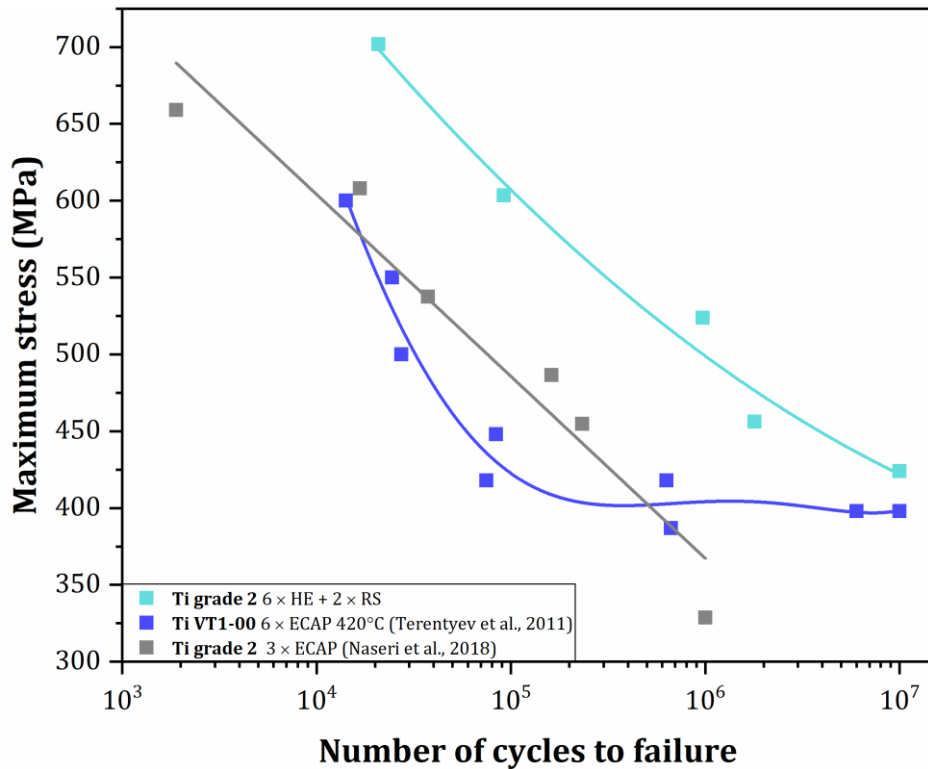
Fig. 4.28. Wöhler diagrams plotted for the hydrostatically extruded titanium as well as the ECAP-produced titanium.

It may be seen that either of the SPD-treated titanium is able to endure more than a million of loading cycles what makes it a fatigue resistant material. At the same time, in comparison to the ECAP-processed titanium, that obtained by means of HE is characterized by superior resistance to stress-govern fatigue. In fact, after reaching ten million cycles, the loading has been paused as the material did not fracture. Overall, in terms of its fatigue mechanical properties, hydrostatically extruded titanium has proven to be an attractive candidate for high-load bearing applications.

4.3.3. Microstructure-strength relationship

Originally, it was thought that superior mechanical properties of the SPD-treated materials are solely derived from grain refinement. Nevertheless, it is now well-known that superposition of various strengthening mechanisms occurs while a sample is subjected to any deformation procedure. In general, mechanical behavior of a severely deformed material is dependent on a variety of factors, including mean grain size, grain refinement ratio, versatility of GBs, texture development, substructure existence and the presence of internal elastic stresses. As proven, in pure titanium, all of these parameters were significantly altered by employing the multistage

71

HE, therefore they all contribute to its reinforced mechanical properties. It is reasonable to state that to explicitly point a single source of strength in hydrostatically extruded titanium seems impossible. However, when it comes down to its low ductility, it should be attributed to extremely high density of dislocations and a substantial share of LAGBs, acting as effective barriers for dislocation glide [98]. Normally, while being deformed, a pure metal is strengthened at the expense of its ductility (the so-called strength-ductility paradox). Contrarily, it has been found out that once a metallic sample gets deformed beyond a certain level of plastic strain, its plasticity could be slightly raised when additional straining is to be introduced [62]. The reason behind such phenomenon could be slightly increased boundary migration as well as, naturally, the reduced density of dislocations, whose saturation enables equiaxed, small grains to be formed.

As mentioned, superior strength of any SPD-treated sample stems from different strengthening mechanisms. Owing to their additive nature and by assuming that they function independently, the overall contributions of strengthening mechanisms into yield strength of a material can be expressed as follows:

$$\sigma = \sigma_0 + \sigma_S + \sigma_G \qquad (7)$$

where: σ_0, σ_S and σ_G denote the threshold stress (solid-solution strengthening), substructure strengthening and grain boundary strengthening, respectively. Nonetheless, it needs to be stressed out that both nanotwins and segregations could also have an impact on mechanical properties, though their input is generally omitted in the calculations of microstructure-strength relationships.

4.3.3.1. Solid-solution strengthening

The threshold stress is typically assessed as the sum of the friction stress, known as Peierls-Nabarro stress (σ_{P-N}), and the increment of strength stemming from solid-solution strengthening (σ_{S-S}):

$$\sigma_0 = \sigma_{P-N} + \sigma_{S-S} \qquad (8)$$

Since the former is known to be negligibly low (approximately 0.5 MPa), the threshold stress is governed only by the solid-solution strengthening. In terms of commercially pure titanium, the phenomenon is controlled by the total of impurities/interstitial solutes i.e., nitrogen, oxygen and carbon:

$$\sigma_0 \approx \sigma_{S-S} = 0.02G\sqrt{c} \qquad (9)$$

Where G stands for the shear modulus (40 GPa for pure titanium, grade 2), while c is the oxygen equivalent, converted from the contents of oxygen, nitrogen and carbon:

$$c = O + 2N + 0.75C \qquad (10)$$

The value of the oxygen equivalent for the HE-processed titanium is equal to 0.18, thus, within the present study, the threshold stress, or simply solid-solution strengthening contribution was estimated to be 339 MPa.

4.3.3.2. Substructure strengthening

The substructure strengthening in pure titanium is the resultant of the presence of both dislocations and LAGBs, encompassed within coarse, HAGB-enclosed grains. It is commonly evaluated based on the following formula:

$$\sigma_S = \sigma_D + \sigma_L \qquad (11)$$

Where σ_D describe the strengthening contributions due to free, mobile dislocations, while σ_L is the strengthening owing to LAGBs.

In order to characterize the dislocation strengthening, the original Taylor formula is employed:

$$\sigma_D = M\alpha Gb\sqrt{\rho} \qquad (12)$$

Where M, α, b and ρ represent the Taylor factor, a constant (ranging in value from 0.1 to 0.5), the Burgers vector and dislocation density, respectively. So as to calculate the dislocation strengthening, a variety of assumptions has to be made. Within the present thesis, M was taken as 2.5, which is consonant with the literature data stating slip to be prism-dominated. In addition, as the already published reports suggest, α should be assessed as 0.15, whereas b as 0.295 nm, which indicates the main impact of <a>-type dislocations during plastic deformation. In terms of dislocation density, the data was assumed to be $\sim 10^{15}$ m^2, the value typically obtained in XRD-based dislocation density calculations for the SPD-treated specimens. Therefore, in the HE-processed titanium, the strengthening due to dislocations was 140 MPa.

The contribution of LAGB strengthening in yield strength of a material is usually expressed as follows:

$$\sigma_L = M\alpha G \sqrt{\frac{3b\theta_L(1-f)}{d}} \qquad (13)$$

Where θ_L is the mean misorientation angle of LAGBs (expressed in radians), f stands for HAGB fraction and d denotes the mean subgrain size. While performing any calculations of the LAGB strengthening, EBSD and TEM data prove themselves necessary. However, since EBSD facilities are not able to detect misorientations below 2°, the overall LAGB strengthening is usually overestimated. Regardless of the data accuracy, the mean misorientation of LAGBs was taken as 8° (0.14 in radians), the HAGB fraction was calculated as 0.51, whereas the mean subgrain size was evaluated as 130 nm. Thus, the LAGB strengthening was 324 MPa.

4.3.3.3. Grain boundary strengthening

Typically, the strength increment resulting from GBs is described by using the standard Hall-Petch (HP) law, whereas in the case of the SPD-processed materials, due to their complex, bimodal microstructures, a summation of coarse grains' contribution (σ_{CG}) as well as ultrafine grains' contribution (σ_{UFG}) is more legitimate:

$$\sigma_G = \sigma_{CG} + \sigma_{UFG} = k_{HP}\left(\frac{1-f_{UFG}}{\sqrt{d_{CG}}} + \frac{f_{UFG}}{\sqrt{d_{UFG}}}\right) \qquad (14)$$

Where k_{HP} denotes the Hall-Petch constant (taken as 0.3 MPa $\times$ m$^{0.5}$), f_{UFG} is the fraction of ultrafine grains in the microstructure (0.316, based on the EBSD data available), while d_{CG} and d_{UFG} stand for the mean thickness of coarse-grained and ultrafine-grained fraction of grains, respectively. The former was assessed as 4 μm, whereas the latter as 0.5 μm. Combining all the data, the estimated grain boundary strengthening was calculated to be 237 MPa.

4.3.3.4. Total strengthening

Based on the abovementioned calculations, the contributions of all the considered strengthening mechanisms in the YS of the HE-processed titanium are listed in Table 4.6.

Table 4.7. Calculated estimates of the strengthening mechanisms.

Threshold stress (MPa)	Substructure strengthening (MPa)		Grain boundary (HAGB) strengthening (MPa)	Predicted YS (MPa)	Measured YS (MPa)
	Dislocation strengthening [MPa]	LAGBs strengthening [MPa]			
339	140	324	237	1040	1085

The predicted value of the YS is barely 4.2% smaller than that of the measured one, despite a great deal of assumptions and uncertainty in assessing some of the parameters, including density of dislocations. It needs to be concluded that substructure strengthening i.e., due to dislocations and LAGBs, had the greatest influence on mechanical properties of the HE-processed titanium. Interestingly, strengthening due to HAGBs is notably lower than that of the LAGBs. The claim is, however, completely supported by the grain boundary fraction plot and the grain boundary density curves as well as a series of TEM/BF images collected. The retention of original/undeformed or only slightly deformed coarse grains in the microstructure could also back up the very high value of the LAGB strengthening. On the contrary, a clearly diminished efficiency of the HAGB strengthening may be substantiated by distinct crystallographic orientation of grains and twinning suppression during the later stages of the HE processing. What is also worth highlighting is that there might be some additional strengthening phenomena occurring during HE, such as those engaging the already mentioned nanotwins or segregations as well as the Basinski effect.

4.4. Surface character

4.4.1. Roughness and surface defects

With respect to the SPD-treated materials, owing to very high density of surface defects, it is highly recommended to perform any roughness-related measurements by taking small areas of a sample, e.g., 1 μm × 1 μm or 5 μm × 5 μm, into account [105]. However, what needs to be stated is that roughness of a material is mostly an adjustable feature, the one that may be easily altered by approaching any surface modification technique. Nowadays, majority of the industry-oriented materials are customized with respect to their topography/roughness so as properties of special importance are provided. The impact of surface roughness on biophysical properties a severely deformed specimen manifests cannot be left aside, yet it has been documented that it might not be a factor directly influencing cell-material interactions [24]. It needs to be mentioned, however, that surface roughness plays a determinant role in the osteointegration rate and the biomechanical fixation of a medical implant. As a matter of fact, higher nanoroughness as well as favorable surface chemical composition may promote superior adhesion, proliferation and differentiation of various cell cultures [84]. Within the present study, prior to AFM investigations, the examined substrates were carefully polished and etched afterwards with the use of an alcohol-based solution in order to obtain intentionally smooth, mirror-finished as well as nanorough surfaces. If untreated, simply as-cut substrates had been characterized, different results would be obtained.

The surface topographies of the materials deformed at the strain of 2.44 and 3.23 are illustrated in Fig. 4.29, whereas surface-related characteristics, including roughness, peak density, mean spacing and surface defects density, are listed in Table 4.8. It is seen that upon implementing the one-step etching, the analyzed surfaces were nanometrically rough and no significant differences in the average arithmetic mean roughness R_a between all of the inspected substrates were observed. Therefore, the effect of surface roughness on biophysical properties of the HE-treated titanium was eliminated. On the other side, there were statistically significant differences viewed between most of the other determined parameters. Discrepancies in surface topography were evident not only with regard to the shape of surface features, but also their amount. Coarse and ultrafine grains of elongated morphology were clearly visible on both LCSs, whereas the shape of grains present on TCSs was hardly discernable. Although the investigated area was considerably smaller in comparison to the regions from which the IPF maps were gathered, the results obtained with the use of the AFM technique are consistent with those coming from the EBSD method.

In general, a grain never represents a completely smooth structure as various grooves, pits or peaks, constituting the so-called surface texture or surface irregularities, always appear. Surface defects comprise either boundaries or planes, separating a material into zones of the same crystalline structure, yet different orientation [106]. They could be also regarded as the spots of substantial stress concentration that have been formed as a result of material's fabrication or post-processing [107]. On the macro-scale, surface defects include various cavities, patterns, areas of diversified geometric alignment as well as surface debris and particles that have been trapped onto it. In terms of the SPD-processed samples, the number of surface imperfections is thought to be especially high, therefore examining 5 μm × 5 μm areas is, once again, highly justified.
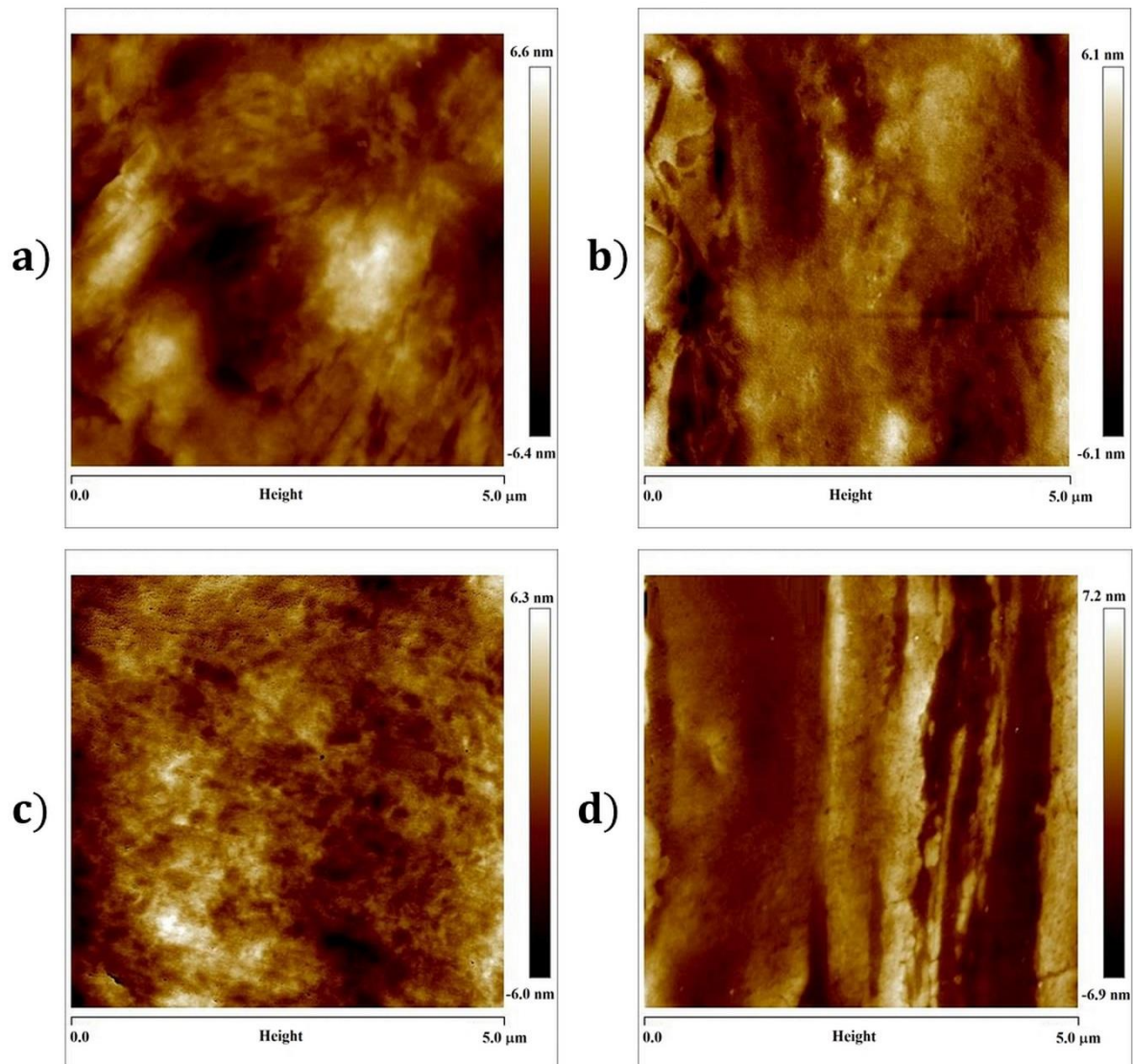
Figure 4.29. AFM topographies of the transverse and the longitudinal cross-section taken from the HE-processed titanium deformed at the strain of a, b) 2.44, c), d) 3.23

Within the present work, the transversal topography of the material deformed at the strain of 3.23 was the one exhibiting the most diversified surface texture as the parameter named surface defects density indicates. As expected, its value for the TCSs was always higher than that for the LCSs, regardless of the strain applied. For every 1 μm of the hydrostatically extruded titanium processed at the strain of 3.23, the number of surface irregularities falls in the range from 1.51 (the lower bound of y-Peak Density for the LCS) to 4.13 (the upper bound of x-Peak Density for the TCS), confirming the material to be defects-enriched and ultrafine-grained.

Table 4.8. AFM- and EBSD-derived surface characteristics of the HE-treated titanium deformed at two different strains.

		3.23 TCS	3.23 LCS	2.44 TCS	2.44 LCS
AFM-derived	Roughness (nm)	1.61 ± 0.16	1.77 ± 0.22	1.92 ± 0.53	1.67 ± 0.41
	x-Peak Density $(\frac{1}{\mu m})$	3.31 ± 0.82	2.29 ± 0.34	2.56 ± 0.46	1.89 ± 0.64
	y-Peak Density $(\frac{1}{\mu m})$	3.17 ± 0.70	2.12 ± 0.61	2.35 ± 0.49	1.48 ± 0.20
	x-Mean Spacing (μm)	0.32 ± 0.09	0.47 ± 0.07	0.40 ± 0.07	0.60 ± 0.23
	y-Mean Spacing (μm)	0.33 ± 0.08	0.50 ± 0.10	0.47 ± 0.10	0.69 ± 0.09
	Surface defects density $(\frac{1}{\mu m^2})$	10.49	4.87	6.00	2.80
EBSD-derived	HAGB density $(\frac{1}{\mu m})$	5.80	2.22	2.22	1.36
	LAGB density $(\frac{1}{\mu m})$	5.58	5.37	4.68	4.82

When examining both CSs taken from the same material, it was found out that the differences in the mean spacing and the peak density were, in most cases, statistically insignificant, proving that at the submicrocrystalline level, the HE-processed titanium is a relatively uniform material, though characterized by a variety of surface defects. It cannot be banished that the results were affected by the area examined. However, had greater regions been studied, the calculated values of surface characteristics would have been considerably underestimated. While comparing the corresponding CSs from the samples deformed at various strains, the differences between the analyzed parameters were also statistically insignificant ($p < 0.05$) except for the surface defects density parameter. As a general rule, low values of mean spacings are entangled with high values of peak densities, implicating surfaces filled with a lot of imperfections. The resemblance between the CSs is believed to originate from the areas taken into examination as the EBSD data confirmed the discrepancies in grain boundary density as well as grain size

between the specimens deformed at the strain of 2.44 and 3.23. What needs to be mentioned herein is that the AFM-derived defects encompass mainly grain boundaries and these, in contrary, greatly differ for the investigated CSs. Thus, while deliberating over surface irregularities the comparison with EBSD data seems reasonable.

Generally, the use of AFM data enabled to confirm that, in comparison to the LCSs, the TCSs of the HE-processed titanium were greatly refined and covered with a higher number of surface irregularities. While no significant differences in surface nanoroughness of the hydrostatically extruded titanium were recorded, the tested surfaces varied considerably in terms of their topography. If biophysical properties were to be stimulated mainly by the presence of surface defects, it should be expected for cells to adhere to any transversal surface of the hydrostatically extruded titanium more readily. In fact, it has been proven that, for ultrafine-grained materials, surface topography rather than roughness itself encourages higher protein adsorption and cell-material interactions [108]. What is more, some reports covering hierarchical modification of the surfaces by applying alkali treatments, acid etching or sandblasting have shown that cell colonization is strictly affected by surface topography/morphology. Additionally, cytocompatibility of a severely deformed material as well as the apatite-forming ability of its surface have also been enhanced as a consequence of changes in topography [84].

4.4.2. Wettability and surface energy

Hydrophilicity is, among electrostatic interactions, ionic binding and van der Waals interactions, one of the most important factors mediating adsorption of biomolecules onto surface. This, in turn, has a profound impact on cell-material interactions. It is believed that the importance of wettability (i.e., hydrophilicity and hydrophobicity) for biophysical properties of a material is supreme. According to previous reports, cells are likely to adhere to any surfaces of hydrophilic character more readily. Moreover, surfaces exhibiting moderate to high hydrophilicity facilitate the adsorption of mineral phases, necessary for guaranteeing a strong, biomechanical interlocking between an implant and a living tissue (chondro- or osteointegration) [85]. In general, wettability of a material can be controlled by altering surface roughness or functionalizing with chemical groups [109]. Wetting behavior of rough surfaces is enhanced in comparison to smooth ones owing to the increased surface area of a roughened material [69]. As a matter of fact, a suitable roughness can influence both early and late cell events a biomaterial's surface is to encounter [12]. Due to the fact that roughness of the hydrostatically extruded titanium is independent of the CSs studied, any discrepancies in its wettability would arise from different factors.

Contact angles of deionized water and two other solvents (polyethylene glycol and diiodomethane), measured for all of the characterized surfaces are depicted in Fig. 4.30.
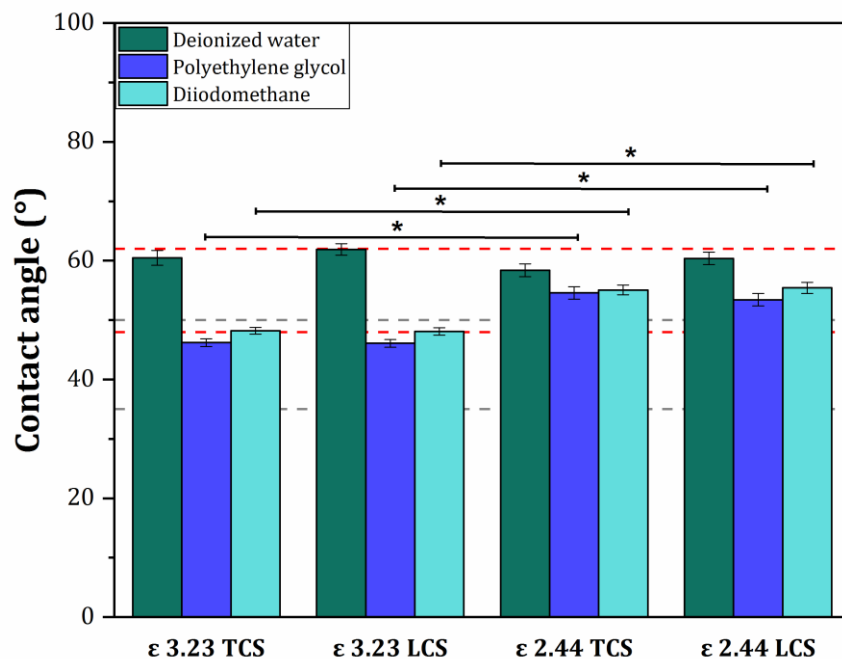
Figure 4.30. Wettability of the examined CSs. The asterisk * sign denotes statistical significance ($p < 0.05$) between the probes.

In terms of the aqueous contact angle, it can be seen that either of the substrates is moderately wettable in nature as red-colored lines, marked at 48° and 62°, indicate. At the same time, no statistically significant differences in water contact angle measured between the whole set of examined samples were noted. The results seem quite surprising as most of the reports looking at the biocompatibility of unconventionally processed titanium-based materials have highlighted the clear differences in aqueous contact angles between the characterized surfaces [69], [78], [85], [110]–[112]. However, within the present study, the materials chosen for physicochemical and biological investigations were characterized by bimodal microstructures, composed of large, fine and ultrafine grains, whereas the differences were illustrated for clearly coarse-grained, unprocessed specimens and those displaying completely ultrafine-grained microstructures. It has been declared that a clear correlation between enhanced wettability of a material and its decreased grain size exists [82]. In addition, if only aqueous contact angles are to be examined, erroneous findings on the material's wettability might be reported.
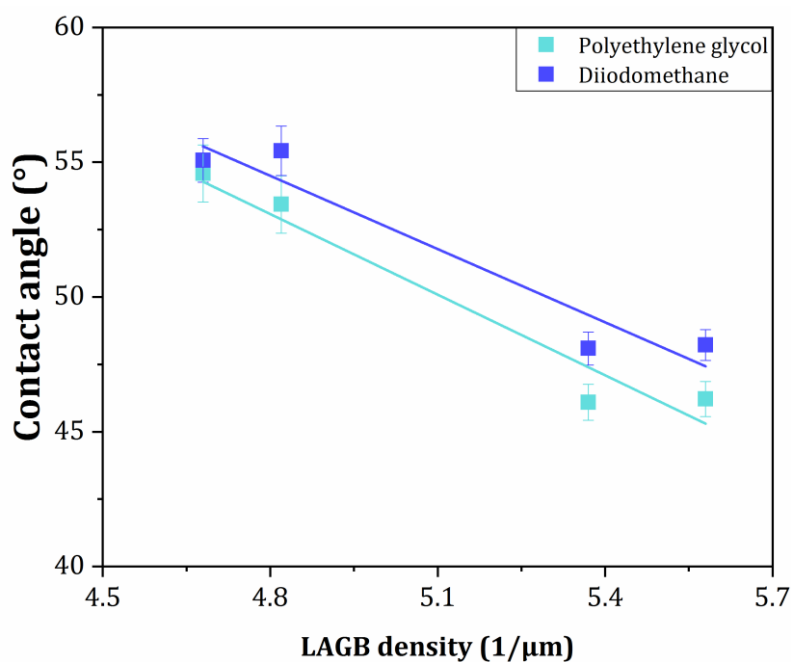
Figure 4.31. LAGB density – contact angle relationship for both the analyzed materials and both their CSs.

The differences in the contact angle of polyethylene glycol and diiodomethane evaluated between CSs taken from the same specimen were found to be statistically insignificant as well. Earlier reports implied wettability of a material to vary as a function of not only grain size but also crystal orientation [113], [114]. Herein, as the examined CSs are entirely dissimilar with

respect to grain size, HAGB density and the crystallographic orientation of grains, it could be expected that another parameter is mediating hydrophilicity of a material subjected to the HE process. In fact, while analyzing the corresponding CSs from specimens deformed at various strains, it may be observed that the differences in the contact angle of the two inspected solvents become statistically significant ($p < 0.05$). What is more, the wetting behavior of the materials deformed at the strain of 3.23 suggest that their surfaces experience higher hydrophilic (i.e., 35°-50°) character. Interestingly, a relationship between the measured contact angles and the LAGB density can be discovered, as seen in Fig. 4.31.

Although the correlation is not completely linear, it might be, without a doubt, stated that the higher density of LAGBs render more hydrophilic surfaces. What has to be additionally pointed out is that each of the LAGB density was calculated based on a single one IPF map and, therefore, to evaluate their arithmetic mean or standard deviation was out of reach. Still, the depicted relation may serve as an explanation for varied wettability of the HE-deformed titanium.
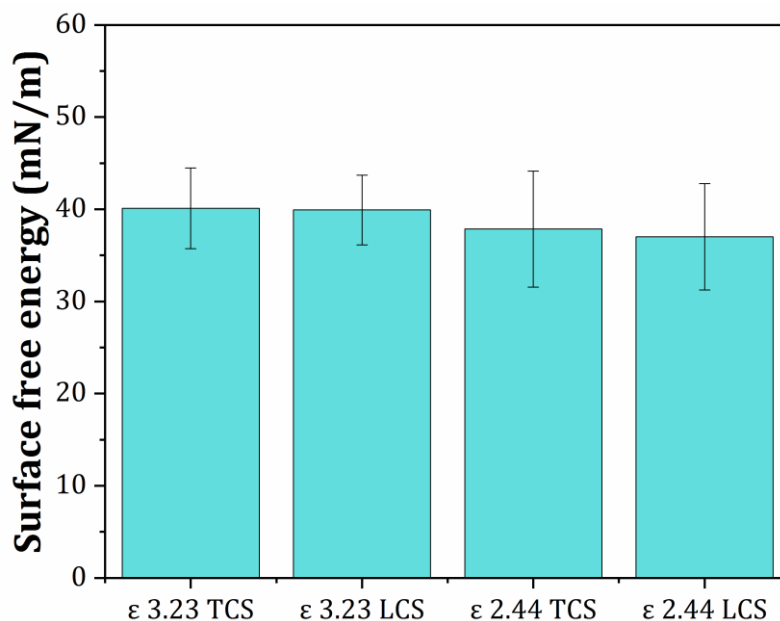
Figure 4.32. Surface free energies of the hydrostatically extruded titanium deformed at two different strains

On the contrary, the differences in the SFE measured for all of the studied materials were negligible, as seen in Fig. 4.32. Similar findings were reported for pure titanium processed at either six or ten stages of the HE process [73], though the calculated values of the SFE were substantially smaller when compared to these documented herein. The main reason behind the

observed discrepancies was the use of solvents for wettability measurements (formamide and hexadecane, instead of polyethylene glycol and diiodomethane) as well as different processing schedules. Finally, it could be envisaged that the effect SFE exerts on biophysical properties of a material was eliminated in a manner similar to surface roughness.

4.4.3. Chemical composition

Biological performance of a material may be improved or exacerbated, depending on the species, composition and density of functional groups present on its surface. For instance, acute inflammatory responses may be triggered by amine groups, yet attenuated by carboxyl ones. Hence, the inspection of surface chemistry is of immense significance if a material is to be utilized for medical purposes [115]. So far, chemical compositions of the SPD-processed materials have been infrequently addressed in the examinations of their biocompatibility [73], [86]. The truth is, any chemical modification within a surface would rather stem from developing of a new interphase e.g., by applying coating deposition, than plastic deformation.

The XPS-gathered chemical compositions of the passive layers formed on the materials chosen for physicochemical and biological investigations are depicted in Fig. 4.33, Fig. 4.34 and listed in Table 4.9. Only titanium and oxygen spectra/data were revealed, although calcium and carbon made up the elements detected on the studied surfaces as well. It is believed that their presence originated from surface contamination in the form of various Ca- or C-bearing compounds, including calcium oxide or calcium carbonate. The claim is supported by the fact that neither carbon nor calcium peaks were collected at high energy binding regions.

Irrespective of the examined substrate, the Ti 2p deconvoluted spectra were very similar in character and two major peaks were clearly visible. The first, present at 465 eV binding energy, originated from the Ti $2p_{1/2}$ state of stoichiometric TiO_2 (Ti^{4+}), and the second, detected at 458.1 eV, stemmed from the Ti $2p_{3/2}$ state of the same compound. Therefore, it has been demonstrated that Ti^{4+} was the dominant oxidation state of titanium in all of the characterized passive oxide films. Moreover, a clearly pronounced peak at the binding energy of 453.2 eV was also distinguished while analyzing the spectra taken from the TCSs of the investigated specimens. It corresponds to the Ti $2p_{3/2}$ state of the metallic titanium in the substrates and, along with a high $[Ti^{Me}]/[Ti^{4+}]$ ratio, confirms that the passive layer present on either of the TCSs was substantially thinner in comparison to that formed on the LCSs. The origin of such unusual behavior could be substantiated by the fact that the prismatic planes are more susceptible to etching [69]. In fact, herein, the ($10\bar{1}0$) planes dominated on the TCSs, whereas (0001) and ($11\bar{2}0$) planes were prevailing on the LCSs. In addition, the surfaces on the TCSs were characterized by greatly diversified surface composition since peaks indicating the existence of Ti(II) and Ti(III) oxidation states were more noticeable with comparison to these on the LCSs.
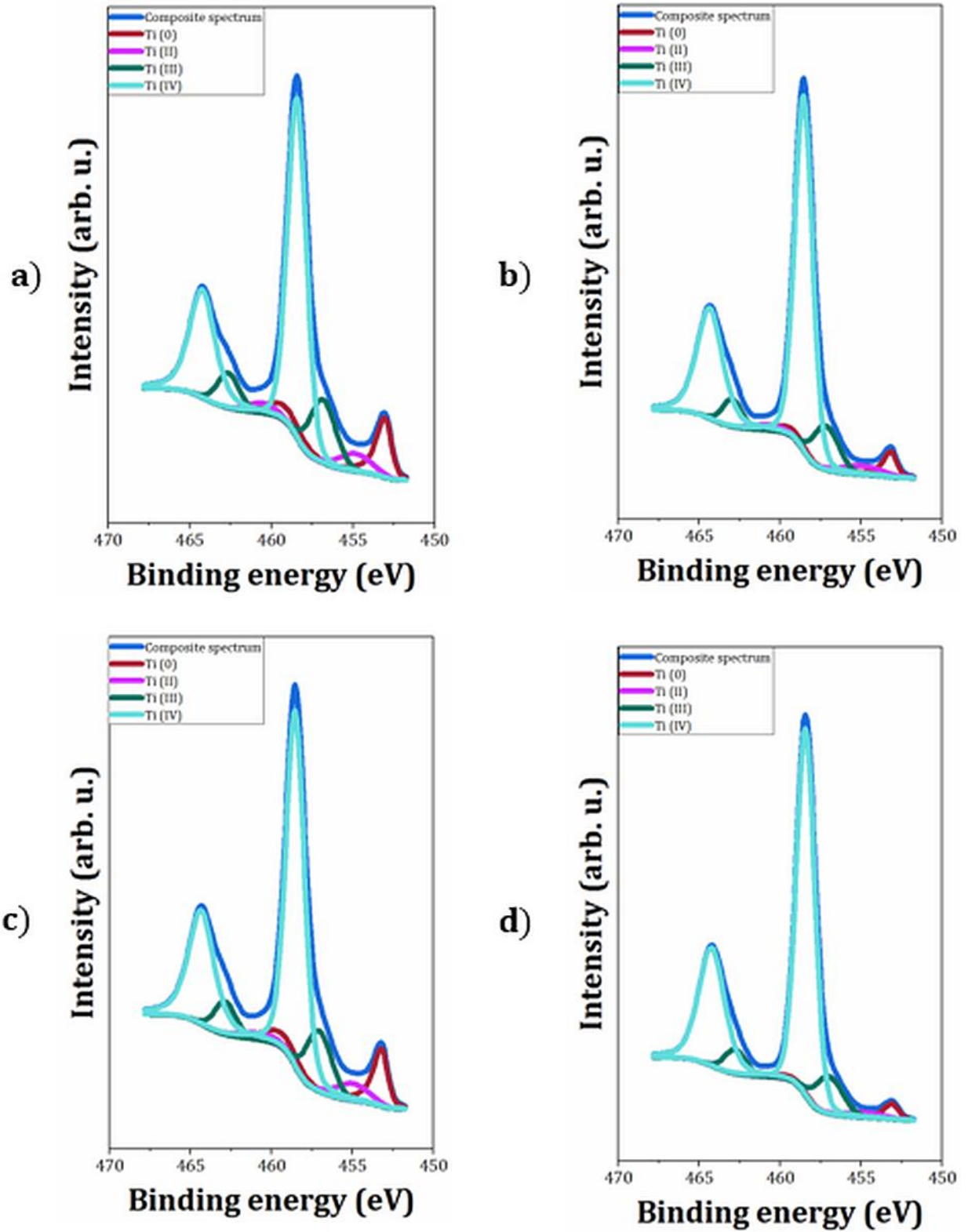
Fig. 4.33. Deconvoluted XPS spectra of Ti 2p obtained from the surfaces of the a) 3.23 TCS, b) 3.23 LCS, c) 2.44 TCS and d) 2.44 LCS
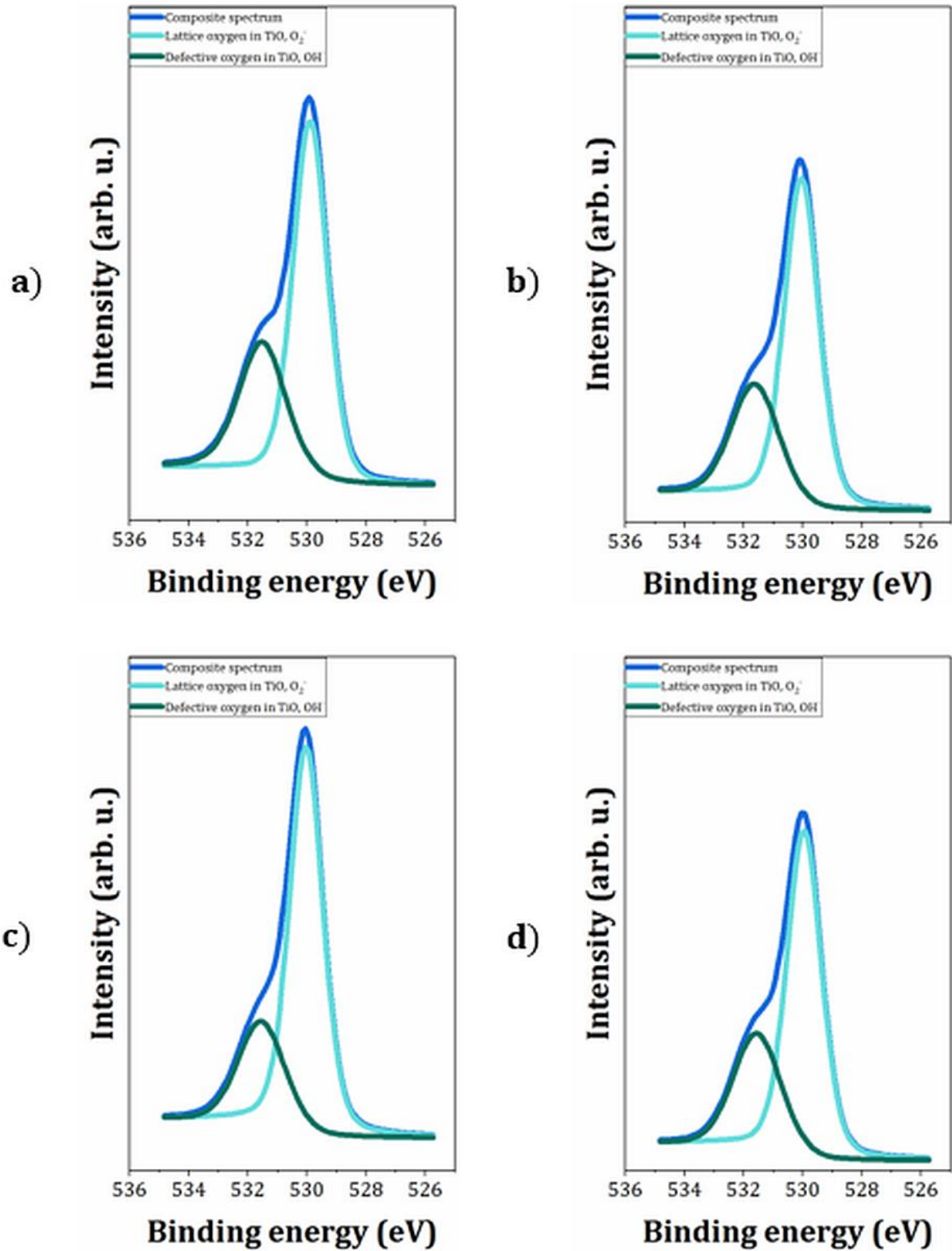
Fig. 4.34. Deconvoluted XPS spectra of O 1s obtained from the surfaces of the a) 3.23 TCS, b) 3.23 LCS, c) 2.44 TCS and d) 2.44 LCS

Table 4.94. Relative percentages of titanium and oxygen detected from the analyzed surfaces

	3.23 TCS	3.23 LCS	2.44 TCS	2.44 LCS
$[Ti^{Me}]$	0.11	0.05	0.10	0.03
$[Ti^{2+}]$	0.05	0.05	0.04	0.03
$[Ti^{3+}]$	0.17	0.13	0.16	0.12
$[Ti^{4+}]$	0.67	0.77	0.70	0.82
$[Ti^{Me}]/[Ti^{4+}]$	0.17	0.07	0.15	0.04
$[O_2^-]$	0.65	0.68	0.75	0.69
$[OH^-]$	0.35	0.32	0.25	0.31
$[OH^-]/[O_2^-]$	0.54	0.47	0.33	0.45

In the case of O 1s deconvoluted spectra, the differences between the examined materials were unveiled only by calculating the relative percentages of oxygen-containing species that could be assigned to the presence of O_2^- or OH^-. It has been recently discovered that the process of HE enables for a higher amount of hydroxyl groups to be absorbed onto the titanium surface [73], but the main reason behind such phenomenon is yet to be revealed.

All of the collected O 1s spectra exhibited a slight hump around the binding energy of 532.5 eV, which is assigned to the adsorbed oxygen. It confirms that the surface of the HE-processed titanium is covered with a great amount of hydroxyl groups. However, significantly higher percentage of the OH^- moieties was detected on the LCS of a sample deformed at the strain of 2.44, as compared to the TCS. Interestingly, analogous findings were reported while examining the surface of the ECAP-formed titanium [86]. Different concentration of functional (i.e., hydroxyl) groups on the surface was found to be related to the crystallographic orientation of grains. As a matter of fact, densely packed basal planes favor the presence of OH^- groups and, as a result, drive the production of Ti-OH bonds. Such a conclusion is fully consonant with the analysis presented herein as the LCS of a material deformed at the strain of 2.44 has mainly the (0001) planes exposed. On the contrary, with comparison to the TCS of a specimen deformed at the strain of 3.23, its LCS had slightly less percentage of the hydroxyl groups absorbed. However, it should be borne in mind that in the case of this particular CS, the grains were distributed between the (0001) and (11$\bar{2}$0) crystallographic planes. If biophysical properties of an SPD-processed sample are to be solely dictated by the chemical composition of its surface, then cell-material interactions should be enhanced on the LCSs of the HE-treated titanium.

4.5. Biophysical properties

4.5.1. Cytocompatibility

It is generally accepted that pure titanium demonstrates remarkable compatibility with living tissues and blood. As a matter of fact, biocompatibility has been one of its most well-known and researched features. However, it could be assumed that cytotoxicity of a biomaterial that has undergone plastic deformation may also be altered since a bunch of material's properties tend to change as soon as heavy strains are put into force. Surprisingly, it was found out that viability of osteoblast cells is greater on the surfaces of the ECAP-processed titanium than that reported for the reference materials i.e., Ti-6Al-4V alloy or unprocessed, coarse-grained titanium [70], [81]. In addition, similar findings were also reported for pure titanium processed at ten stages of the HE process and the phenomenon was ascribed to deformation-induced grain refinement [73]. Despite the fact that various assays (MTT, MST, WST-1) were undertaken to check up on the biocompatibility of the SPD-treated titanium, a general conclusion is that no cytotoxic effect against osteoblast cells was discovered.

Herein, HUVECs were used for cell viability assessment due to the fact this particular cell line has never been utilized in any cytotoxicity evaluation of the severely deformed titanium. Fig. 4.35 plots the obtained results of the performed MTT-based assay.
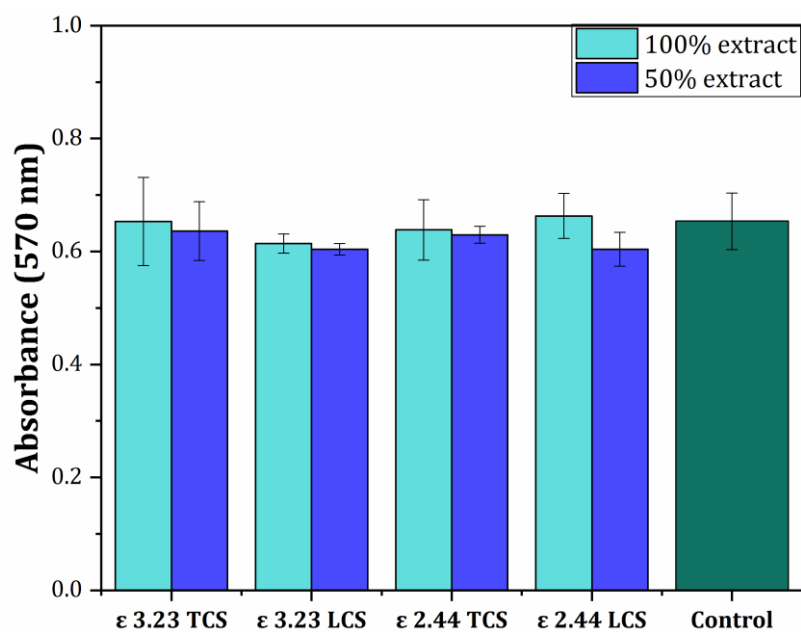
Figure 4.35. Assessment of cell viability of the analyzed surfaces by MTT assay

It may be observed that cell viability for all the analyzed materials reached the range of control (polystyrene). The differences in the recorded absorbance values between the tested specimens and the reference material were, as expected, statistically insignificant. In fact, it could be declared that the hydrostatically extruded titanium is characterized by excellent non-cytotoxicity i.e., surpassing the confidence level of 95%. Therefore, the material could be safely employed for medical applications in the future.

4.5.2. Protein adsorption

Owing to the fact that adsorption of water followed by that of proteins make up one of the very first events taking place as soon as an implant is embedded into a tissue, it is of utmost importance to identify how various proteins are attached on the surfaces of materials, especially the newly developed, intended for medical applications. In general, as implants do not directly come into contact with the biological matter, it is the protein-bearing layer that form the body-material interface, greatly affecting interactions between cells and surface [87]. The overall adsorption of proteins can be driven by electrostatic attraction, hydrophobic interactions or weak forces e.g., van der Waals'. In addition, the phenomenon is controlled by material's surface parameters (charge, hydroxylation, roughness, wettability), solution characteristics (composition, pH, temperature) as well as protein properties themselves (conformation, distribution, hydrophilicity, structure) [116]. Actually, protein adsorption represents a very complex and dynamic process, which is ruled by a multitude of various factors.

Within the present study, two entirely different proteins (serum-derived albumin and fibronectin) were used for the assessment of the protein-adhering properties the HE-processed titanium surface exhibits. The normalized absorption of albumin, a constitutional plasma protein, and fibronectin, a matrix-organizing protein, on the analyzed surfaces of the hydrostatically extruded titanium is displayed in Fig. 4.36.
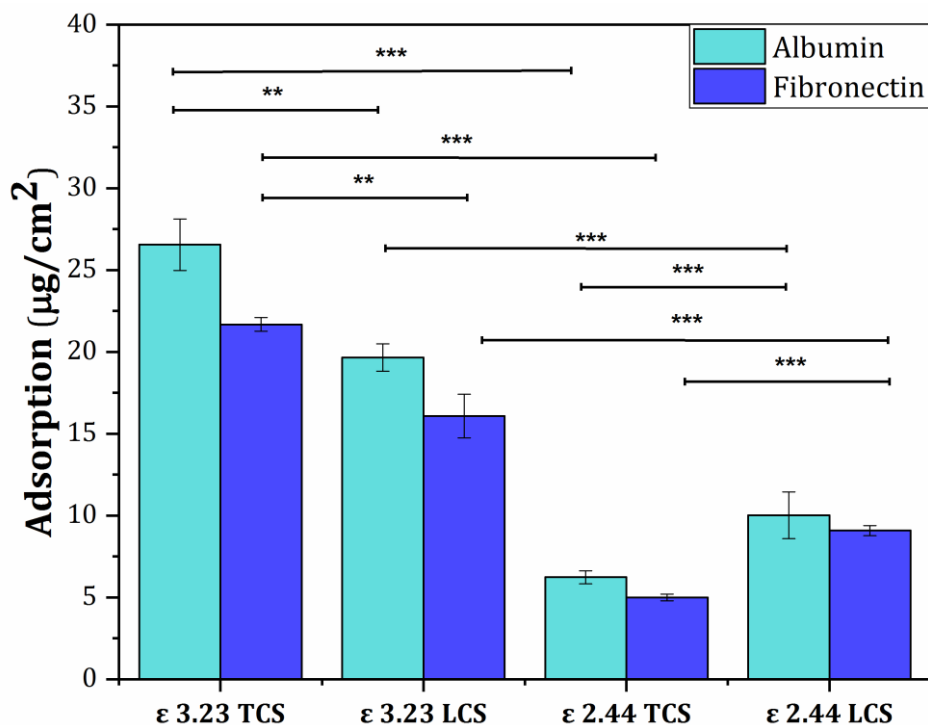
Figure 4.36. The adsorption of albumin and fibronectin onto the surfaces of the HE-processed titanium. The asterisk signs denote statistical significance (* $p < 0.05$, ** $p < 0.01$, *** $p < 0.001$) between the probes.

Regardless of the cross-section studied or the strain introduced, the adsorption of albumin to any surface of the HE-formed titanium was always greater than that of fibronectin. A precise explanation of such behavior would require delving into the proteomics, thus beyond the area of expertise the present study heads to. Nevertheless, as the selected proteins are completely dissimilar with respect to their size, colloidal nature, ion binding capacity or reactivity, the observed trend should be, without a doubt, attributed to the characteristics of the proteins utilized for investigations. In fact, one of the most important discrepancies between albumin and fibronectin are their dimensions and molecular weight. It is well-known that protein adsorption is a competitive phenomenon as proteins compete for a sufficient space on the surface. Smaller and more abundant proteins are able to get absorbed onto the surface more quickly than larger ones. Albumin, having dimensions of 4 nm × 4 nm × 14 nm and molar mass of 66 kDa, belongs to the former, whereas fibronectin, with dimensions of 18 nm × 9 nm × 9 nm and a molar mass of approximately ~550-600 kDa is an example of the latter [117]. Obviously, a conclusion may be drawn that reaching the equilibrium of adsorption by fibronectin takes up a greater amount of time.

Generally, the obtained results of protein assays clearly indicate that the adsorption behavior was specific for the hydrostatically extruded titanium. It may be noted that the TCS of a sample deformed at the strain of 3.23 was the one among the characterized surfaces that adsorbed the highest amount of albumin. On the flip side, the lowest concentration of the plasma-typical protein was found to adhere to the TCS of a specimen processed at the strain of 2.44. The same, rather unexpected regularities were noticed while analyzing the adsorption of fibronectin onto the examined substrates. What is also worth stressing out is that, irrespective of the type of protein and CS, the sample deformed at the strain of 3.23 was characterized by superior protein-adhering surface in comparison to that of the material deformed at the strain of 2.44. Overall, the differences in the normalized adsorption of both proteins between CSs taken from the same specimens as well as these between corresponding CSs coming from the materials fabricated at various strains were statistically significant ($p < 0.01$ or even $p < 0.001$).

Recently, it has been found out that the saturated concentration of albumin adsorbed on the surface of pure titanium increases had it been subjected to the process of HE. On the other hand, when compared to the unprocessed, coarse-grained material, the adsorption of fibronectin shows an opposite tendency if severely deformed surfaces are scrutinized. Eventually, microstructure refinement and its implications were claimed to have a considerable impact on protein adsorption [73]. However, if grain size was to be the major factor mediating the

adsorption of proteins on deformed surfaces, then, within the present study, the TCS of a sample processed at the strain of 2.44 would have attracted a substantially greater volume of proteins. Instead, the surface of this particular CS demonstrated the weakest protein-adhering ability. Since roughness and wettability ought to be ruled out from explications about the role of surface cues in protein adsorption, a special emphasis needs to be put on chemical composition, surface charge as well as surface irregularities.

It has been reported that the force enabling the surface of a material to attract charged proteins is bound with its electric properties, specifically relative permittivity, also known as dielectric constant. The lower it gets, the higher electrostatic force is generated, thus a greater chance for a protein molecule to be adhered to the surface [118]. Naturally, any differences in the composition of a passive layer could influence protein adsorption as relative permittivity is a characteristic material parameter. Herein, the TCSs of the hydrostatically extruded titanium contained markedly higher amount of Ti_2O_3 in comparison to the LCSs. Therefore, it might have been expected that both of the examined TCS would be able to adsorb substantially greater volume of either albumin or fibronectin. As seen, such a relation holds true only for a sample deformed at the strain of 3.23, thereby one may conclude that the discrepancies in chemical composition of passive films do not have a meaningful impact on protein adsorption.

Surprisingly, within the present study, the normalized concentrations of the adsorbed proteins were in harmony with the relative percentage of the hydroxyl groups detected on the analyzed surfaces:

- Proteins: 3.23 TCS > 3.23 LCS > 2.44 LCS > 2.44 TCS
- Hydroxyl groups: 3.23 TCS > 3.23 LCS > 2.44 LCS > 2.44 TCS

However, it has to borne in mind that the differences in the content of functional groups present on the surfaces were, in fact, marginal, with the exception of the TCS from a specimen deformed at the strain of 2.44. What is more, one may suppose that any influence of OH^- groups on albumin and fibronectin adsorption should be discarded since both of these proteins are negatively charged, therefore the repulsion forces would naturally come to the fore in contact with an already-hydroxylated surface. The truth is that under physiological conditions, any oxide-covered metal has an outmost layer composed of hydroxyl groups as a result of interactions between the surface and tissue-derived water molecules [87]. Therefore, it may be stated that the higher content of functional groups present on the surface do not considerably and directly affect protein adsorption. In fact, not only albumin, but also fibronectin tends to

get adsorbed easily on any surface due to their ability to alter conformation as well as high flexibility [119]. When conformation changes, the entropy, one of the major driving forces behind adsorption, is enhanced. As a consequence, amino acid side chains are instantly attracted by a charged adsorbent i.e., a surface [87]. If the strength of electric field within the zone formed between a protein layer and a metal is sufficient enough, then conformational states of biomacromolecules and their reactivity are controlled by surface charge [119]. Herein, all of the characterized surfaces were negatively charged, as the XPS data indicate, but the exact value of surface charge requires further investigations e.g., Zeta potential measurements. Interestingly, some reports on biocompatibility of metallic biomaterials clearly indicate that their biological behavior depends on the electronic structure of an inherent passive layer [71], [119]. Nevertheless, any changes in charge density, adsorption sites or electrostatic repulsion are pronounced if a material experienced deformation and is filled with substantial amount of microstructural/surface defects [87].

Herein, a surprising, linear relationship between LAGB density and proteins adsorption was discovered, as seen in Fig. 4.37, even though the differences in the density of non-equilibrium defects were subtle. As proven earlier, an SPD treatment leads to considerable changes in a material's microstructure as a variety of defects, including triple points, grain boundaries or dislocations, are generated. Interestingly, it has been documented that the abundance of defects affects corrosion resistance of a material, regarded as the most important parameter dictating its biocompatibility [44]. It could be, therefore, postulated that the presence of microstructural defects has an influence on electronic (semiconductor) properties a passive layer formed on a metallic material demonstrates. As a matter of fact, redox interactions between a film and proteins tend to increase if a material has been subjected to plastic deformation. Comparing to the unprocessed counterparts, both pure titanium as well as Ti-6Al-4V treated by ECAP manifested substantial differences in electronic conductivities, flat band potentials and surface charge [71]. The observed changes, especially the donor densities, were hypothesized to correlate with dislocation density. Although, within the present study the electronic properties of the passive layers were not tested, it may be stated that the high-density non-equilibrium microstructural defects, mainly LAGBs and dislocations, have a great influence on protein adsorption. Any defects within microstructure may be bound with surface irregularities and these, were claimed to profoundly influence how protein adhere to a surface [120]. The fact is that protein adsorption is known to be a non-specific phenomenon, occurring preferentially along the high energy regions e.g., grain boundaries, dislocations or second phase particles.

More importantly, the structural stability of a protein, the pH and the ionic strength of a protein-containing solution as well as the ability of a protein to modify its conformation have a major impact on the affinity of a particular protein to a surface. Any microstructural or surface defects might affect the abovementioned factors, yet the truth is that the exact mechanism responsible for adsorption of proteins onto metallic substrates is yet to be unveiled [116].
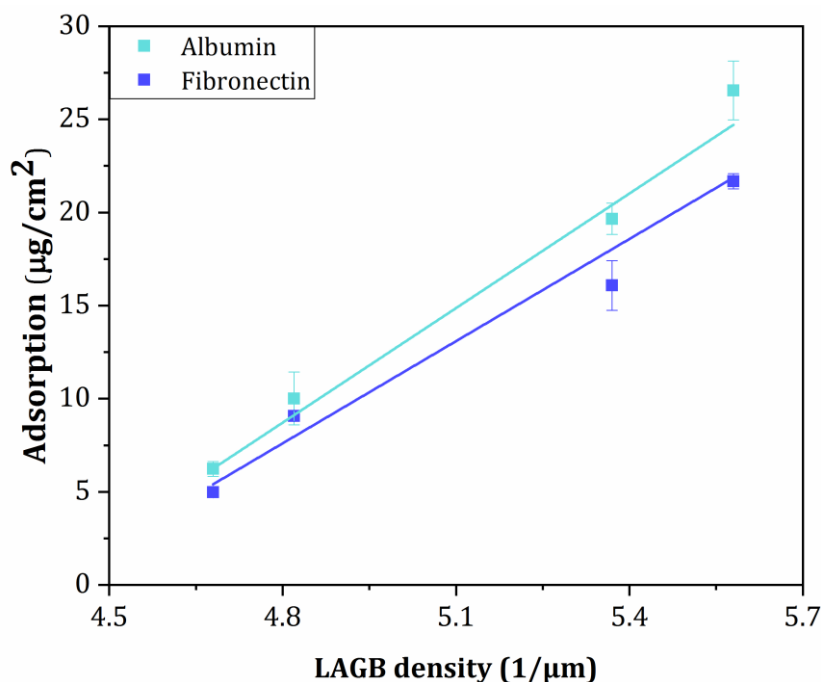
Figure 4.37. Normalized absorption of proteins vs. LAGB density

Finally, it is worth mentioning that protein adsorption is not, in most cases, a positive phenomenon. In general, it is one of the events of blood-material interactions that encompass also platelet adhesion and its activation as well as the processes of protein-promoted coagulation and thrombosis. Concerning osteointegration, once a protein-filled layer is secured at the interface between a living tissue and a synthetic material, a series of reactions aimed at platelet adhesion take place. The exact mechanism of protein adsorption at any surface consists of direct adhesion of biomolecules and rearrangement of those that have been adsorbed later on. Subsequently, inflammatory response mediated by neutrophils and monocytes occurs followed by differentiation of mesenchymal stem cells into osteoblasts. At the worst-case scenario, fibrotic encapsulation is triggered as a consequence of the proliferation of fibroblasts. The presence of fibrous tissue makes it impossible for a material to be safely fused with bony tissue, therefore the process of osteointegration is hindered. The biggest challenge is, thus, to

ensure that an equilibrium between protein adsorption and the activation of bone-forming mechanisms is guaranteed. Hence, no wonder that the contemporary materials science utilizes a plethora of various approaches, including surface biofunctionalization e.g., coatings with peptides or proteins, in order for a host to respond properly to an implanted material [116], [121], [122]. Protein adsorption, mostly a harmful phenomenon, might have positive implications as well. It has been demonstrated that once a denatured, absorbed protein transforms into a bio-film, it may reduce the wear rate of an artificial joint surface [123]. Furthermore, protein adsorption itself could also boost up the processes of cell attachment and subsequent proliferation [124].

4.5.3. Cell-material interactions

Two completely different cell lines were employed for cell-material interaction studies in order to gain a better insight into the mechanisms ruling the actual cell behavior on the surfaces of the severely deformed substrates. Since titanium and its alloys are nowadays mostly utilized for dental and orthopedic applications, the use of osteoblast cells seems natural. In addition, the interactions between the surface of the HE-processed titanium and endothelial cells were also investigated due to the fact that proliferation of these particular line has never been the subject of any reported examination concerning biocompatibility of the SPD-treated titanium-based materials. As some of the elements constituting e.g., a pacemaker are usually made out of pure titanium, the use of endothelial cells within the present study is also fully justified.

The CLSM-obtained morphologies of osteoblast and endothelial cells grown on the selected surfaces of the hydrostatically extruded titanium are depicted in Fig. 4.38 and Fig. 4.39, respectively. In addition, cell densities assessed out of at least five CLSM images are illustrated in Fig. 4.40. Cell culture was maintained for 72 hours so as the extent of proliferation is revealed and, thereby, the material's usefulness for biomedical applications is known. Evidently, both osteoblasts and endothelial cells responded differently to the analyzed surfaces of the HE-treated titanium. It confirms that the material manifests anisotropy of cell-material interactions, perceived as surface-dependent phenomena. At first glance, huge discrepancies in the size and the number of cells as well as their activity may be detailed. Regardless of the cell line analyzed and the strain imposed, it may be seen that cells displayed various behavior, depending on the CS examined. Without a doubt, cell viability was more enhanced on the TCSs of the HE-processed titanium. On the other hand, cells either barely survived or only a couple of them were distinguishable on both of the investigated LCSs what implies less pronounced cell activity.

In terms of the osteoblasts' viability, the TCS of a sample deformed at the strain of 2.44 was the only one among the studied substrates that have been entirely covered with a confluent monolayer. After 72 hours of incubation, the cells exhibited normal, phenotypic morphology, including polygonal configuration, oblong and flattened shape. In addition, wealth of cytoplasmic extensions had already been formed as cells were able to develop a stable linkage of spread fibers. The proliferation process was so intense that it became indiscernible to point out the exact, single cells. Osteoblasts were growing in all possible directions with no particular spreading pattern what indicates superior cell activity. The observations are fully supported by osteoblasts density, being a couple of times greater for the TCS of a material deformed at the

strain of 2.44 than for the rest of samples. In fact, one may suppose that instead of a single monolayer, a couple of cell layers were present on this surface. However, an akin phenomenon is characteristic of osteoconductive biomaterials, not the inert ones of whose titanium is the most prominent example [116]. The fact that osteoblasts were able to proliferate so vividly on titanium surface deserves a special attention as none of the reported studies with the use of severely deformed materials and osteoblasts have shown such outstanding interactions. One can risk stating that the transversal surface of the HE-processed titanium demonstrate bioactivity, yet the claim obligates further investigations, especially *in vivo* examinations or apatite-forming ability studies, to be performed. Surprisingly, the differences in the osteoblasts cell counts between all of the characterized surfaces were statistically significant. The lowest number of cells was evaluated for the LCS of a specimen deformed at the strain of 3.23. While examining osteoblast cells behavior on this particular substrate, the early signs of cell death, including globular morphology, the lack of filopodia and shrinkage, were seen. The exact mechanism of cell death, either apoptosis or necrosis, was, nonetheless, hard to determine out of the CLSM-collected images. Similar conclusions were not made when analyzing the cells activity on the LCS of a specimen processed at the strain of 2.44. Contrarily, the processes of extensive filopodia formation were clearly noticed as actin filaments began to assembly into a network of elongated, well-defined fibers. It is of vast significance for a further proper cell functioning to develop actin filaments as they play a major role in cellular locomotion, organelle movements and alterations in the shape of a cell [77]. The most striking difference between these two substrates is the mean grain size and the presence of $(11\bar{2}0)$ planes, thus it may be supposed that crystallographic texture has a strong influence on cell-material interactions.
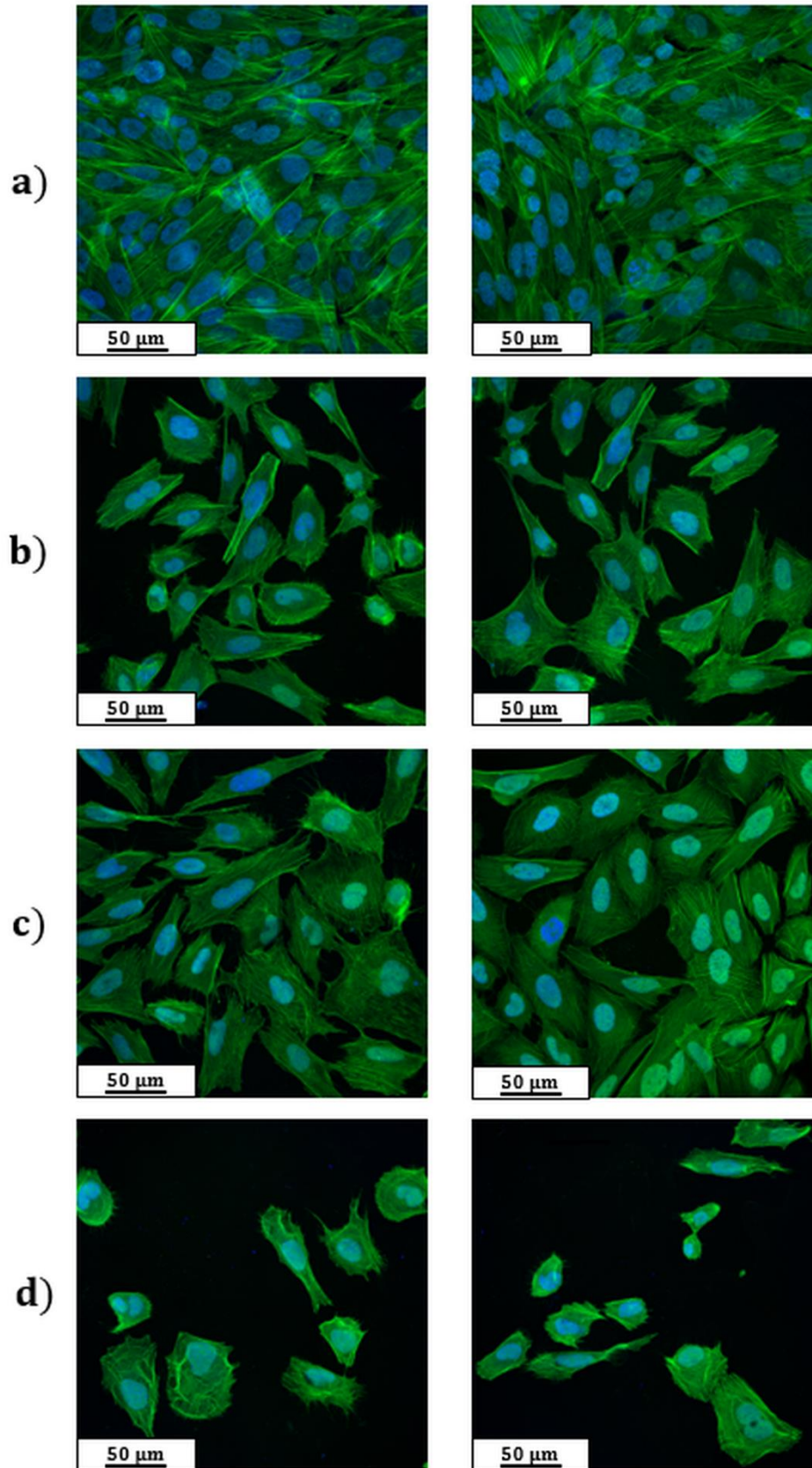
Figure 4.38. CLSM morphologies of osteoblast cells grown on HE-processed titanium deformed at the strain of a) 2.44 TCS, b) 2.44 LCS, c) 3.23 TCS, d) 3.23 LCS
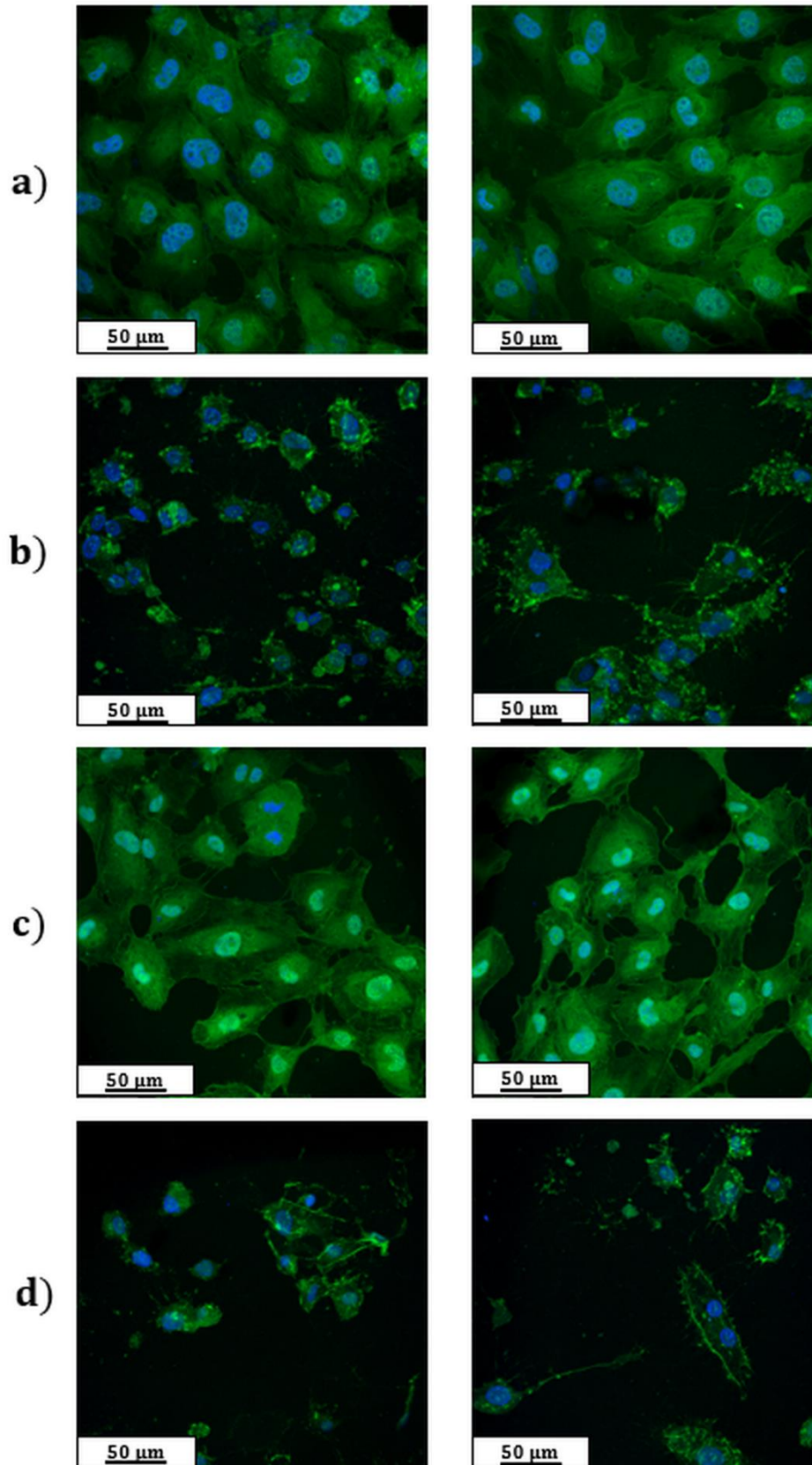
Figure 4.39. CLSM morphologies of endothelial cells grown on HE-processed titanium deformed at the strain of a) 2.44 TCS, b) 2.44 LCS, c) 3.23 TCS, d) 3.23 LCS

In terms of endothelial cells activity on the selected surfaces of the HE-processed titanium, a vast of similarities to that of osteoblasts may be noticed. However, in general, HUVECs experienced less dynamic proliferation than osteoblasts did. As seen, endothelial cells attached and spread on either of the examined TCSs more eagerly than on the LCSs. A nearly complete monolayer was formed only on the transversal surface of a material deformed at the strain of 2.44. The cells were large in size and displayed flattened, regular morphology what signifies good cell viability. Comparable characteristics were exhibited by HUVECs that cultivated on the surface of a specimen processed at the 3.23 of strain. Therein, the active processes of filopodia and lamellipodia formation as well as cytoskeleton organization, ultimately resulting in the development of a single monolayer, might have been witnessed. With respect to the LCSs, the main cellular mechanism taking place was cell death. In fact, abnormal morphology of HUVECs as well as their unnatural, small size clearly suggest low cell viability, even though a few cell clusters may have been distinguished. Interestingly, no statistically significant differences were found in endothelial cell densities between all of the studied substrates what is consonant with the MTT assay. Such unprecedented observation clearly proves that the use of cytotoxicity tests as well as the approaches making use of cell counts in the evaluation of material's biophysical properties is not sufficient. It has to be borne in mind that although a lot of cells were present on both of the analyzed LCSs, normal morphologies were revealed only for HUVECs that adhered to the TCSs.

In general, cell adhesion on any substrate is perceived as a multistage event, involving surface recognition by cells, generation of initial cell-surface contacts and their consecutive assembly into focal adhesions followed by cell migration on the substrate [114]. Although, within the present study, the actual cell adhesion phenomenon was not taken into examination as cells were cultured for 72 hours, one may easily deduce it from the extent of cell spreading. Titanium and its alloys belong to the group of chemically inert biomaterials, thus it is well-known that a stable, strong bonding between the metallic surface and living, organizing tissues do not form. In other words, cells poorly adhere to the surface of titanium-based materials. Cell adhesion and subsequent growth as well as proliferation are influenced mostly by proteins, especially the ECM proteins, membrane receptors (integrins) and cytoskeletal proteins [110]. Therefore, to reveal the exact mechanism responsible for cell behavior is only achievable by analysis of molecular events occurring directly at the examined surface. Nevertheless, an attempt, aiming at the explanation of cell-material interactions shown within the present study, has been made and presented thereinafter.
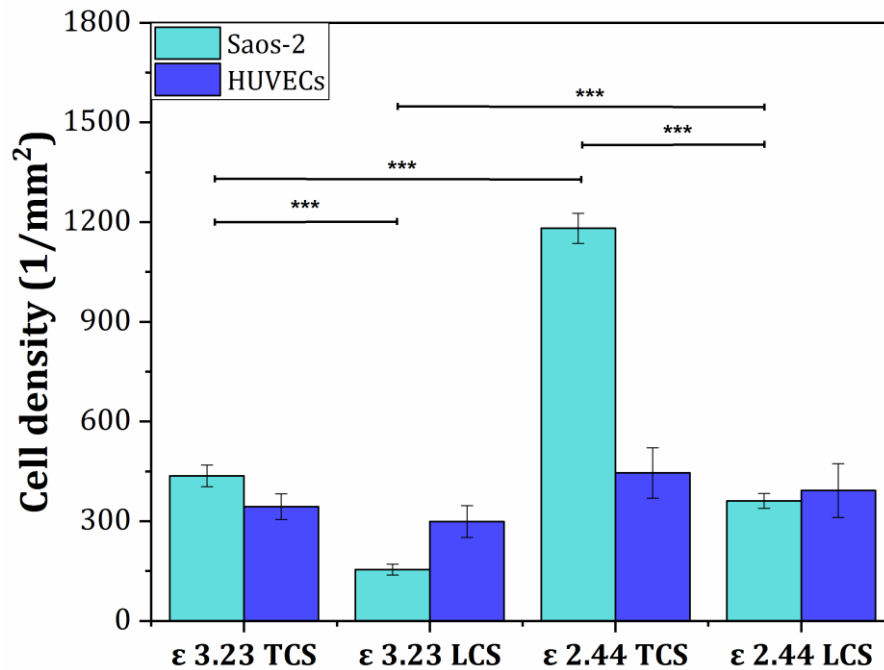
Figure 4.40. Cell densities assessed from CLSM-derived morphologies of cells grown on the HE-processed titanium surfaces. The asterisks sign *** denotes statistical significance (p < 0.001) between the probes.

A cellular response to any surface has origins in a cascade of events, incorporating protein adsorption and subsequent receptor-ligand binding followed by signal transduction. Proteins, both adsorbed and produced by a cell, determine, to the greatest extent, the strength and the extent of cell adhesion [125]. As a matter of fact, the overall cell behavior on a substrate is governed by physicochemical characteristics of the surface as well as properties of the macromolecules related to cytoskeleton and ECM, including actin, vinculin as well as fibronectin or albumin, depending on the cell type [77]. As soon as a single cell comes into contact with an artificial material, it secretes a variety of proteins, ready to change their conformation state easily. Fibronectin and albumin are considered the earliest biomolecules expressed by osteoblast and endothelial cells, respectively. They are, in fact, crucial proteins involved in the proper cell functioning, including its attachment, growth and motility [77], [126]. ECM proteins tend to influence cell signaling, organization of a nucleus as well as cytoskeleton formation by binding integrins. They are known to interact with specific receptors, what induces signal transduction and, consequently, regulates cell behavior [112]. Fixation, adherence, spreading and proliferation of cells are under the constant, direct control of proteins [127]. One of the most important factors affecting the adsorption of cell-derived proteins are roughness and hydrophilicity and the phenomenon is believed to be improved on any moderately-roughened, hydrophilic surface [69]. Within the present study, the impact of

101

wettability and roughness on biological behavior of the HE-processed titanium was excluded, thus there has to be an additional parameter responsible for the adsorption of proteins as well as subsequent cell adhesion and proliferation. The most probable scenario is that cells respond to various cues present on the surface. A distinct advantage of nanostructured and ultrafine-grained materials over their coarse-grained counterparts is that they exhibit a notably greater specific surface area, demonstrating itself in a massive number of nano-scaled features. Surface defects, functioning as adsorption and adhesion sites, promote the processes of protein adherence and cell attachment, respectively. Furthermore, defects-filled surfaces tend to regulate integrin functions so it identifies the proteins that have just been adsorbed onto surface [128]. Nano-sized features mimic the architecture of the ECM, regarded as an environment interacting with cells. In addition, not only integrin signaling but also signaling pathways, controlling the proper cell behavior, are influenced by surface defects [66]. Interestingly, the study related to *in vitro* biocompatibility of ECAP-processed titanium has proven that the number, the width and the depth of surface discontinuities positively affect cell response [129]. Nonetheless, the impact of surface irregularities is modulated, or even slightly obstructed, by conformation, distribution, quantity and type of the cell-borne proteins adsorbed on the surface [130]. As already mentioned, the protein-involving events occurring at the molecular level have the greatest impact on cell behavior. For instance, cell response could be greatly affected by the exposition of the tripeptide Arg-Gly-Asp, also known as the RGD motif [108]. Within the present study, in comparison to the LCSs, both of the examined TCSs were characterized by greatly defects-enriched surfaces as the AFM and the EBSD data indicated. At the same time, the most evident difference between the LCSs and the TCSs was crystallographic orientation of grains.

Irrespective of the cell line, the considerably higher cell densities on either of the TCSs taken from the hydrostatically extruded titanium proves that it is the presence of surface imperfections and the prismatic planes, not necessarily the small grain size, that modulates cell-surface relationship. One can conclude that the grain size does not have a meaningful impact on cell attachment and their subsequent migration and proliferation. Were it was for the grain size, osteoblasts and endothelial cells would have experienced much more intense activity on the LCS of a sample deformed at the strain of 3.23. Instead, barely a couple of properly grown cells were distinguished therein as some osteoblasts/HUVECs had supposedly undergone cell death. Similar outcomes were achieved while examining pre-osteoblasts response to the severely deformed surface since statistically insignificant differences were noted between the number of

cells grown on the coarse-grained and the ultrafine-grained HPT-treated titanium [69]. In addition to crystallographic texture, the role of microstructural or surface defects in cell performance should be praised as well. The high-density surface irregularities can affect conformation and distribution of adsorbed proteins by changing their binding sites/moieties [73]. However, herein, substantially higher density of defects was noted for the TCS of a material deformed at the strain of 3.23, yet it was the transversal surface of a specimen processed at the 2.44 of strain that was covered with a couple of cell layers, as osteoblasts density chart suggests. The fact that cell count was the greatest for this particular substrate could serve as a definite proof that neither the small grain size nor the presence of functional groups affects cell behavior. As demonstrated, the relative percentage of hydroxyl groups was the lowest on the TCS of a specimen processed at the strain of 2.44. It may be declared that having substantial amount of surface irregularities and the prismatic planes aligned parallel to the surface allows for a remarkable and, more importantly, proper cell behavior, involving attachment, migration, spreading and proliferation. A similar conclusion was drawn while investigating pre-osteoblast cells response to various titanium monocrystals [114]. Depending on a crystallographic plane directly exposed to the surface, severely deformed materials induce a change in conformational state of the adsorbed proteins leading to specific cell adhesion and proliferation. It has been shown that nanostructured titanium is able to adjust the conformation of adsorbed proteins by exposing protein epitopes, adhesive for osteoblast cells [108]. Within the present study, the impact of texture on biological behavior of SPD-treated titanium is reflected in dynamic, effective proliferation of cells on the prismatic planes. It is believed that proteins demonstrate different affinity for various crystal structures and, as a result, experience changes in conformation, leading finally to varied cell activity. The conformational alterations in the structure of ECM components, such as collagen, fibronectin and laminin, are of the greatest importance. These proteins have a tendency to modulate the processes of cell signaling, formation of cytoskeletal networks as well as organization of nuclei by binding adhesion receptors [88].

The modification of crystallographic orientation of grains should be regarded as one of the positive side effect the SPD processing brings about. Some of the earlier reports regarding biocompatibility of unconventionally-manufactured titanium pinpointed that the initial cell events i.e., attachment, growth and proliferation, are truly affected by crystallographic orientation of grains, whereas the late cell events i.e., differentiation and mineralization, are less dependent on texture [110], [112]. What needs to be additionally highlighted is that

subjecting a material to any SPD treatment might not necessarily leads to improvement of its biophysical properties. So far, the studies concerning biological behavior of nanostructured and UFG samples focused mainly on enhanced cell response as compared to the non-treated materials. The truth is, as proven herein, that, based on the crystal structure, cell-material interactions may be either increased or hindered. The key to improved cell behavior is mostly the presence of surface irregularities and the exposition of specific crystallographic planes. Moreover, by analyzing cells morphology after 72 hours of incubation, it can be stated that the HE-processed titanium should be dedicated to dental and orthopedic applications. HUVECs response to the surface of the hydrostatically extruded titanium was less impressive than that of osteoblasts.

It cannot be ruled out, however, that there are other various parameters mediating cell-substrate interactions as well. Within the present study, the differences in SFE between all of the examined substrates were marginal, statistically insignificant, but some of the previous reports, especially those exploiting computer-assisted modelling, have proven that the discrepancies in SFE between varied crystallographic planes of titanium actually exist. The prismatic planes display slightly higher SFE (1019 erg/cm^2), than the basal ones (988 erg/cm^2), due to the fact that they have the lower planar atomic density [69]. As a consequence of undergoing plastic deformation, the material is filled with a tremendous number of high-energy defects, specifically the non-equilibrium ones. These, along with long-range stresses, are responsible for considerably higher SFE of nanostructured or ultrafine-grained samples as compared to their unprocessed, coarse-grained counterparts [73]. It is well-known that increased, non-specific protein adsorption is linked to the enhanced SFE. Moreover, it has been reported that the prismatic planes are more susceptible to any etching-based treatment what is reflected in the generation of biologically active, more hydrophilic and roughened surfaces [69]. This is consistent with the results disclosed within the present study as the TCSs were covered with a thinner passive titania layer. Therefore, susceptibility of non-basal planes during etching and their SFE could also be linked to various biophysical properties of the severely deformed titanium. Finally, with respect to a thin passive layer, any possible modifications in its electronic properties, especially conductivity, might also affect biological behavior of the hydrostatically extruded titanium.

5.   Conclusions

Pure titanium obtained by the multistage process of hydrostatic extrusion followed by rotary swaging was extensively analyzed within the present study with a main focus centered on the origin of its mechanical and biophysical properties. The use of the state-of-the-art techniques, including electron backscatter diffraction, transmission electron microscopy and confocal laser scanning microscopy, enabled to state the following conclusions:

- Regardless of the strain applied, the microstructure of the hydrostatically extruded titanium is substantially refined and typical of severely deformed materials as reflected in a tremendous number of defects, including small-sized grains, grain boundaries, dislocations or triple points.
- The material is highly inhomogeneous in nature as proven by significant substructure, broad distribution of grain sizes, varying shapes of grains, considerable misorientation gradients within grains and the coexistence of coarse grains, fine grains, ultrafine grains as well as nanograins.
- The entire process of microstructure evolution is governed by the mechanism of grain subdivision, taking place at low strains, and that of continuous dynamic recrystallization, occurring at intermediate and high strains.
- Mechanical properties of titanium subjected to hydrostatic extrusion stem mainly from substructure strengthening and grain boundary strengthening, proving that strength of a severely deformed material is linked to the outcomes of grain refinement.
- The material processed at the strain of 3.23 outperforms the popular Ti-6Al-4V alloy in terms of its static mechanical properties.
- Pure titanium deformed by hydrostatic extrusion exhibits significant anisotropy of microstructure, texture and biological behavior.
- Hydrostatically extruded titanium is a fully biocompatible material; protein adsorption on its surface is mostly governed by the presence of surface defects, whereas cell-material interactions are regulated not only by surface irregularities but also diversified protein affinity to various crystallographic planes exposed directly to the investigated surface.
- The material might be considered for future applications in medicine and dentistry, especially as a dental implant material.

6.   Literature references

[1]   G. Lutjering and J. C. Williams, *Titanium*. Springer, 2003.

[2]   C. Leyens and M. Peters, *Titanium and titanium alloys. Fundamentals and Applications*. Wiley, 2003.

[3]   M. Aspects, "Titanium and Titanium Alloy Applications in Medicine," *Surf. Eng. Surg. Tools Med. Devices*, pp. 533–576, 2007.

[4]   A. M. Khorasani, M. Goldberg, E. H. Doeven, and G. Littlefair, "Titanium in biomedical applications—properties and fabrication: A review," *Journal of Biomaterials and Tissue Engineering*, vol. 5, no. 8. pp. 593–619, 2015.

[5]   R. P. Kolli and A. Devaraj, "A review of metastable beta titanium alloys," *Metals (Basel).*, vol. 8, no. 7, p. 506, 2018.

[6]   M. Kaur and K. Singh, "Review on titanium and titanium based alloys as biomaterials for orthopaedic applications," *Mater. Sci. Eng. C*, vol. 102, no. April, pp. 844–862, 2019.

[7]   L. C. Zhang and L. Y. Chen, "A Review on Biomedical Titanium Alloys: Recent Progress and Prospect," *Adv. Eng. Mater.*, vol. 21, no. 4, pp. 1–29, 2019.

[8]   S. Bahl, S. Suwas, and K. Chatterjee, "Comprehensive review on alloy design, processing, and performance of β Titanium alloys as biomedical materials," *Int. Mater. Rev.*, vol. 66, no. 2, pp. 114–139, 2021.

[9]   K. Kothari, "Manufacturing Techniques for Titanium Aluminide Based Alloys and Metal Matrix Composites," *Vasa*, p. 232, 2010.

[10]   D. K. Ammisetti and S. S. Harish Kruthiventi, "Recent trends on titanium metal matrix composites: A review," *Mater. Today Proc.*, 2020.

[11]   M. D. Hayat, H. Singh, Z. He, and P. Cao, "Titanium metal matrix composites: An overview," *Composites Part A: Applied Science and Manufacturing*, vol. 121. pp. 418–438, 2019.

[12]   H. Garbacz, I. P. Semenova, S. Zherebtsov, and M. Motyka, *Nanocrystalline titanium*. Elsevier, 2018.

[13]   M. Kulkarni, A. Mazare, P. Schmuki, and A. Iglič, "Biomaterial surface modification of

titanium and titanium alloys for medical applications," *Nanomedicine*, vol. 111, pp. 111–136, 2014.

[14]   S. H. Hong, Y. J. Hwang, S. W. Park, C. H. Park, J. T. Yeom, J. M. Park, and K. B. Kim, "Low-cost beta titanium cast alloys with good tensile properties developed with addition of commercial material," *J. Alloys Compd.*, vol. 793, pp. 271–276, 2019.

[15]   K. T. Kim, M. Y. Eo, T. T. H. Nguyen, and S. M. Kim, "General review of titanium toxicity," *Int. J. Implant Dent.*, vol. 5, no. 1, pp. 1–12, 2019.

[16]   M. do A. Ferreira, M. A. Luersen, and P. C. Borges, "Nickel-titanium alloys: A systematic review," *Dental Press J. Orthod.*, vol. 17, no. 3, pp. 71–82, 2012.

[17]   R. Sarvari, P. Keyhanvar, S. Agbolaghi, M. S. Gholami Farashah, A. Sadrhaghighi, M. Nouri, and L. Roshangar, "Shape-memory materials and their clinical applications," *International Journal of Polymeric Materials and Polymeric Biomaterials*. pp. 1–21, 2020.

[18]   L. C. Zhang, L. Y. Chen, and L. Wang, "Surface Modification of Titanium and Titanium Alloys: Technologies, Developments, and Future Interests," *Advanced Engineering Materials*. p. 1901258, 2020.

[19]   Muhammad Irfan, Badaruddin Soomro, Bilal Waseem, Sumaira Nosheen, and Abdul Karim Aziz, "Microstructural effects of the substrate on adhesion strength and mechanical properties of TiN Thin Films," *Int. J. Sci. Res. Arch.*, vol. 1, no. 2, pp. 022–031, 2020.

[20]   Y. Sasikumar, K. Indira, and N. Rajendran, "Surface Modification Methods for Titanium and Its Alloys and Their Corrosion Behavior in Biological Environment: A Review," *Journal of Bio- and Tribo-Corrosion*, vol. 5, no. 2. 2019.

[21]   E. Zhang, X. Zhao, J. Hu, R. Wang, S. Fu, and G. Qin, "Antibacterial metals and alloys for potential biomedical implants," *Bioactive Materials*, vol. 6, no. 8. pp. 2569–2612, 2021.

[22]   J. Buxadera-Palomero, K. Albó, F. J. Gil, C. Mas-Moruno, and D. Rodríguez, "Polyethylene glycol pulsed electrodeposition for the development of antifouling coatings on titanium," *Coatings*, vol. 10, no. 5, p. 456, 2020.

[23]   Y. Li, Y. Yang, R. Li, X. Tang, D. Guo, Y. Qing, and Y. Qin, "Enhanced antibacterial

properties of orthopedic implants by titanium nanotube surface modification: A review of current techniques," *International Journal of Nanomedicine*, vol. 14. pp. 7217–7236, 2019.

[24] T. C. Lowe, R. A. Reiss, P. E. Illescas, C. F. Davis, M. C. Connick, and J. A. Sena, "Effect of surface grain boundary density on preosteoblast proliferation on titanium," *Mater. Res. Lett.*, vol. 8, no. 6, pp. 239–246, 2020.

[25] F. Reshadi, G. Faraji, H. Moghtaderi, and S. Faghihi, "Surface and Bulk Modification of Titanium Grade 2 Substrates for Enhanced Biological Activity," *Jom*, vol. 72, no. 2, pp. 721–729, 2020.

[26] R. Z. Valiev, Y. Estrin, Z. Horita, T. G. Langdon, M. J. Zehetbauer, and Y. T. Zhu, "Fundamentals of Superior Properties in Bulk NanoSPD Materials," *Mater. Res. Lett.*, vol. 4, no. 1, pp. 1–21, Jan. 2016.

[27] K. Edalati, A. Bachmaier, V. A. Beloshenko, Y. Beygelzimer, V. D. Blank, W. J. Botta, K. Bryła, J. Čížek, S. Divinski, N. A. Enikeev, Y. Estrin, G. Faraji, R. B. Figueiredo, M. Fuji, T. Furuta, T. Grosdidier, J. Gubicza, A. Hohenwarter, Z. Horita, J. Huot, Y. Ikoma, M. Janeček, M. Kawasaki, P. Král, S. Kuramoto, T. G. Langdon, D. R. Leiva, V. I. Levitas, A. Mazilkin, M. Mito, H. Miyamoto, T. Nishizaki, R. Pippan, V. V. Popov, E. N. Popova, G. Purcek, O. Renk, Á. Révész, X. Sauvage, V. Sklenicka, W. Skrotzki, B. B. Straumal, S. Suwas, L. S. Toth, N. Tsuji, R. Z. Valiev, G. Wilde, M. J. Zehetbauer, and X. Zhu, "Nanomaterials by severe plastic deformation: review of historical developments and recent advances," *Mater. Res. Lett.*, vol. 10, no. 4, pp. 163–256, 2022.

[28] E. Bagherpour, N. Pardis, M. Reihanian, and R. Ebrahimi, "An overview on severe plastic deformation: research status, techniques classification, microstructure evolution, and applications," *International Journal of Advanced Manufacturing Technology*. 2019.

[29] S. Bagherifard, R. Ghelichi, A. Khademhosseini, and M. Guagliano, "Cell response to nanocrystallized metallic substrates obtained through severe plastic deformation," *ACS Appl. Mater. Interfaces*, vol. 6, no. 11, pp. 7963–7985, 2014.

[30] A. Sotniczuk and H. Garbacz, "Nanostructured Bulk Titanium with Enhanced Properties—Strategies and Prospects for Dental Applications," *Adv. Eng. Mater.*, vol. 23, no. 4, 2021.

[31] R. Z. Valiev, Y. Estrin, Z. Horita, T. G. Langdon, M. J. Zehetbauer, and Y. Zhu,

"Producing Bulk Ultrafine-Grained Materials by Severe Plastic Deformation: Ten Years Later," *JOM*, vol. 68, no. 4, pp. 1216–1226, Apr. 2016.

[32] D. Ahmadkhaniha, M. Fedel, M. Heydarzadeh Sohi, and F. Deflorian, "Corrosion behavior of severely plastic deformed magnesium based alloys: A review," *Surf. Eng. Appl. Electrochem.*, vol. 53, no. 5, pp. 439–448, 2017.

[33] R. Mahmoodian, N. S. M. Annuar, G. Faraji, N. D. Bahar, B. A. Razak, and M. Sparham, "Severe Plastic Deformation of Commercial Pure Titanium (CP-Ti) for Biomedical Applications: A Brief Review," *Jom*, vol. 71, no. 1. pp. 256–263, 2019.

[34] Z. S. Levin, X. Wang, M. Kaynak, I. Karaman, and K. T. Hartwig, "Strength and ductility of powder consolidated ultrafine-grain tantalum," *Int. J. Refract. Met. Hard Mater.*, vol. 80, no. May 2018, pp. 73–84, 2019.

[35] I. Ansarian, M. H. Shaeri, M. Ebrahimi, P. Minárik, and K. Bartha, "Microstructure evolution and mechanical behaviour of severely deformed pure titanium through multi directional forging," *J. Alloys Compd.*, vol. 776, pp. 83–95, 2019.

[36] K. Sztwiertnia, A. Morawiec, M. Bieda, and J. Kawałko, "Microstructure of titanium deformed by warm extrusion with forward- backward rotating die," in *IOP Conference Series: Materials Science and Engineering*, 2014, vol. 63, no. 1.

[37] A. Sotniczuk, D. Kuczyńska-Zemła, A. Królikowski, and H. Garbacz, "Enhancement of the corrosion resistance and mechanical properties of nanocrystalline titanium by low-temperature annealing," *Corros. Sci.*, vol. 147, no. November, pp. 342–349, 2019.

[38] J. J. Lewandowski, A. Awadallah, and C. Western, "Hydrostatic Extrusion of Metals and Alloys," *Metalwork. Bulk Form.*, vol. 14, pp. 440–447, 2018.

[39] H. Garbacz, M. Lewandowska, W. Pachla, and K. J. Kurzydłowski, "Structural and mechanical properties of nanocrystalline titanium and 316LVM steel processed by hydrostatic extrusion," *J. Microsc.*, vol. 223, no. 3, pp. 272–274, 2006.

[40] J. Kawałko, M. Wroński, M. Bieda, K. Sztwiertnia, K. Wierzbanowski, D. Wojtas, M. Łagoda, P. Ostachowski, W. Pachla, and M. Kulczyk, "Microstructure of titanium on complex deformation paths: Comparison of ECAP, KOBO and HE techniques," *Mater. Charact.*, vol. 141, pp. 19–31, 2018.

[41] D. Wojtas, K. Wierzbanowski, R. Chulist, W. Pachla, M. Bieda-Niemiec, A. Jarzębska,

Ł. Maj, J. Kawałko, M. Marciszko-Wiąckowska, M. Wroński, and K. Sztwiertnia, "Microstructure-strength relationship of ultrafine-grained titanium manufactured by unconventional severe plastic deformation process," *J. Alloys Compd.*, vol. 837, p. 155576, Oct. 2020.

[42] K. Majchrowicz, Z. Pakieła, W. Chrominski, and M. Kulczyk, "Enhanced strength and electrical conductivity of ultrafine-grained Al-Mg-Si alloy processed by hydrostatic extrusion," *Mater. Charact.*, vol. 135, no. May 2017, pp. 104–114, 2018.

[43] V. A. Milyutin and I. V. Gervasyeva, "Formation of crystallographic texture in Fe-Ga alloys during various types of plastic deformation and primary recrystallization," *Mater. Today Commun.*, vol. 27, no. February, 2021.

[44] A. Chojnacka, J. Kawalko, H. Koscielny, J. Guspiel, A. Drewienkiewicz, M. Bieda, W. Pachla, M. Kulczyk, K. Sztwiertnia, and E. Beltowska-Lehman, "Corrosion anisotropy of titanium deformed by the hydrostatic extrusion," *Appl. Surf. Sci.*, vol. 426, pp. 987–994, 2017.

[45] J. Lee, S. Y. Park, and H. Jeong, "Effect of strains on textural evolution of hydrostatically extruded niobium tubes," *Mater. Sci. Technol. (United Kingdom)*, vol. 36, no. 11, pp. 1245–1249, 2020.

[46] T. Majda, D. Moszczyńska, J. Zdunek, M. Kulczyk, J. Mizera, and K. J. Kurzydłowski, "Influence of hydrostatic extrusion process on the microstructure and texture of polycrystalline nickel," *Mater. Sci. Technol. (United Kingdom)*, vol. 33, no. 17, pp. 2046–2052, 2017.

[47] V. A. Milyutin, I. V. Gervasyeva, E. G. Volkova, A. V. Alexandrov, V. V. Cheverikin, Y. Mansouri, V. V. Palacheva, and I. S. Golovin, "Texture formation in FeGa alloy at cold hydrostatic extrusion and primary recrystallization," *J. Alloys Compd.*, vol. 816, p. 153283, 2020.

[48] T. H. Lee, M. S. Sim, S. H. Joo, K. T. Park, H. G. Jeong, and J. H. Lee, "Effect of intermetallic compound thickness on anisotropy of Al/Cu honeycomb rods fabricated by hydrostatic extrusion process," *Trans. Nonferrous Met. Soc. China (English Ed.*, vol. 26, no. 2, pp. 456–463, 2016.

[49] A. Y. Volkov, A. A. Kalonov, D. A. Komkova, and A. V. Glukhov, "Structure and Properties of Cu/Mg Composites Produced by Hydrostatic Extrusion," *Phys. Met.*

Metallogr., vol. 119, no. 10, pp. 946–955, 2018.

[50] P. Bazarnik, Y. Huang, M. Lewandowska, and T. G. Langdon, "Enhanced grain refinement and microhardness by hybrid processing using hydrostatic extrusion and high-pressure torsion," *Mater. Sci. Eng. A*, vol. 712, no. November 2017, pp. 513–520, 2018.

[51] B. Leszczynska-Madej, M. W. Richert, and M. Perek-NOWAK, "Effect of severe plastic deformation on microstructure evolution of pure aluminium," *Arch. Metall. Mater.*, vol. 60, no. 2, pp. 1437–1440, 2015.

[52] K. Topolski, H. Garbacz, W. Pachla, and K. J. Kurzydlowski, "The influence of the initial state on microstructure and mechanical properties of hydrostatically extruded titanium," *Solid State Phenom.*, vol. 140, pp. 191–196, 2008.

[53] E. C. Moreno-Valle, W. Pachla, M. Kulczyk, B. Savoini, M. A. Monge, C. Ballesteros, and I. Sabirov, "Anisotropy of uni-axial and bi-axial deformation behavior of pure Titanium after hydrostatic extrusion," *Mater. Sci. Eng. A*, vol. 588, pp. 7–13, 2013.

[54] K. Topolski, W. Pachla, and H. Garbacz, "Progress in hydrostatic extrusion of titanium," in *Journal of Materials Science*, 2013, pp. 4543–4548.

[55] M. Kulczyk, K. J. Kurzydlowski, W. Pachla, A. Mazur, and M. Sus-Ryszkowska, "Nanocrystalline titanium produced by hydrostatic extrusion," *J. Mater. Process. Technol.*, vol. 205, no. 1–3, pp. 173–182, 2007.

[56] G. Faraji, H. S. Kim, and H. T. Kashi, "Fundamentals of Severe Plastic Deformation," *Sev. Plast. Deform.*, pp. 19–36, 2018.

[57] Y. Cao, S. Ni, X. Liao, M. Song, and Y. Zhu, "Structural evolutions of metallic materials processed by severe plastic deformation," *Mater. Sci. Eng. R Reports*, vol. 133, no. May, pp. 1–59, 2018.

[58] J. Gubicza, "Defect structure in bulk nanomaterials processed by severe plastic deformation," *Defect Struct. Nanomater.*, pp. 41–83, 2012.

[59] G. Faraji, H. S. Kim, and H. T. Kashi, "Mechanical Properties of Ultrafine-Grained and Nanostructured Metals," in *Severe Plastic Deformation*, Elsevier, 2018, pp. 223–257.

[60] S. Liu, J. Liu, L. Wang, R. L. W. Ma, Y. Zhong, W. Lu, and L. C. Zhang, "Superelastic

behavior of in-situ eutectic-reaction manufactured high strength 3D porous NiTi-Nb scaffold," *Scr. Mater.*, vol. 181, pp. 121–126, 2020.

[61] Y. Estrin and A. Vinogradov, "Extreme grain refinement by severe plastic deformation: A wealth of challenging science," *Acta Mater.*, vol. 61, no. 3, pp. 782–817, 2013.

[62] Y. T. Zhu, J. Y. Huang, J. Gubicza, T. Ungár, Y. M. Wang, E. Ma, and R. Z. Valiev, "Nanostructures in Ti processed by severe plastic deformation," *J. Mater. Res.*, vol. 18, no. 8, pp. 1908–1917, 2003.

[63] D. F. Williams, "On the mechanisms of biocompatibility," *Biomaterials*, vol. 29, no. 20, pp. 2941–2953, 2008.

[64] X. Wang, B. Li, L. Zhou, J. Ma, X. Zhang, H. Li, C. Liang, S. Liu, and H. Wang, "Influence of surface structures on biocompatibility of TiO2/HA coatings prepared by MAO," *Mater. Chem. Phys.*, vol. 215, no. May, pp. 339–345, 2018.

[65] C. Y. Zheng, F. L. Nie, Y. F. Zheng, Y. Cheng, S. C. Wei, and R. Z. Valiev, "Enhanced in vitro biocompatibility of ultrafine-grained titanium with hierarchical porous surface," *Appl. Surf. Sci.*, vol. 257, no. 13, pp. 5634–5640, 2011.

[66] E. M. Lotz, R. Olivares-Navarrete, S. Berner, B. D. Boyan, and Z. Schwartz, "Osteogenic response of human MSCs and osteoblasts to hydrophilic and hydrophobic nanostructured titanium implant surfaces," *J. Biomed. Mater. Res. - Part A*, vol. 104, no. 12, pp. 3137–3148, 2016.

[67] H. Shahali, A. Jaggessar, and P. K. D. V. Yarlagadda, "Recent Advances in Manufacturing and Surface Modification of Titanium Orthopaedic Applications," *Procedia Eng.*, vol. 174, pp. 1067–1076, 2017.

[68] H. Chouirfa, H. Bouloussa, V. Migonney, and C. Falentin-Daudré, "Review of titanium surface modification techniques and coatings for antibacterial applications," *Acta Biomater.*, vol. 83, pp. 37–54, 2019.

[69] S. M. Baek, M. H. Shin, J. Moon, H. S. Jung, S. A. Lee, W. Hwang, J. T. Yeom, S. K. Hahn, and H. S. Kim, "Superior pre-osteoblast cell response of etched ultrafine-grained titanium with a controlled crystallographic orientation," *Sci. Rep.*, vol. 7, no. February, pp. 1–10, 2017.

[70] A. Sandeep Kranthi Kiran, M. Sireesha, R. Ramalingam, A. Kizhakeyil, N. K. Verma,

R. Lakshminarayanan, T. S. Sampath Kumar, M. Doble, and S. Ramakrishna, "Modulation of biological properties by grain refinement and surface modification on titanium surfaces for implant-related infections," *J. Mater. Sci.*, vol. 54, no. 20, pp. 1–18, 2019.

[71] M. Franz, B. Mingler, M. Krystian, L. Sajti, D. Pohl, B. Rellinghaus, C. Wolf-Brandstetter, and D. Scharnweber, "Strengthening of Titanium by Equal Channel Angular Pressing - Impact on Oxide Layer Properties of Pure Titanium and Ti6Al4V," *Adv. Mater. Interfaces*, vol. 7, p. 2000552, 2020.

[72] E. Matykina, R. Arrabal, R. Z. Valiev, J. M. Molina-Aldareguia, P. Belov, and I. Sabirov, "Electrochemical Anisotropy of Nanostructured Titanium for Biomedical Implants," *Electrochim. Acta*, vol. 176, pp. 1221–1232, 2015.

[73] D. Kubacka, A. Yamamoto, P. Wieciński, and H. Garbacz, "Biological behavior of titanium processed by severe plastic deformation," *Appl. Surf. Sci.*, vol. 472, pp. 54–63, 2019.

[74] Y. Estrin, C. Kasper, S. Diederichs, and R. Lapovok, "Accelerated growth of preosteoblastic cells on ultrafine grained titanium," *J. Biomed. Mater. Res. - Part A*, vol. 90, no. 4, pp. 1239–1242, 2009.

[75] M. Hoseini, P. Bocher, F. Azari, H. Vali, and J. A. Szpunar, "Effects of grain size and texture on the biocompatibility of commercially pure titanium," *Mater. Sci. Forum*, vol. 702–703, pp. 822–825, 2012.

[76] A. Günay-Bulutsuz, Ö. Berrak, H. A. Yeprem, E. D. Arisan, and M. E. Yurci, "Biological responses of ultrafine grained pure titanium and their sand blasted surfaces," *Mater. Sci. Eng. C*, vol. 91, no. June 2017, pp. 382–388, 2018.

[77] S. Faghihi, F. Azari, A. P. Zhilyaev, J. A. Szpunar, H. Vali, and M. Tabrizian, "Cellular and molecular interactions between MC3T3-E1 pre-osteoblasts and nanostructured titanium produced by high-pressure torsion," *Biomaterials*, vol. 28, no. 27, pp. 3887–3895, 2007.

[78] Y. Estrin, E. P. Ivanova, A. Michalska, V. K. Truong, R. Lapovok, and R. Boyd, "Accelerated stem cell attachment to ultrafine grained titanium," *Acta Biomater.*, vol. 7, no. 2, pp. 900–906, 2011.

[79] M. Novin and S. Faghihi, "Mouse bone marrow-derived mesenchymal stem cell response to nanostructured titanium substrates produced by high-pressure torsion," *Surf. Interface Anal.*, vol. 45, no. 2, pp. 619–627, 2013.

[80] M. A. Zile, S. Puckett, and T. J. Webster, "Nanostructured titanium promotes keratinocyte density," *J. Biomed. Mater. Res. - Part A*, vol. 97 A, no. 1, pp. 59–65, 2011.

[81] Y. G. Ko, D.-H. Lee, C. S. Lee, J.-H. Jang, C. H. Park, Y.-J. Kim, and J.-W. Park, "Enhanced osteoblast response to an equal channel angular pressing-processed pure titanium substrate with microrough surface topography," *Acta Biomater.*, vol. 5, no. 8, pp. 3272–3280, 2009.

[82] R. D. K. Misra, C. Nune, T. C. Pesacreta, M. C. Somani, and L. P. Karjalainen, "Understanding the impact of grain structure in austenitic stainless steel from a nanograined regime to a coarse-grained regime on osteoblast functions using a novel metal deformation-annealing sequence," *Acta Biomater.*, vol. 9, no. 4, pp. 6245–6258, 2013.

[83] B. E. Pippenger, M. Rottmar, B. S. Kopf, S. Stübinger, F. H. Dalla Torre, S. Berner, and K. Maniura-Weber, "Surface modification of ultrafine-grained titanium: Influence on mechanical properties, cytocompatibility, and osseointegration potential," *Clin. Oral Implants Res.*, vol. 30, no. 1, pp. 99–110, 2019.

[84] H. Mora-Sanchez, I. Sabirov, M. A. Monclus, E. Matykina, and J. M. Molina-Aldareguia, "Ultra-fine grained pure Titanium for biomedical applications," *Mater. Technol.*, vol. 31, no. 13, pp. 756–771, 2016.

[85] P. Jojibabu, B. R. Sunil, T. S. S. Kumar, U. Chakkingal, V. Nandakumar, and M. Doble, "Wettability and in vitro bioactivity studies on titanium rods processed by equal channel angular pressing," *Trans. Indian Inst. Met.*, vol. 66, no. 4, pp. 299–304, 2013.

[86] M. Hoseini, P. Bocher, A. Shahryari, F. Azari, J. A. Szpunar, and H. Vali, "On the importance of crystallographic texture in the biocompatibility of titanium based substrate," *J. Biomed. Mater. Res. - Part A*, vol. 102, no. 10, pp. 3631–3638, 2014.

[87] Z. Wang, Y. Yan, and L. Qiao, "Protein adsorption on implant metals with various deformed surfaces," *Colloids Surfaces B Biointerfaces*, vol. 156, pp. 62–70, 2017.

[88] D. Wojtas, A. Mzyk, J. Kawałko, G. Imbir, K. Trembecka-Wójciga, M. Marzec, A.

Jarzębska, L. Maj, K. Wierzbanowski, R. Chulist, W. Pachla, and K. Sztwiertnia, "Texture-Governed Cell Response to Severely Deformed Titanium," *ACS Biomater. Sci. Eng.*, vol. 7, no. 1, 2021.

[89]   G. S. Dyakonov, S. Mironov, I. P. Semenova, R. Z. Valiev, and S. L. Semiatin, "Microstructure evolution and strengthening mechanisms in commercial-purity titanium subjected to equal-channel angular pressing," *Mater. Sci. Eng. A*, vol. 701, no. June, pp. 289–301, 2017.

[90]   Y. J. Chen, Y. J. Li, J. C. Walmsley, S. Dumoulin, S. S. Gireesh, S. Armada, P. C. Skaret, and H. J. Roven, "Quantitative analysis of grain refinement in titanium during equal channel angular pressing," *Scr. Mater.*, vol. 64, no. 9, pp. 904–907, 2011.

[91]   Y. Sun, C. Zhang, H. Feng, S. Zhang, J. Han, W. Zhang, E. Zhao, and H. Wang, "Dynamic recrystallization mechanism and improved mechanical properties of a near α high temperature titanium alloy processed by severe plastic deformation," *Mater. Charact.*, vol. 163, no. March, p. 110281, 2020.

[92]   X. Ma, D. Zhao, S. Yadav, D. Sagapuram, and K. Y. Xie, "Grain-subdivision-dominated microstructure evolution in shear bands at high rates," *Mater. Res. Lett.*, vol. 8, no. 9, pp. 328–334, 2020.

[93]   G. S. D'yakonov, S. V. Zherebtsov, M. V. Klimova, and G. A. Salishchev, "Microstructure evolution of commercial-purity titanium during cryorolling," *Phys. Met. Metallogr.*, vol. 116, no. 2, pp. 182–188, 2015.

[94]   H. Fan, S. Aubry, A. Arsenlis, and J. A. El-Awady, "Grain size effects on dislocation and twinning mediated plasticity in magnesium," *Scr. Mater.*, vol. 112, pp. 50–53, 2016.

[95]   Y. J. Chen, Y. J. Li, J. C. Walmsley, S. Dumoulin, and H. J. Roven, "Deformation structures of pure titanium during shear deformation," in *Metallurgical and Materials Transactions A: Physical Metallurgy and Materials Science*, 2010, vol. 41, no. 4, pp. 787–794.

[96]   S. Bahl, B. T. Aleti, S. Suwas, and K. Chatterjee, "Establishing the microstructure-strengthening correlation in severely deformed surface of titanium," *Philos. Mag.*, vol. 98, no. 23, pp. 2095–2119, 2018.

[97]   B. Mingler, L. Zeipper, H. P. Karnthaler, and M. Zehetbauer, "TEM Investigations of Ti

Deformed by ECAP," *Nanomater. by Sev. Plast. Deform.*, pp. 369–374, 2005.

[98] G. S. Dyakonov, C. F. Gu, L. S. Toth, R. Z. Valiev, and I. P. Semenova, "Microstructure and mechanical properties of continuous equal channel angular pressed Titanium," *IOP Conf. Ser. Mater. Sci. Eng.*, vol. 63, no. 1, 2014.

[99] K. Kowalczyk-Gajewska, K. Sztwiertnia, J. Kawałko, K. Wierzbanowski, M. Wronski, K. Frydrych, S. Stupkiewicz, and H. Petryk, "Texture evolution in titanium on complex deformation paths: Experiment and modelling," *Mater. Sci. Eng. A*, vol. 637, pp. 251–263, 2015.

[100] K. Wierzbanowski, J. Jura, W. G. Haije, and R. B. Helmholdt, "F.C.C. Rolling Texture Transitions in Relation to Constraint Relaxation," *Cryst. Res. Technol.*, vol. 27, pp. 513–522, 1992.

[101] M. Wroński, "Modelling and experimental study of asymmetric rolling of titanium and aluminium," *PhD Thesis, AGH Univ. Sci. Technol.*, 2013.

[102] A. Meng, X. Chen, J. Nie, L. Gu, Q. Mao, and Y. Zhao, "Microstructure evolution and mechanical properties of commercial pure titanium subjected to rotary swaging," *J. Alloys Compd.*, vol. 859, p. 158222, 2021.

[103] V. F. Terentyev, S. V. Dobatkin, S. A. Nikulin, V. I. Kopylov, D. V. Prosvirnin, S. O. Rogachev, and I. O. Bannykh, "Fatigue strength of submicrocrystalline Ti and Zr-2.5%Nb alloy after equal channel angular pressing," *Kov. Mater.*, vol. 49, no. 1, pp. 65–73, 2011.

[104] R. Naseri, H. Hiradfar, M. Shariati, and M. Kadkhodayan, "A comparison of axial fatigue strength of coarse and ultrafine grain commercially pure titanium produced by ECAP," *Arch. Civ. Mech. Eng.*, vol. 18, no. 3, pp. 755–767, 2018.

[105] R. D. K. Misra, W. W. Thein-Han, T. C. Pesacreta, K. H. Hasenstein, M. C. Somani, and L. P. Karjalainen, "Cellular response of preosteoblasts to nanograined/ultrafine-grained structures," *Acta Biomater.*, vol. 5, no. 5, pp. 1455–1467, 2009.

[106] A. S. H. Makhlouf and M. Aliofkhazraei, *Handbook of Materials Failure Analysis with Case Studies from the Chemicals, Concrete and Power Industries*. Elsevier, 2015.

[107] M. Hourmand, M. S. Uddin, and A. A. D. Sarhan, "Processing of Titanium by Machining: A Closer Look Into Performance Metrics in Bio-Fabrications," in *Reference

Module in Materials Science and Materials Engineering, Elsevier, 2017, pp. 1–24.

[108] K. C. Nune and R. D. K. Misra, "Biological activity of nanostructured metallic materials for biomedical applications," *Mater. Technol.*, vol. 31, no. 13, pp. 772–781, 2016.

[109] S. Cai, C. Wu, W. Yang, W. Liang, H. Yu, and L. Liu, "Recent advance in surface modification for regulating cell adhesion and behaviors," *Nanotechnol. Rev.*, vol. 9, no. 1, pp. 971–989, 2020.

[110] A. T. Rad and S. Faghihi, "On the relation between surface texture of metallic implants and their bioactivity," *Surf. Innov.*, vol. 7, no. 2, pp. 93–100, 2018.

[111] A. T. Rad, M. Novin, M. Solati-Hashjin, H. Vali, and S. Faghihi, "The effect of crystallographic orientation of titanium substrate on the structure and bioperformance of hydroxyapatite coatings," *Colloids Surfaces B Biointerfaces*, vol. 103, no. 2016, pp. 200–208, 2013.

[112] S. Faghihi, F. Azari, H. Li, M. R. Bateni, J. A. Szpunar, H. Vali, and M. Tabrizian, "The significance of crystallographic texture of titanium alloy substrates on pre-osteoblast responses," *Biomaterials*, vol. 27, pp. 3532–3539, 2006.

[113] S. Faghihi, A. P. Zhilyaev, J. A. Szpunar, F. Azari, H. Vali, and M. Tabrizian, "Nanostructuring of a titanium material by high-pressure torsion improves pre-osteoblast attachment," *Adv. Mater.*, vol. 19, pp. 1069–1073, 2007.

[114] S. Faghihi, F. Azari, J. A. Szpunar, H. Vali, and M. Tabrizian, "Titanium crystal orientation as a tool for the improved and regulated cell attachment," *J. Biomed. Mater. Res. - Part A*, vol. 91, no. 3, pp. 656–662, 2009.

[115] P. Thevenot, W. Hu, and L. Tang, "Surface chemistry influences implant biocompatibility.," *Curr. Top. Med. Chem.*, vol. 8, no. 4, pp. 270–80, 2008.

[116] J. Barberi and S. Spriano, "Titanium and protein adsorption: An overview of mechanisms and effects of surface features," *Materials*, vol. 14, no. 7. 2021.

[117] H. Yang, B. Jia, Z. Zhang, X. Qu, G. Li, W. Lin, D. Zhu, K. Dai, and Y. Zheng, "Alloying design of biodegradable zinc as promising bone implants for load-bearing applications," *Nat. Commun.*, 2020.

[118] A. Michiardi, C. Aparicio, B. D. Ratner, J. A. Planell, and J. Gil, "The influence of

surface energy on competitive protein adsorption on oxidized NiTi surfaces," *Biomaterials*, vol. 28, no. 4, pp. 586–594, 2007.

[119] R. Thull, "Physicochemical principles of tissue material interactions," in *Biomolecular Engineering*, 2002, vol. 19, no. 2–6.

[120] Y. Wang, H. Deng, C. Huangfu, Z. Lu, X. Wang, X. Zeng, H. He, and H. Rao, "Research of protein adsorption on the different surface topography of the zinc oxide," *Surf. Interface Anal.*, vol. 47, no. 2, pp. 245–252, 2015.

[121] E. Jia, X. Zhao, Y. Lin, and Z. Su, "Protein adsorption on titanium substrates and its effects on platelet adhesion," *Appl. Surf. Sci.*, vol. 529, p. 146986, 2020.

[122] M. Talha, Y. Ma, P. Kumar, Y. Lin, and A. Singh, "Role of protein adsorption in the bio corrosion of metallic implants – A review," *Colloids and Surfaces B: Biointerfaces*, vol. 176. pp. 494–506, 2019.

[123] Y. Liao, R. Pourzal, M. A. Wimmer, J. J. Jacobs, A. Fischer, and L. D. Marks, "Graphitic tribological layers in metal-on-metal hip replacements," *Science (80-.).*, vol. 334, no. 6063, pp. 1687–1690, 2011.

[124] E. Anbazhagan, A. Rajendran, D. Natarajan, M. S. Kiran, and D. K. Pattanayak, "Divalent ion encapsulated nano titania on Ti metal as a bioactive surface with enhanced protein adsorption," *Colloids Surfaces B Biointerfaces*, vol. 143, pp. 213–223, 2016.

[125] S. Faghihi, M. R. Bateni, F. Azari, J. A. Szpunar, H. Vali, and M. Tabrizian, "The role of crystallographic texture of Ti-6Al-4V alloy on cell attachment and proliferation," *Mater. Sci. Forum*, vol. 495–497, no. PART 1, pp. 705–710, 2005.

[126] D. G. Tunica, X. Yin, A. Sidibe, C. Stegemann, M. Nissum, L. Zeng, M. Brunet, and M. Mayr, "Proteomic analysis of the secretome of human umbilical vein endothelial cells using a combination of free-flow electrophoresis and nanoflow LC-MS/MS," *Proteomics*, vol. 9, no. 21, pp. 4991–4996, 2009.

[127] T. N. Kim, A. Balakrishnan, B. C. Lee, W. S. Kim, B. Dvorankova, K. Smetana, J. K. Park, and B. B. Panigrahi, "In vitro fibroblast response to ultra fine grained titanium produced by a severe plastic deformation process," *J. Mater. Sci. Mater. Med.*, vol. 19, no. 2, pp. 553–557, 2008.

[128] N. Gui, W. Xu, D. E. Myers, R. Shukla, H. P. Tang, and M. Qian, "The effect of ordered

and partially ordered surface topography on bone cell responses: A review," *Biomater. Sci.*, vol. 6, no. 2, pp. 250–264, 2018.

[129] T. N. Kim, A. Balakrishnan, B. C. Lee, W. S. Kim, K. Smetana, J. K. Park, and B. B. Panigrahi, "In vitro biocompatibility of equal channel angular processed (ECAP) titanium," in *Biomedical Materials*, 2007, vol. 2, no. 3.

[130] S. Bahl, S. Suwas, and K. Chatterjee, "The importance of crystallographic texture in the use of titanium as an orthopedic biomaterial," *RSC Adv.*, vol. 4, no. 72, pp. 38078–38087, 2014.

Summary

Throughout the years, fine-grained, ultrafine-grained and nanostructured materials have drawn a considerable interest in a wide range of research fields since they are characterized by a set of superior characteristics in comparison to their untreated counterparts. A special attention has been focused on nanomaterials produced by the Severe Plastic Deformation (SPD) technologies and the chase after increased mechanical, magnetic or corrosion properties has become the prime aim of materials science-related studies. Hydrostatic Extrusion (HE), a well-established metalworking process and an unconventional SPD technique has proven itself effective in enhancing the strength of various metals and alloys, including titanium-, copper- or zinc-based materials. However, it is generally believed that some gaps in microstructure-property relationships have been overshadowed by the rapid development of novel materials. Whereas the origin of increased mechanical characteristics in plastically deformed samples is believed to be associated with grain refinement, their biological behavior has not been clearly elucidated.

The main purpose of the dissertation is to explicitly point out the sources responsible for the increased strength and biophysical properties in commercially pure titanium subjected to the multistage HE process. Despite the fact that the material has been proposed as an alternative to commonly applied alloys in medicine and dentistry, its properties have not been meticulously scrutinized and explained. In addition, an in-depth microstructural examination with the use of Transmission Electron Microscopy (TEM) and Electron Backscatter Diffraction (EBSD) was realized in order to trace the microstructure evolution of titanium during HE. A detailed analysis of grains, grain boundaries, misorientation gradients and crystallographic orientation of grains was executed. Mechanical behavior of the HE-processed titanium was assessed in a series of static tensile and compression tests as well as fatigue tests, while characterization of biophysical properties was carried out with the help of Atomic Force Microscopy (AFM) and X-ray Photoelectron Spectroscopy (XPS) techniques as well as wettability determination, cytotoxicity measurements, protein assays and Confocal Laser Scanning Microscopy (CLSM). All of the possible origins governing the mechanical and biophysical properties in the HE-manufactured titanium have been disclosed and interpreted.

An abundance of differently sized grains of various shapes and microstructural defects in the form of twins, dislocation-based structures, triple junctions and grain boundaries proves that pure titanium obtained by the multistep process of HE is a highly heterogeneous material with

regard to its microstructure. Moreover, the claim is supported by tremendous misorientation gradients in randomly chosen grains and the large deformation energy stored. At low strains, the main grain fragmentation mechanism dictating the microstructure downsizing is the grain subdivision process, as reflected in the constant presence of original/parent grains in deformed microstructures, the existence of grains demonstrating lengthened shape on transverse cross-sections of a material as well as the persisting lack of homogeneity in terms of grain size and shape. At intermediate and high strains, the process of continuous dynamic recrystallization comes to the fore as manifested by a progressively growing fraction of small-sized grains and high-angle grain boundaries with an increase in plastic strain exerted on a processed material. The finding is backed up by the fact that post-deformation heat treatment did not anneal out the dislocation-based defects present within the microstructure.

Hydrostatically extruded titanium outperforms the popular Ti-6Al-4V alloy in terms of yield strength and ultimate tensile strength. What is responsible for such an excellent tendency is the development of a significant substructure and the presence of high-angle grain boundaries, surrounding a vast amount of sub-microcrystalline grains. Due to hydrostatic extrusion, tensile strength of a material gets increased nearly two times when compared to the unprocessed, coarse-grained titanium. A relevant rise in hardness and its uniformity over a diameter of a sample should be mentioned as well. In addition, fatigue strength of the hydrostatically extruded titanium exceeds that of titanium fabricated by means of Equal Channel Agular Pressing, the most popular SPD technique.

With respect to biophysical properties of the HE-treated titanium, it could be stated that, regardless of the cell line or protein analyzed, it is the abundance of deformation-induced surface defects and the presence of prismatic planes exposed to the surface, not necessarily the small grain size, that mediates cell-material relationship. In addition, the role of surface roughness, wettability as well as chemical composition has shown to have a minor influence on biological behavior of a material. Due to the fact that osteoblasts grew and thrived more vividly on the surface of hydrostatically extruded titanium than endothelial cells, it might be concluded that the material may be an appropriate candidate for dental or orthopedic applications.

Streszczenie

Obserwowane na przestrzeni ostatnich lat zainteresowanie materiałami drobnoziarnistymi, ultradrobnoziarnistymi oraz nanostrukturalnymi, otrzymywanymi przy pomocy technik intensywnego odkształcenia plastycznego (ang. *Severe Plastic Deformation*, SPD), podyktowane jest koniecznością miniaturyzacji obiektów oraz udoskonalania ich właściwości. Biomateriały otrzymywane przy pomocy metod SPD charakteryzują się zwiększoną wytrzymałością mechaniczną oraz odpornością korozyjną, a zatem zestawem cech kluczowych z punktu widzenia potencjalnych zastosowań biomedycznych. Na wyjątkową uwagę zasługują biomateriały wytwarzane za pomocą wieloetapowego procesu wyciskania hydrostatycznego (ang. *Hydrostatic Extrusion*, HE), w tym ultradrobnoziarnisty tytan. Technika HE należy do niekonwencjonalnych metod SPD ze względu na redukcję wymiarów poprzecznych obrabianego elementu, jednak wytwarzany dzięki niej czysty technicznie tytan wyróżnia się unikalnymi właściwościami mechanicznymi oraz biofizycznymi. Powszechnie uważa się, że rozdrobnienie mikrostruktury determinuje wytrzymałość materiału, jednak kwestia genezy zmodyfikowanych, ulepszonych właściwości biofizycznych pozostaje niejasna.

Głównym celem rozprawy doktorskiej było jednoznaczne określenie czynników wpływających na poprawę właściwości mechanicznych oraz biofizycznych czystego tytanu poddanego procesowi wyciskania hydrostatycznego. Ponadto, dogłębne badania mikrostrukturalne materiału, zrealizowane z wykorzystaniem techniki dyfrakcji elektronów wstecznie rozproszonych oraz transmisyjnej mikroskopii elektronowej, przeprowadzono w celu zbadania ewolucji mikrostruktury materiału w trakcie wieloetapowego wyciskania hydrostatycznego. Szczególny nacisk położono na analizę ziaren, granic ziaren, gradientów dezorientacji wewnątrz ziaren, a także tekstury krystalograficznej. Właściwości mechaniczne hydrostatycznie wyciskanego tytanu określono w serii prób rozciągania, ściskania, a także w oparciu o badania właściwości zmęczeniowych. Charakterystykę właściwości biofizycznych dokonano przy zastosowaniu techniki mikroskopii sił atomowych, spektroskopii fotoelektronów w zakresie promieniowania X, mikroskopii konfokalnej, a także pomiarów zwilżalności i cytotoksyczności materiałów oraz zdolności ich powierzchni do adsorpcji białek.

Przeprowadzone badania mikrostrukturalne wykazały, że hydrostatycznie wyciskany tytan jest materiałem silnie niejednorodnym z punktu widzenia mikrostruktury. Fakt ten znajduje potwierdzenie w ogromnej ilości nagromadzonych defektów, wśród których wyróżnić należy granice ziaren, granice bliźniacze, dyslokacje czy punkty potrójne. Dodatkowo, o braku

jednorodności mikrostruktury materiału świadczy złożoność kształtów i wielkości ziaren, wielkość zmagazynowanej energii deformacji oraz gradienty dezorientacji wewnątrz ziaren. Otrzymany metodą HE tytan cechuje się ponadto silną teksturą krystalograficzną. Głównym mechanizmem odpowiedzialnym za rozdrobnienie mikrostruktury hydrostatycznie wyciskanego tytanu przy niskich odkształceniach jest podział ziarna, potwierdzony obecnością granic dużego kąta wewnątrz nieznacznie odkształconej frakcji gruboziarnistej oraz występowaniem ziaren o wydłużonym kształcie na przekrojach poprzecznych materiału. Przy średnich i dużych odkształceniach na pierwszy plan wysuwa się proces ciągłej dynamicznej rekrystalizacji, który znajduje odzwierciedlenie we wzrastającym udziale granic dużego kąta oraz ziaren o wielkości poniżej 2 μm. Obserwację tę potwierdza obecność defektów mikrostrukturalnych w materiale po zastosowaniu niskotemperaturowej obróbki cieplnej.

Wyciskany hydrostatycznie tytan przewyższa popularny stop biomedyczny Ti-6Al-4V pod względem umownej granicy plastyczności, a także maksymalnej wytrzymałości na rozciąganie. O właściwościach mechanicznych materiału w dużej mierze decyduje silna podstruktura oraz olbrzymi udział granic dużego kąta. Dzięki procesowi HE możliwy jest niemal dwukrotny wzrost wytrzymałości czystego tytanu w zestawieniu z materiałem gruboziarnistym, nieodkształconym oraz znacznie wzrasta twardość materiału, która, mierzona wzdłuż średnicy przekroju poprzecznego pręta, staje się bardziej jednorodna. Dodatkowo, wyciskany hydrostatycznie tytan przewyższa, z punktu widzenia wytrzymałości zmęczeniowej, właściwości tytanu otrzymywanego w jednym z najpopularniejszych procesów SPD tj. równokanałowym kątowym przeciskaniu (ang. Equal Channel Angular Pressing, ECAP).

Tytan otrzymywany metodą HE charaktryzuje się anizotropią właściwości biofizycznych. Niezależnie od analizowanej linii komórkowej czy roztworu białka, niewielki rozmiar ziarna, hydrofilowość, chropowatość powierzchni czy jej skład chemiczny nie mają decydującego wpływu na odpowiedź komórkową materiału. Obecność defektów powierzchniowych oraz płaszczyzn pryzmatycznych zdaje się mieć kluczowe znaczenie dla prawidłowego rozwoju komórek śródbłonka oraz osteoblastów na powierzchni materiału poddanego procesowi SPD. Hydrostatycznie wyciskany tytan może być więc odpowiednim kandydatem do zastosowań ortopedycznych i stomatologicznych ze względu na intensywność procesów komórkowych zachodzących na jego powierzchni z udziałem osteoblastów.

Appendix: HE predicted texture

The textures determined within the present thesis were also predicted with the use of the crystallographic deformation model for polycrystalline materials, introduced by Leffers and further developed by Wierzbanowski (the LW model) [100], [101].

In this model the elasto-plastic isotropic interactions between a single grain and its surroundings is assumed, according to the formula:

$$\sigma_{ij} = \Sigma_{ij} + L(E^p_{ij} - \varepsilon^p_{ij}) \qquad \text{(A1)}$$

where σ_{ij} and ε^p_{ij} denote the stress and the plastic strain tensors of a grain, respectively, whereas Σ_{ij} stands for the stress tensor applied to a sample, E^p_{ij} is the plastic strain tensor of a sample and L is a scalar interaction parameter. In the used deformation model, the crystal structure and appropriate crystal deformation mechanisms were considered. For calculations, the $\{0001\}<11\bar{2}0>$, $\{10\bar{1}0\}<11\bar{2}0>$ and the $\{10\bar{1}1\}<11\bar{2}0>$ slip systems as well as the $\{10\bar{1}2\}<\bar{1}011>$ and the $\{11\bar{2}2\}<\bar{1}\bar{1}23>$ twin systems were used.

A comparison between the EBSD-derived PFs and these obtained using the LW model is illustrated in Fig. A1.
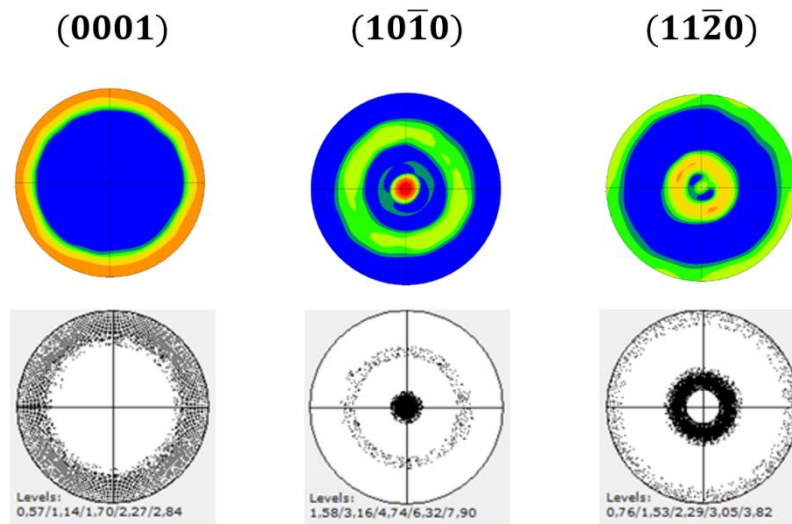
Fig. A1. EBSD-derived (top) and calculated with the use of the LW model (bottom) PFs, determined on TCS.

A remarkable match between the PFs is evident and it proves a correct selection of deformation mechanisms and the usefulness of the LW model in determination of texture during plastic deformation.